AIRFLOW RESISTIVITY MEASUREMENT OF ALKALINE EARTH SILICATE MATERIALS BETWEEN ROOM TEMPERATURE AND 800°C

Thesis submitted in accordance with the requirements of
University of Liverpool for the degree of Master of Philosophy

By

Thamasha Samarasinghe

School of Engineering, University of Liverpool

May 2019

ABSTRACT

The acoustic properties of porous materials are usually measured at room temperature. However in industrial applications, porous materials are sometimes required to provide sound absorption in high temperature environments such as in Heat Recovery Steam Generators (HRSG) applications, automobile silencers and aero engine liners. As the airflow resistance can be related to the sound absorption of porous materials, this is an important parameter to measure at the operating temperature. HRSG applications tend to operate at temperatures of 800 °C and above; however, the highest temperature in a previously reported study of airflow resistivity measurements on rock wool was 500 °C. Hence this research investigated the measurement of airflow resistance at room temperature according to ISO 9053-1 and in a bespoke test rig inside a kiln at temperatures from room temperature up to 800 °C. For the relevant high temperature applications, three different densities of Alkaline Earth Silicate (AES) fibrous materials were measured.

The design for the high temperature test rig required use of Matlab Simulink to carry out high temperature simulations before it was built. In addition, Simulink and analytical calculations were used to assess the effect of measuring the differential pressure after significant cooling of the air adjacent to the test sample. This showed that the differential pressure measured with the high temperature test rig after cooling of the air is significantly lower than at room temperature. The implication of this finding was that thick test samples were needed to ensure measurable differential pressure.

Measurements from the ISO 9053-1 and high temperature test rigs at room temperature confirmed that there was no significant difference between the two rigs. The high temperature tests indicated that there was no significant effect of temperature on specific airflow resistance for AES material between 20 and 100 °C but not at higher temperatures up to 800 °C. Above 600 °C, the effect of crystallisation and the change in material thickness meant that specific airflow resistance (rather than airflow resistivity) was used in regression analysis to identify empirical relationships for the three different density materials at different temperatures. In addition, it was found that the specific airflow resistance of these materials up to 600 °C was, on average, proportional to absolute temperature to the 1.6^{th} power.

To my Parents, in gratitude

ACKNOWLEDGEMENT

I would like to acknowledge my primary supervisor, Professor Carl Hopkins, for his guidance, support and advices during this project. Moreover, I would like to thank for the opportunity he gave me to enter and experience the world of acoustics.

Also, I would like to extend my gratitude to my secondary supervisor Dr. Gary Seiffert for his support, advices and his positive thoughts throughout my time in Acoustics Research Unit (ARU).

I am thankful to all my colleagues in the Acoustics Research Unit and my friends in both Liverpool and Sri Lanka for their kind support and the cooperation.

I would like to gratefully acknowledge, the funding and the facilitation provided by Morgan Advanced Materials Plc and especially, Miss Jilly Knox for her valuable support during in the project. Also, I would like to thank their industrial partner, Bibby's Precision Engineering Ltd for their support in fabricating the high temperature test rig.

Finally, I would like to thank my parents and my brother for their love, support and encouragement throughout my studies.

TABLE OF CONTENT

LIST OF TABLES viii

LIST OF FIGURES xi

CHAPTER 1. INTRODUCTION 1

1.1 Background and aim of the thesis 1

1.2 Aims 7

1.3 Outline of the thesis 8

CHAPTER 2. LITERATURE REVIEW 9

2.1 Measurement of airflow resistivity at room temperature 9

2.1.1 Room temperature experimental apparatus assembly....9

2.1.2 Empirical models for materials at room temperature....15

2.2 Measurements of airflow resistivity at high temperatures 18

2.2.1 Empirical relationships for airflow resistivity at high temperatures20

2.3 Summary 23

CHAPTER 3. EMPIRICAL THEORY 24

3.1 Empirical relationships between airflow resistivity and material properties 24

3.2 Empirical relationships between airflow resistivity and characteristic impedance 27

3.3 Empirical relationships for airflow resistivity, air viscosity and temperature 33

3.4 Summary 37

CHAPTER 4. DESIGN OF EXPERIMENTAL APPARATUS 38

4.1 Test samples 38

4.2 Measuring equipment for airflow 39

4.3 Air supply 40

4.4 Room temperature test rig 41

4.5 High temperature test rig 43

4.5.1 Initial design considerations....43

4.5.2 Kiln....45

4.5.3 Assessing a suitable length for the preheating chamber 47

4.5.4 Assessment of potential materials for the test rig 52

4.5.5 Thermal stress analysis of the high temperature test rig....55

4.5.6 Pipe connections....59
4.5.7 Simulink modelling to determine the length of pipe needed to ensure sufficient cooling....60

4.6 Choice of preheater material 70

4.7 Measurement of differential pressure 72
4.7.1 Simulink modelling of differential pressure measurements in the high temperature test rig....73
4.7.2 Manual calculation for differential pressure variation according to the temperatures....74

4.8 Summary 77

CHAPTER 5. RESULTS AND ANALYSIS 78

5.1 Room temperature measurements 78
5.1.1 Comparison of ISO 9053-1 and ASTM C522 results....78
5.1.2 Assessing the effect of air leaks in the pipes....80
5.1.3 Comparison of the ISO and high temperature test rigs....82
5.1.4 Regression analysis for different density materials....102
5.1.5 Effect of airflow velocity on the specific airflow resistance of double samples....110

5.2 High temperature measurements 114
5.2.1 Change in material thickness at high temperature....114
5.2.2 Differential pressure variation at high temperature....116
5.2.3 Specific airflow resistance and airflow resistivity of double samples at specific temperatures....119
5.2.4 Influence of temperature on the specific airflow resistance of double samples in high temperature test rig....121
5.2.5 Effect of airflow velocity on double samples....133
5.2.6 Regression analysis to relate specific airflow resistance to sample mass for different density materials....140
5.2.7 Regression analysis to identify the power law relationship between specific airflow resistance and temperature for different density materials....144

5.3 Summary 147

CHAPTER 6. CONCLUSIONS 150

6.1 Limitations of the research and recommendations for future work 152

REFERENCES 154

APPENDICES 162

LIST OF TABLES

Table 1. Linear airflow velocities and their corresponding SPL s at 20 ℃ and 800 ℃.....5
Table 2. Characteristic impedance calculation: Coefficients and exponents of the Mechel-Ver model [58].....32
Table 3. List of AES materials used for the measurements.....38
Table 4. Measured change in temperature along the length of pipe that was outside the kiln when the inside of the kiln was at 900 ℃.....65
Table 5. Temperature changes of pipework with cooler arrangement.....66
Table 6. Measured expansion for connectors of the test rig. 67
Table 7. Measured expansion of external connecting pipes. 67
Table 8. Measured expansion or shrinkage of test rig connectors.....67
Table 9. Measured pipe diameter change for external connecting tubes after heating to 900 ℃ and cooling down to room temperature (measurements carried out after the tube had cooled down to room temperature).....68
Table 10. Airflow resistivity results of material before heating the test rig without pipes and after heat up and cool down the test rig with connected pipes. 69
Table 11. Thermal conductivity of the packing material along with the temperature.....70
Table 12. Comparison between room temperature airflow resistivity measurements using ISO 9053-1 and ASTM C522 for different AES materials. 78
Table 13. Statistical test results on the comparison of ISO 9053-1(10 samples) and ASTM C522 (5 samples).....79
Table 14. Airflow resistivity results without leaks – sample of material ID No.0055 (64kg/m^3) 80
Table 15. Airflow resistivity results with a 2 mm diameter hole in the air supply – sample of material ID No.0055 (64 kg/m^3). Percentage error is based on the value in Table 14. 81
Table 16. Airflow resistivity results with a 2 mm diameter hole in the air supply and the differential pressure pipe – sample of material ID No.0055 (64 kg/m^3). Percentage error is based on the value in Table 14.....81
Table 17. Airflow resistivity results without leaks – 20 mm porous aluminium.....82
Table 18. Airflow resistivity results with a 2 mm diameter hole in the air supply - 20mm porous aluminium. Percentage error is based on the value in Table 17. 82
Table 19. Airflow resistivity results with a 2 mm diameter hole in the air supply and the differential pressure pipe – 20 mm porous aluminium. Percentage error is based on the value in Table 17. 82
Table 20. Airflow resistivity measured in the ISO test rig for single samples of AES material at room temperature. 84
Table 21. Airflow resistivity measured in the high temperature test rig for single samples of AES material at room temperature. 85
Table 22. Statistical output from an independent samples test for the ISO and high temperature test rigs: Single samples of material ID No.0048 (64 kg/m^3). 86
Table 23. Statistical output from an independent samples test for the ISO and high temperature test rigs: Single samples of material ID No.0064 (96 kg/m^3). 87
Table 24. Statistical output from an independent samples test for the ISO and high temperature test rigs: Single samples of material ID No.0058 (128 kg/m^3). 88

Table 25. Airflow resistivity results at room temperature for the ISO test rig. 89
Table 26. Airflow resistivity from the ISO test rig for double samples of AES material at room temperature. 90
Table 27. Airflow resistivity from the high temperature test rig for double samples of AES material at room temperature. 91
Table 28. Statistical output from an independent samples test for the ISO and high temperature test rigs: Material ID No.0048 (64 kg/m^3). 92
Table 29. Statistical output from an independent samples test for the ISO and high temperature test rigs: Material ID No.0064 (96 kg/m^3) 93
Table 30. Statistical output from an independent samples test for the ISO and high temperature test rigs: Material ID No.0058 (128 kg/m^3). 94
Table 31. Statistical output from an independent samples test for the thickness of single samples and the equivalent single sample thickness from double samples - ISO test rig. 95
Table 32. Statistical output from an independent samples test for the thickness of single samples and the equivalent single sample thickness from double samples - high temperature test rig.96
Table 33. Statistical output from an independent samples test for single and double samples in the ISO test rig: Material ID No.0048 (64 kg/m^3). 98
Table 34. Statistical output from an independent samples test for single and double samples in the ISO test rig: Material ID No.0064 (96 kg/m^3). 98
Table 35. Statistical output from an independent samples test for single and double samples in the ISO test rig: Material ID No.0058 (128 kg/m^3). 99
Table 36. Statistical output from an independent samples test for single and double samples in high temperature test rig: Material ID No.0048 (64 kg/m^3). 100
Table 37. Statistical output from an independent samples test for single and double samples in the high temperature test rig: Material ID No.0064 (96 kg/m^3). 101
Table 38. Statistical output from an independent samples test for single and double samples in the high temperature test rig: Material ID No.0058 (128 kg/m^3). 102
Table 39. Regression coefficients for single samples in the ISO and high temperature test rigs at room temperature. 103
Table 40. Relationship between airflow resistivity of single samples and bulk density at room temperature: ANOVA for regression variables in the order fitted 104
Table 41. Likelihood ratio test results.....106
Table 42. Regression coefficients for single and double samples in the ISO and high temperature test rigs at room temperature. 107
Table 43. Relationship between airflow resistivity of single and double samples and bulk density at room temperature: ANOVA for regression variables in the order fitted.....108
Table 44. Likelihood ratio test results.....109
Table 45. Likelihood ratio test results.....109
Table 46. Specific airflow resistance values for different airflow velocities at room temperature. 110
Table 47. Statistical test results on comparison of specific airflow resistance at room temperature for four different airflow velocities. 111
Table 48. Change in thickness of the double samples when heated in the kiln to 800 °C.....115
Table 49. Differential pressure variation of double samples in the high temperature test rig with packing. 116

Table 50. Corrected specific airflow resistance and airflow resistivity values for double samples in the high temperature test rig with packing inside the preheater. 119
Table 51. Statistical test output for specific airflow resistance of double samples at high temperatures for material ID No.0048 (64 kg/m^3).....123
Table 52. Statistical test output for specific airflow resistance at high temperatures for material ID No.0064 (96 kg/m^3) 127
Table 53. Statistical test output for specific airflow resistance at high temperatures for material ID No.0058 (128 kg/m^3) 130
Table 54. Specific airflow resistance values for different airflow velocities. 133
Table 55. Statistical comparison of specific airflow resistance at 800℃ for four different airflow velocities.....133
Table 56. Regression lines for each individual temperature.....140
Table 57. Relationship between airflow resistivity and mass of the double samples at temperatures between 20 and 800 ℃: Multiple regression analysis. 142
Table 58. Relationship between airflow resistivity and mass of the double samples at temperatures between 20 and 800 ℃: ANOVA for variables in the order fitted. 143
Table 59. Exponents for the absolute temperature from power law regression for individual samples.....144
Table 60. Statistical test output for exponents of power curves for each material ID. 146

LIST OF FIGURES

Figure 1. Cross section sketch of an HRSG indicating where the acoustic silencer can be incorporated. Image taken from reference [3]. 1
Figure 2. Dauchez et al's measuring apparatus. Image taken from reference [10]. 10
Figure 3. Resistometer use for variable airflow method according to ISO 9053 [2]. 10
Figure 4. Mendibil's test rig. Image taken from reference [11]. 11
Figure 5. Bies and Hansen's measuring apparatus. Image taken from reference [14]. 12
Figure 6. Apparatus used in Brown et al. Image taken from reference [16]. 13
Figure 7. Apparatus used by Dragonetti et al. Image taken from reference [17]. 14
Figure 8. Flow resistance apparatus. Image taken from reference [34]. 19
Figure 9. Apparatus used by Miglietta et al. Image taken from reference [36]. 20
Figure 10. The relationship between air viscosity and absolute temperature according to Sutherland's equation. 35
Figure 11. Experimental data for viscosity of nitrogen at different absolute temperatures. 36
Figure 12. Experimental data for viscosity of oxygen at different absolute temperatures. 36
Figure 13. Experimental data for viscosity of carbon dioxide at different absolute temperatures. 37
Figure 14. Flow rate and differential pressure measuring instrument. 39
Figure 15. Pressure regulator with the filter. 41
Figure 16. ISO test rig for room temperature experiments. 42
Figure 17. ISO test rig for room temperature measurements and associated measurement equipment. 43
Figure 18. 3D model of high temperature test rig. 45
Figure 19. The Kiln 46
Figure 20. Kiln dimensions. 46
Figure 21. Matlab Simulink: Model for the preheater length. 49
Figure 22. Matlab Simulink: Kiln temperature subsystem. 49
Figure 23. Matlab Simulink: Downstream temperature measurement subsystem. 50
Figure 24. Matlab Simulink: Upstream temperature measurement subsystem. 51
Figure 25. Matlab Simulink: Results for Port *A* (downstream temperature). 52
Figure 26. Matlab Simulink: Results for Port *B* (upstream temperature). 52
Figure 27. Temperature distribution of specimen holder cap 57
Figure 28. von-Mises stress distribution of specimen holder cap 57
Figure 29. Temperature distribution of specimen holder 58
Figure 30. von-Mises stress distribution of specimen holder 58
Figure 31. Temperature distribution of preheater 58
Figure 32. von-Mises stress distribution of preheater 58
Figure 33. AutoCAD 3D model of high temperature test rig with connecting pipes. 59
Figure 34. Photo of high temperature test rig with connecting pipes. 59
Figure 35. Matlab Simulink: System to assess pipe cooling. 60
Figure 36. Matlab Simulink: Results for the temperature of pipe. 63
Figure 37. Experimental set-up used to assess cooling of the connecting pipes. 64
Figure 38. Experimental cooler arrangement indicating temperature measurement points A and B. 66

Figure 39. Packing material inside preheater. 71
Figure 40. High temperature experimental assembly. 72
Figure 41. Simulation of the high temperature rig measurement using a local restriction to simulate a porous material. 74
Figure 42. Arrangement of high temperature test rig and the measuring instrument. 75
Figure 43. Relationship between airflow resistivity of single samples and bulk density at room temperature: Regression plots for the ISO test rig (blue) and the high temperature test rig (red). 103
Figure 44. Relationship between airflow resistivity of single and double samples and bulk density at room temperature: Regression plots for the ISO test rig (blue) and the high temperature test rig (red). 107
Figure 45. Specific airflow resistance at room temperature for four different airflow velocities. 113
Figure 46. Corrected differential pressure variation for double samples of AES material. 118
Figure 47. Specific airflow resistance at 800 ℃ for four different airflow velocities. 139
Figure 48. Relationship between specific airflow resistance and mass of the double samples at temperatures between 20 and 800 ℃. 141
Figure 49. Power law relationship for Material ID No.0048A 145
Figure 50. Power law relationship for Material ID No.0048B 145
Figure 51. Power law relationship for Material ID No.0064A 145
Figure 52. Power law relationship for Material ID No.0064B 145
Figure 53. Power law relationship for Material ID No.0064C 145
Figure 54. Power law relationship for Material ID No.0058A 145
Figure 55. Power law relationship for Material ID No.0058B 146
Figure 56. Exponents for individual material ID Nos. 147

Chapter 1. INTRODUCTION

1.1 Background and aim of the thesis

Sound absorbing materials are used to reduce reverberant sound pressure levels and the reverberation time in acoustic spaces. The sound absorption depends on material composition, thickness, surface finish and method of mounting which results in frequency-dependent absorption. In the building industry, porous materials are primarily used for room temperature applications. However, in other industries it is common for porous materials to be needed in high temperature applications to provide sound absorption such as in aero-engine liners, passive damping in combustion chamber, automotive silencers, and gas turbine exhaust silencers in Heat Recovery Steam Generators (HRSG) applications. Alkaline Earth Silicate (AES) porous material is used in order to reduce sound levels inside the silencers and near to the exhaust areas of HRSG which operate at temperatures between 800-1300℃ [1]. At present there is very limited understanding of how sound absorption at room temperature relates to the performance at temperatures up to 1000 ℃. The highest temperature in a previously reported study of airflow resistivity measurements on rock wool was 500 ℃. Hence, this research investigated the measurement of airflow resistance at room temperature according to ISO 9053-1 [2] and in a bespoke test rig inside a kiln at temperatures from room temperature up to 800℃. For the relevant high temperature applications, three different densities of Alkaline earth silicate fibrous materials were measured

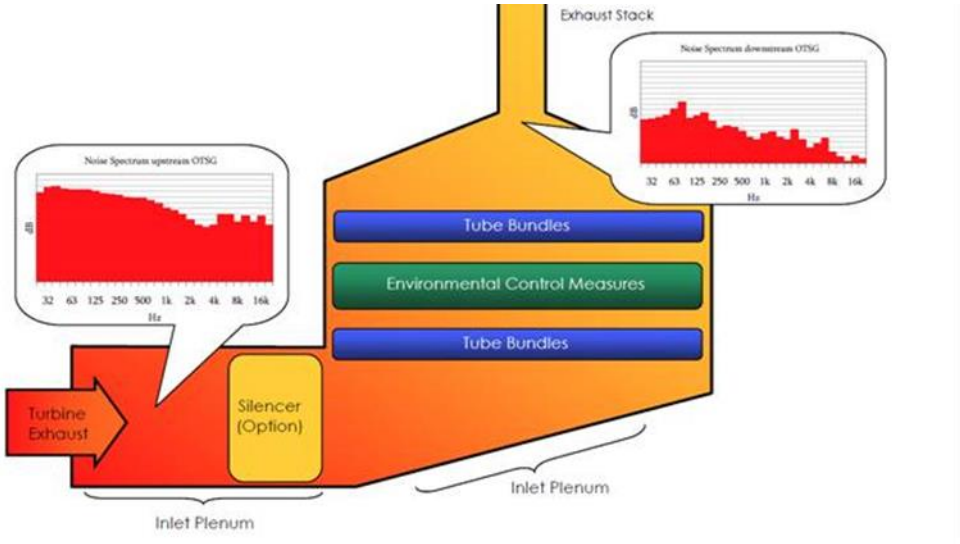

Figure 1. Cross section sketch of an HRSG indicating where the acoustic silencer can be incorporated. Image taken from reference [3].

The absorption coefficient is defined to describe the sound absorption of planar absorbers and takes values between 0 and 1. The intensity in a plane wave is proportional to the mean square pressure; hence the absorption coefficient, α, can be defined in terms of the reflection coefficient R as follows:

$$\alpha = 1 - |R|^2 \tag{1}$$

The reflection coefficient R can be expressed as follows.

$$R = \frac{Z_{a,s}cos\theta - 1}{Z_{a,s}cos\theta + 1} \tag{2}$$

where $Z_{a,s}$ denotes the specific acoustic impedance and θ is the incident angle of the sound.

Examples of porous materials which are sound absorbers include fiberglass, ceramics and plastic foam with open cells. When a porous material is exposed to incident sound waves, the air particles at the surface of the material and within the pores of the material vibrate and in doing so lose energy through conversion into heat due to thermal and viscous losses at the walls of the interior pores. Normally the process is isothermal at low frequencies and adiabatic at higher frequencies (e.g. see [4]).

The bulk acoustic properties of porous materials can be used to assess how sound propagates within it. Sound propagation in porous materials is dependent on the airflow resistivity (or the related parameters of airflow resistance and specific airflow resistance) hence it can be used to predict both sound absorption and sound attenuation (e.g. see [5]). The airflow resistivity of fibrous materials is due to friction between the fibres and the air particles moving between the fibres. Therefore, the airflow resistivity depends on the fibre diameter, shape/type of fibres, density of fibres, number of fibres per unit volume and the fibres tend to lie in planes which are parallel to the place of the sheet and the orientation of the fibres within each plane being random, the airflow resistivity in the lateral direction is significantly lower than in the longitudinal direction [6].

Airflow resistance can be used to determine the sound absorption by or sound propagation through porous material and the resistance to the airflow is quantified by airflow resistance, specific airflow resistance and airflow resistivity [2]. The airflow resistance, *R*, is defined as

$$R = \frac{\Delta P}{q_v} \tag{3}$$

where ΔP is the air pressure difference across a layer of porous material with respect to the atmosphere (Pa) and q_v is the volumetric airflow rate passing through the material (m^3/s).

The volumetric airflow rate, q_v, can be defined as follows [2]

$$q_v = uS \tag{4}$$

where u is the linear airflow velocity (m/s) and S is the cross-sectional area of the porous material (m^2).

According to ISO 9053-1 [2] which is the International measurement standard for airflow resistance for acoustical purposes, the recommended value of linear airflow velocity should be in the range from 0.5×10^{-3} to 15×10^{-3} m/s. In the American measurement standard, ASTM C522 [7], it is recommended that the linear velocities are in the range from 0.5×10^{-3} to 50×10^{-3} m/s. In order to understand the reason for these ranges of airflow velocity at room temperature it is useful to relate the values to the Sound Pressure Level (SPL), and then to calculate the corresponding SPL for these values at 800 ℃.

The sound pressure, p, and particle velocity, u, are related to the speed of sound, c_0, and the air density, ρ_0, by

$$\frac{P}{u} = \rho_0 c_0 \tag{5}$$

where the speed of sound is a temperature dependent parameter that can be calculated using [6]

$$c_0 = \sqrt{\frac{1}{K\rho}} = \sqrt{\frac{V}{KnM}} = \sqrt{\frac{\gamma PV}{nM}} = \sqrt{\frac{\gamma R(T+273.15)}{M}} \quad (6)$$

where ρ the gas density, K is the compressibility. V is the volume which is occupied by n moles of a gas, M is the molar mass of the gas in kg/mol (which is 28.97×10^{-3} kg/mol for air), γ is the ratio of specific heats at constant pressure and constant volume (which is 1.41 for air), P is static pressure which is 1.013×10^5 Pa for air at atmospheric pressure, R is the universal gas constant which has the value of 8.314 J/mol.K and T is temperature in ℃. Here, it is assumed that the conditions are adiabatic. For room temperature (20 ℃), the corresponding speed of sound is 344 m/s and for 800 ℃ the value is 659 m/s.

The density of air is also a temperature dependent parameter which can be calculated from

$$\rho_0 = \frac{353.2}{273+T} \quad (7)$$

The corresponding density of air for the room temperature (20 ℃) is 1.205 kg/m^3 and for 800 ℃ the value is 0.329 kg/m^3.

By assuming that the linear airflow velocity represents the particle velocity, the SPL in decibels,L_p can then be calculated from

$$L_P = 20\ \log_{10}\left({}^{p}/_{p_0}\right) \quad (8)$$

where p_0 is 20 μPa.

The SPL values for room temperature and 800 ℃ at different linear airflow velocities are given in Table 1. This indicates that the choice of 0.5×10^{-3} m/s is reasonable for most building acoustics design calculations in spaces where sound absorption is needed to reduce the SPL of

approximately 80 dB to levels that are suitable for occupation by people. It is also seen that the SPL at 800 ℃ is lower than at 20 ℃.

Table 1. Linear airflow velocities and their corresponding SPL s at 20 ℃ and 800 ℃

Linear airflow velocity (m/s)	Sound pressure level at 20 ℃ (dB)	Sound pressure level at 800 ℃ (dB)
0.5×10^{-3}	80.32	74.68
1×10^{-3}	86.34	80.70
2×10^{-3}	92.36	86.72
4×10^{-3}	93.38	92.74
8×10^{-3}	104.40	98.76
16×10^{-3}	110.42	104.78
32×10^{-3}	116.44	110.78
64×10^{-3}	122.46	116.82
128×10^{-3}	128.49	122.84

The specific airflow resistance, R_s, (Pa.s/m) applies to a specific thickness or a porous material. The specific airflow resistance is an appropriate specification parameter for both homogenous and non-homogenous materials as well as materials with a porous surface coating or perforated surface layer and materials where the thickness is not known exactly. The specific airflow resistance is defined as

$$R_s = R\,S \tag{9}$$

The airflow resistivity, *r*, (Pa.s/m^2) is only appropriate as a specification parameter for homogenous materials and is defined as

$$r = \frac{s\Delta P}{dq_v} = \frac{RS}{d} = \frac{R_s}{d} \tag{10}$$

where *d* is the thickness of the layer of porous material in the direction of airflow (m).

The airflow resistivity in the fibrous material depends on the direction of airflow through the material [2]. Usually, these materials are manufactured in rectangular sheets as slabs or in a roll; hence the airflow resistivity can be measured in two directions; in the plane of the sheet (lateral airflow) and perpendicular to the plane of the sheet (longitudinal airflow). Depending on the orientation of these sheets when installed to provide sound absorption, it is either the lateral or longitudinal direction that is needed to calculate the absorption coefficient [6].

Porous materials can be considered as a skeletal frame surrounded by gas [8]. Sound transmission through porous materials takes place due to airborne propagation through the pores and structure-borne propagation via the frame. Due to the varying degrees of coupling between these types of propagation, sound propagation through porous materials is more complex than in air. Two basic parameters that describe the properties of porous materials are the porosity and the airflow resistance. However, in order to describe them more completely, the structure factor, shape factor and tortuosity are often required [8].

For porous materials, the porosity,$\emptyset$, is calculated as follows

$$\emptyset = \frac{V_{\text{air}}}{V_{\text{bulk}}} \tag{11}$$

where V_{air} is the volume of air within the material and V_{bulk} is the bulk volume of the material.

Porous materials which are used in buildings typically have a porosity in the range between 0.9 and 0.99. If the material that binds solid fibres together has negligible mass, the porosity can be estimated as follows:

$$\emptyset = 1 - \frac{\rho_{\text{bulk}}}{\rho_{\text{fibre}}} \tag{12}$$

where ρ_{bulk} is the bulk density of the material and ρ_{fibre} is the fibre density [6].

Usually, the airflow resistance of the porous materials increases with increasing bulk density (e.g. see [6]). However, it is not certain that the porous materials with low or high airflow resistivity will always give the highest absorption coefficients over a wide frequency range.

The airflow resistance of fibrous materials is due to friction between the fibres and the air particles moving between the fibres; hence this makes a link to sound absorption [9]. Therefore, the airflow resistance depends on the size of fibres, shape/type of fibres, density of fibres, and number of fibres per unit volume. It also depends on the orientation of the fibres because the airflow resistivity in the lateral direction on sheet material is significantly lower than in the longitudinal direction in the plane of sheet material (the more common orientation for sheet material used to provide sound absorption) [6].

To estimate the sound absorption of a range of porous materials with different bulk densities it is possible to take a sufficiently large number of airflow resistivity measurements and determine an empirical relationship against a material property such as bulk density. For this purpose, this work describes the measurement of airflow resistivity (longitudinal direction) for Alkaline Earth Silicate (AES) fibrous materials at high temperatures.

1.2 Aims

To investigate the material properties that are relevant to sound absorption at high temperatures through the measurement of airflow resistance the main aims were:

- Design and build a test rig to measure airflow resistance according to ISO 9053-1 [2].
- Design and build a "high temperature test rig" to measure airflow resistance at temperatures up to 1000 ℃ (for practical reasons and for cost implications this was later limited to 800 °C in the project).
- Validate the high temperature test rig through comparison of the airflow resistance measured at room temperature with the ISO 9053-1 [2] test rig.
- Establish empirical relationships for the variation of airflow resistivity with temperature for AES materials using the high temperature test rig.

1.3 Outline of the thesis

Chapter 2 contains a literature review of previous work on airflow resistivity measurements including empirical models.

Chapter 3 describes the theory related to the airflow resistivity, characteristic impedance, the sound absorption and the air viscosity.

Chapter 4 describes the design of the experimental apparatus to measure airflow resistivity at room temperature and high temperature.

Chapter 5 presents and analyses the results of the room temperature and high temperature airflow resistivity measurements.

Chapter 6 contains the conclusions.

Chapter 2. LITERATURE REVIEW

2.1 Measurement of airflow resistivity at room temperature

Many of the applications for porous materials as sound absorbers is inside buildings; hence the material properties are usually measured at room temperature. For this reason, this section reviews the literature on room temperature measurement of airflow resistivity.

2.1.1 Room temperature experimental apparatus assembly

The literature indicates that room temperature airflow resistivity measurements are carried out using either constant or variable flow which was described by ISO 9053-1 [2] or ASTM C522 [7].

Dauchez et al [10] used the constant airflow method to measure airflow resistivity. To generate constant airflow they used a vacuum pump with a water column. Two types of porous materials were considered, one material with a known airflow resistivity R_1, which was used as a reference material and the other material whose airflow resistivity R_2 is to be measured. These two materials (cross-sectional area A and thickness t) were placed in series and manometers were used to measure the differential pressures ΔP_1 and ΔP_2 across the two samples as shown in Figure 2. Therefore, the airflow resistivity can be determined using

$$r = R_2 \frac{A}{t} \tag{13}$$

Since, the airflow is constant, the following relationship must be fulfilled,

$$\frac{\Delta P_1}{R_1} = \frac{\Delta P_2}{R_2} \tag{14}$$

Therefore, by considering equations 13 and 14 the airflow resistivity can be determined as follows:

$$r = R_1 \frac{\Delta P_2}{\Delta P_1} \frac{A}{t} \tag{15}$$

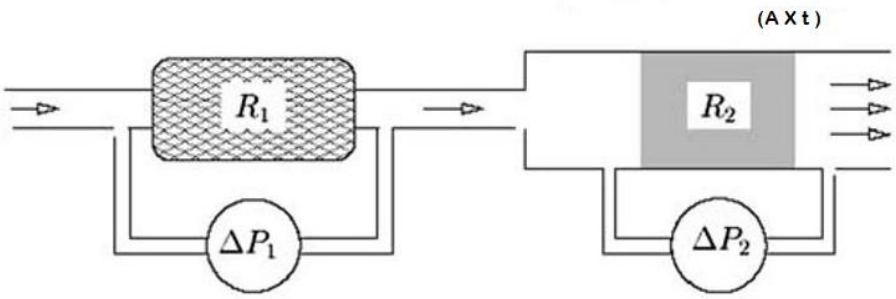

Figure 2. Dauchez et al's measuring apparatus. Image taken from reference [10].

Mendibil [11] used a variable airflow method to measure airflow resistivity which required oscillating air pressure from a moving piston. Due to the movement of the piston, the air pressure inside the measuring cell increases and decreases at the same frequency as the piston. A condenser microphone was used to measure the air pressure and the microphone was calibrated at 2 Hz using a pistonphone in order to fulfill the ISO 9053-1 [2] requirements of alternating airflow method. The piston movement is sinusoidal and can be achieved using a lever or a mechanical system.

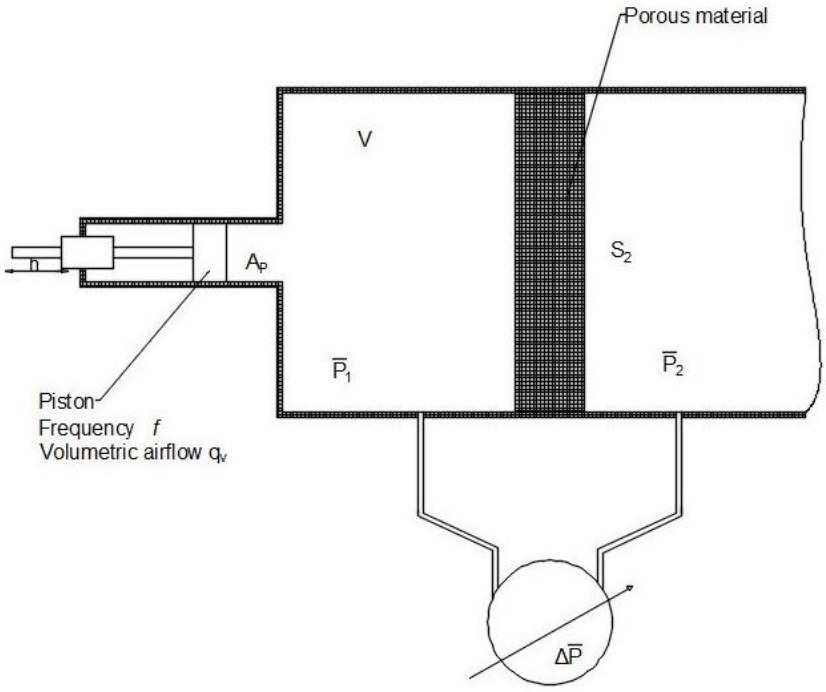

Figure 3. Resistometer use for variable airflow method according to ISO 9053 [2].

As shown in the Figure 3, $u_{r.m.s}$, can be defined as follows:

$$u_{r.m.s} = \frac{\pi}{\sqrt{2}} f h \frac{A_P}{S_2} \tag{16}$$

where f denotes the piston frequency, h is the peak-to-peak range of stroke, A_P is the piston surface area and S_2 is the sample surface area.

The airflow resistivity can be calculated as follows:

$$r = -\frac{1}{u_{r.m.s}} \frac{\Delta P}{l} \tag{17}$$

Based on the measurement requirements for the variable airflow method (illustrated in Figure 3), Mendibil developed the "Resistometer" as shown in Figure 4 [11].

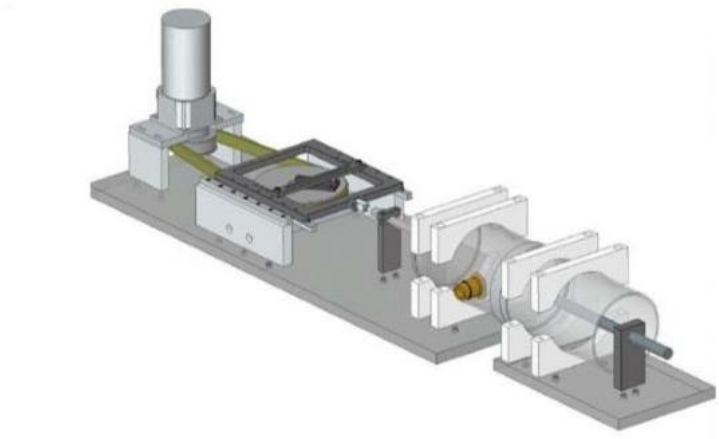

Figure 4. Mendibil's test rig. Image taken from reference [11].

Stinson and Daigle [12] used an electronic system which involved a calibrated laminar flow element of known resistance that was placed in series with the sample materials. The difference in pressure across the laminar element and the sample were measured using electronic manometers of variable capacitance. An electronic flow controller was used to keep steady airflow. The airflow resistivity was estimated using the flow resistance and pressure difference

measurements. According to Pan and Jackson [13], the accuracy of the apparatus in terms of the airflow resistivity was more than 1.6%.

In Bies and Hansen's [14] experimental investigation, the apparatus which they used, met the requirements of American standard ASTM C522-73 [15]. The specimen holder shown in Figure 5 was designed so that it also served as the specimen cutter. To prevent the leakage of air around the edge of sample they used a coating of silicon grease on the cutter. When investigating soft materials they recommended using perforated plates with a large percentage open area. An O-ring seal was used to prevent air leakage around the holder. The funnel shape of the apparatus ensured the flow across the sample surface is uniform. The pressure on the upstream side of the sample is measured using a barocell and a digital manometer. The manometer was capable of measuring differential pressure with a resolution of 0.014 Pa. (The lowest value tested was 1.3 Pa). The airflow was measured using an airflow meter and a control valve to control the flow through the sample. The tested specimens had a diameter of 102 mm [14].

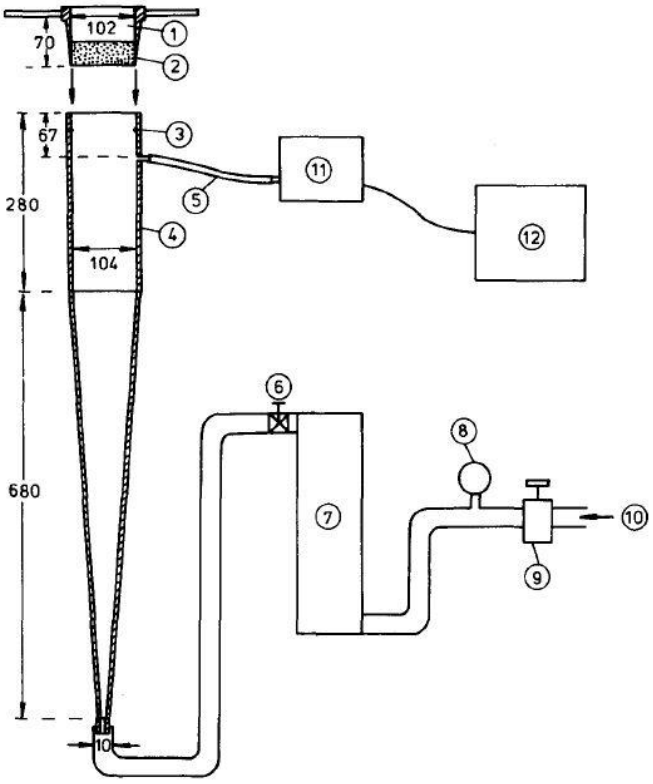

Figure 5. Bies and Hansen's measuring apparatus. Image taken from reference [14].
1). Sample holder and cutter 2). Porous material sample 3). O-ring seal 4). Conical tube to ensure uniform airflow through the sample 5). Tube 6). Valve 7). Flow meter 8). Manometer 9). Pressure regulator 10). Air supply 11). Barocell 12). Electronic manometer

Brown and Bolt [16] used the apparatus shown in Figure 6. By siphoning water from a tank, steady airflow was maintained. As the water flowed, the void was replaced with an equal volume of air. The slowest flow used was approximately 0.1 cm^3/s and the fastest flow was approximately 200 cm^3/s. The pressure difference across the sample was measured using a manometer and connected to the sample holder by a tube. A disc of acoustics material was mounted into a cylindrical container. To prevent air leaks between the sample and the container, the container consists of a slightly conical taper. Brown and Bolt [16] concluded that the airflow resistance varied by 25% for different samples of the same material and it could be measured with an accuracy of ± 2% for a given sample.

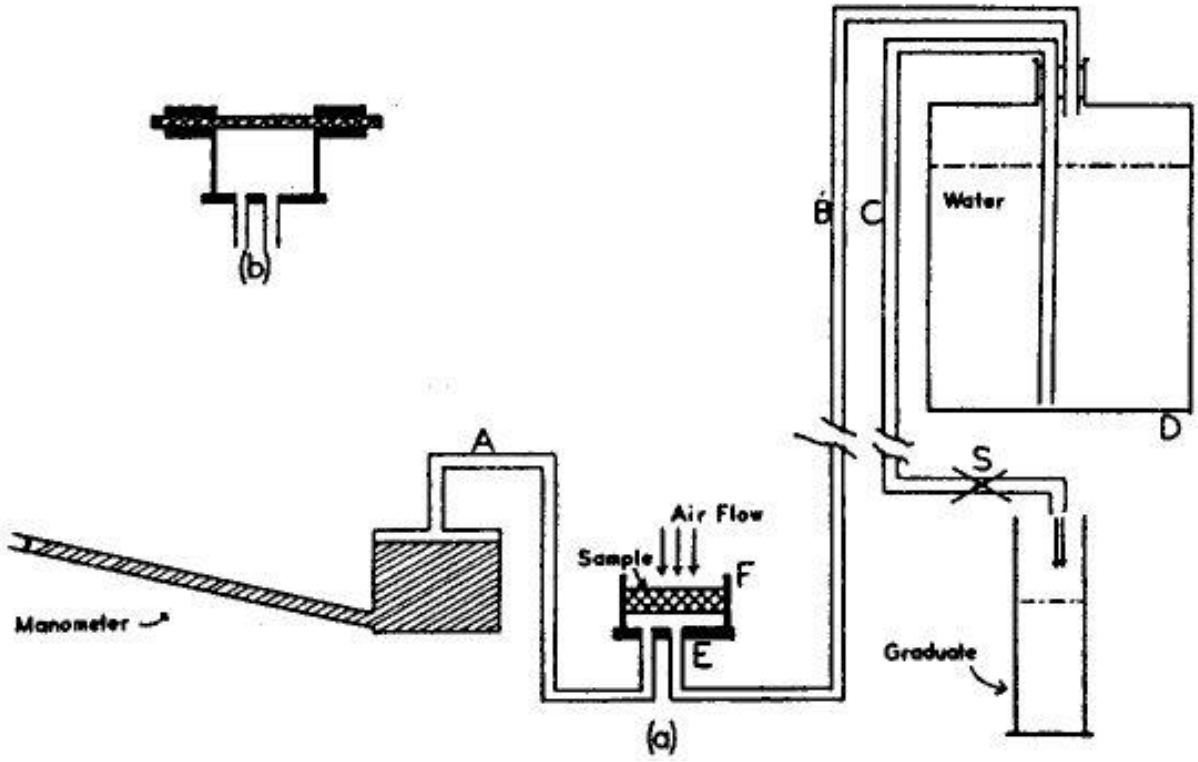

Figure 6. Apparatus used in Brown et al. Image taken from reference [16].

Dragonetti et al [17] performed airflow resistivity experiments on porous materials at room temperature based on the alternating airflow method in ISO 9053-1 [2].They noted that the alternating airflow method required the measurement of sound pressure at a frequency as low as 2 Hz and this posed signal acquisition problems due to inadequacies of typical instrumentation. To overcome those drawbacks, a motor-driven piston was used in the research. Two cavities were associated in the apparatus that they used for the measurements. The side length of two cavities was 10.4 cm and the heights of two volumes were 9.2 and 21.3 cm for the lower and upper cavities respectively. For the apparatus, they selected the vertical

arrangement and the wire net was associated with the sample holder. The cross section of the cavities was chosen according to the requirements of ISO 9053-1 [2] which specified a parallelepiped–like sample holder a square cross section with a side dimension of 90 cm at least. The height of the lower cavity was chosen to be as small as possible for compatibility with the loudspeaker dimensions to ensure its behavior as an acoustic compliance to as high a frequency as possible. The apparatus is shown in Figure 7.

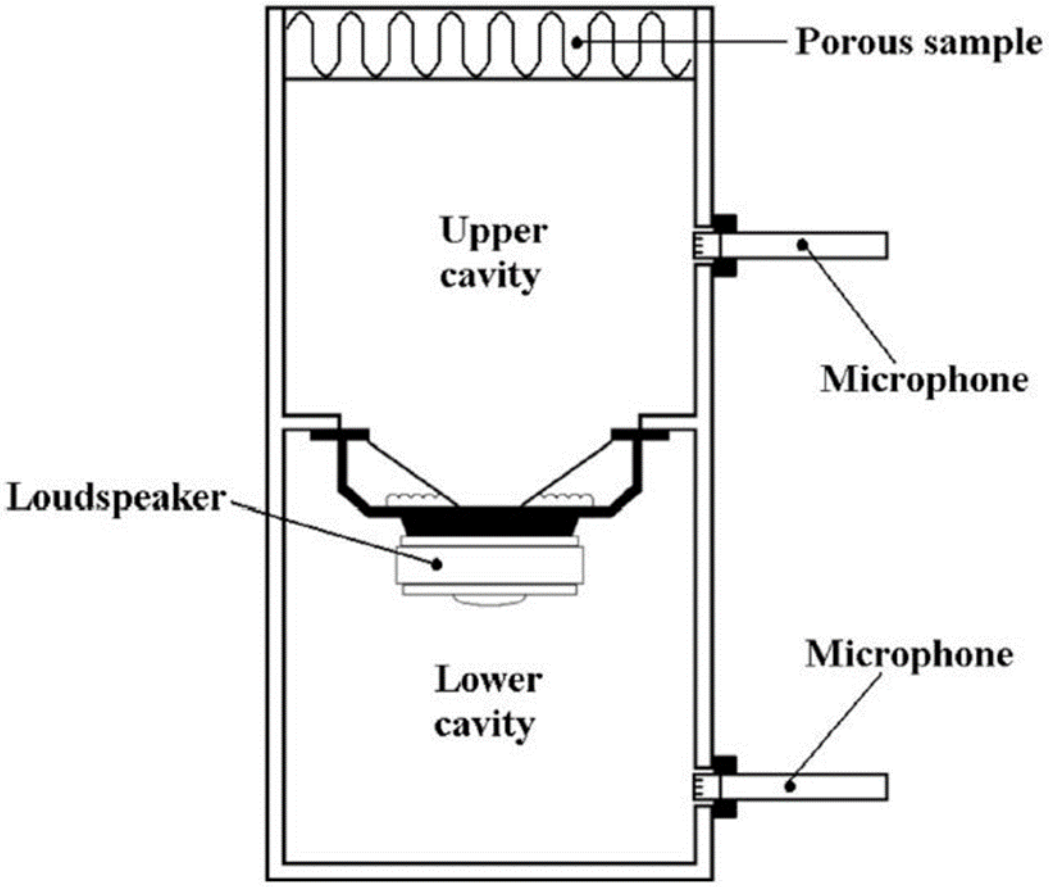

Figure 7. Apparatus used by Dragonetti et al. Image taken from reference [17].

Based on ISO 9053-1 [2], Garai et al [18] conducted airflow resistivity measurements to determine the repeatability and reproducibility standard deviation values. They considered two melamine foam sheets of different thickness and carried out measurements in repeatability conditions either on a single sample or on different samples. They investigated the influence of the sample cutting and non-homogeneity of the foam on airflow resistivity and the results showed that the higher internal repeatability, particularly for single sample. However, the

overall reproducibility was not found to be satisfactory due to systematic deviations that were inherent in the laboratory procedures.

Kino and Ueno [19] measured the surface impedance and physical parameters of seven glass wool samples and six polyester fiber samples with flow resistivity between 4100 and 69,900 Pa.s/m^2. A comparison was made between the measured normal incidence absorption coefficients and normal surface impedance for comparison with the Johnson-Allard model [20, 21] that is considered to be an improvement on the Delany and Bazley [22] empirical model [22]. The Johnson-Allard model required airflow resistivity as an input variable for which measurements were carried out using a device based on ISO 9053-1 [2]. Comparison of measurements with the Johnson-Allard model indicated differences up to 20%. An improved model was developed which introduced a correction factor that was a function of airflow resistivity.

Nichols et al [23] conducted an experiment to investigate the flow resistance characteristics of fibrous material. The apparatus which was used was very similar to the apparatus used by Brown and Bolt [16]. However, there were some modifications added to the apparatus in terms of the techniques of measuring the flow rate and sample holder. The main finding from the experimental data was an empirical relationship between airflow resistivity and fibrous material properties.

Venzke et al [24] experimentally determined the airflow resistance of porous layers normal to their surface without cutting out samples and fitting them in to a sample holder. With its partly radial airflow through the layer under test the method resembled a method for measuring the lateral flow resistance. It was noted [24] that the method can also be used to determine the airflow resistance of the single parts of a combined layer without separating the two components for the measurement provided that the one of larger resistance is thin compared with other.

2.1.2 Empirical models for materials at room temperature

The acoustic properties of fibrous materials relate to the airflow resistivity; hence the sound absorption at room temperature can be modelled with the aid of suitable appropriate empirical

formulae. Usually the airflow resistivity is measured under steady Poiseuille flow conditions for laminar flow speeds.

According to Lambert and Tesar [25], non-negligible flow resistance versus frequency variation can arise in stratified fibrous materials like Kevlar. Therefore, Morse and Ingard [26] suggested using airflow resistivity parameters to define the fluid flow characteristics. In Morse and Ingard's phenomenological approach [26], the equations, in terms of airflow resistivity, relate to motion, continuity and state for one-dimension as follows.

$$\rho_o \frac{k}{\emptyset} \frac{\partial u}{\partial t} + ru = -\frac{\partial p}{\partial x} \tag{18}$$

$$\emptyset \frac{\partial p}{\partial t} + \rho \frac{\partial u}{\partial x} = 0 \tag{19}$$

$$c_0^2(\rho - \rho_0) = \gamma(P - p_0) \tag{20}$$

where ρ_0 is the density of air, c_0 is the speed of sound in air, *k* represents the structure factor and the structure factor to distinguish between mass density and inertial mass density and *u* is the average air particle velocity.

In its more common form, this approach requires the flow resistivity to be a function of frequency to concern the transferring of fluid flow to turbulent from steady state type flow within the material.

Zwicker and Kosten [27], Lambert et al [25] and Biot [28] used a cylindrical pore approximation to quantify the airflow resistance per unit thickness of the fibrous material. The empirical relationship can be presented as a function of the Reynolds number, *Re*, as follows.

$$Re = \frac{d_{\text{fibre}}}{2}\left(\frac{\omega \rho_o}{\mu}\right) \quad (21)$$

where d_{fibre} is the fibre diameter, μ is the air viscosity and ω is the angular frequency of excitation.

According to Zwicker and Kosten [27], for the steady state flow regime (i.e. *Re*<<1), the specific airflow resistance has an empirical relationship with the porosity, $\emptyset$,as follows.

$$r = Re/\emptyset\,(8\mu/d_{fibre}^2) \quad (22)$$

For the Helmholtz flow regime (i.e. *Re*>>1) the airflow resistivity behaves as follows.

$$r = Re/(\frac{\emptyset d_{fibre}}{2})\sqrt{2\mu\omega\rho_o} \quad (23)$$

Picard et al [29], and Ren and Jacobsen [30] investigated the airflow resistivity for transient flow regimes.

Delany and Bazley [22] provided the first comprehensive empirical relationship for the airflow resistivity and sound absorption at the room temperature. This model estimates the impedance of the porous material assuming that the material has a rigid skeleton. Qunli [31] and Cummings [32, 33] later verified this model using a large amount of experimental data for plastic foams. The model correlates the characteristic impedance and the propagation constant to the airflow resistivity of the material. Further improvements were made to Delany and Bazley original model to give the Johnson-Allard model [20].

Bies and Hansen [14] developed these empirical relationships for the magnitude and phase of the complex density and complex compressibility. They built up the relationship based on properties of porous fibrous materials in which the gas was air, however, these plots can be

applied to any gas. The empirical relationships were used to calculate four quantities; complex density modulus and phase, complex compressibility modulus and phase flow.

Empirical models are highly advantageous as in many cases they only need a single input variable, airflow resistivity, which is measurable. However, their limitation is that they may only be applicable to one type of porous material.

2.2 Measurements of airflow resistivity at high temperatures

For measurements at high temperatures, Christie [34] determined the Delany and Bazley [22] coefficients for rock wool (Stillite SR5) at 19, 255 and 490 ℃ using measurements of airflow resistivity. Christie [34] designed the sample chamber to fit into a standard laboratory kiln that had a working area of 150 mm × 175 mm × 350 mm. Steady airflow was provided through a bottled air supply and the speed of the airflow can be varied up to 1 m/s. Each sample has a diameter of 100 mm and the length of the sample chamber is also 100 mm. The sample is retained at each end of the chamber by 12 mm open wire mesh attached to retaining rings. To cut samples they used a cylindrical tubular cutter with a sharp bevelled edge. The cutter dimensions ensured that the samples had a tight fit in the sample chamber. A preheater filled with high density mineral wool was used to ensure that the air entering the sample is at the correct temperature and the flow is uniformly distributed. They reduced the level of airflow leakage to 1% and the temperature at each end of sample is measured by thermocouples. The volumetric flow of air is measured by a flow meter (Gapmeter) before it enters the specimen holder, and the actual volume flow of air through the sample is calculated by correcting the flow meter reading. Christie [34] measured the pressure difference across the sample using a tilting tube manometer. The configuration of the test rig used by Christie [34] is shown in Figure 8.

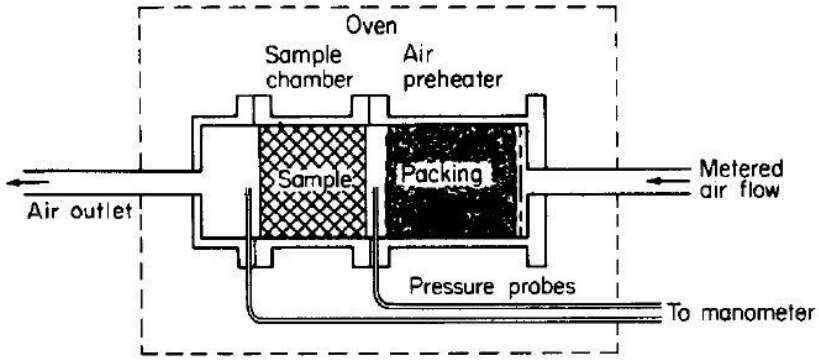

Figure 8. Flow resistance apparatus. Image taken from reference [34].

For measurements at high temperatures, the apparatus was heated to 490 °C and the air was passed through the sample until the temperature at each end of the sample was steady before readings were taken of pressure difference and volume flow. To heat the acoustic apparatus they used a kiln. Measurements were carried out on a sample cut from a standard 600×900×500 mm semi rigid board of starch bonded mineral wool (nominal density of 80 kg/m^3). The flow velocity for measurements was in the range between 1 and 4×10^{-2} m/s. The measured flow resistance varied between 15,000 and 27,500 Pa.s/m^2. It was found that the airflow resistivity for Stillite SR5 was proportional to the $\approx0.6^{th}$ power of the absolute temperature and that the airflow resistivity increased at a lower rate above 400°C. There was no change observed in the flow resistance due to the thermal cycling of the material and the flow resistance measured at a particular temperature did not seem to depend on flow velocity within the range of velocities that they used [34].

Christie [34] also carried out acoustic impedance measurements at high temperature based on closed cavity experimental apparatus that was previously described by Mawardi and Wigan [35]. This allowed comparison of the measured impedance with that predicted from the Delaney and Bazley empirical formula [22]. This indicated the potential to use the Delaney and Bazley empirical formula over a wide temperature range [22].

Miglietta et al [36] measured the variation of airflow resistivity due to temperature using the alternating flow method. They noted that the effect of temperature was expected to change the airflow resistivity due to variation of the air viscosity and thermal expansion of the material. The measurement equipment was installed in a standard laboratory climatic chamber. Steel and aluminum materials were used for the realization of the measurement apparatus to allow the

measurements to be performed in a range of temperatures between -20 and 50 ℃ without operational variations occurring due to thermal expansion. This temperature range was chosen as being of relevance to sound absorbent materials installed in automotive vehicles. The apparatus is illustrated in Figure 9. The experimental results indicated that the airflow resistivity data, as a function of temperature, increases within a power law to the 1.2^{th} power, when airflow resistivity increases. However, this temperature range is significantly lower than that investigated in this research with AES materials.

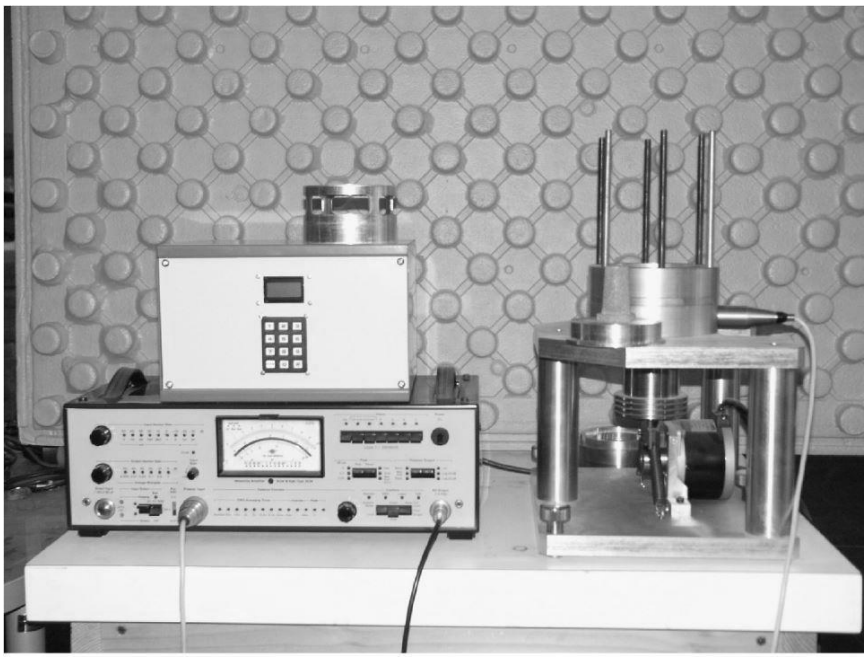

Figure 9. Apparatus used by Miglietta et al. Image taken from reference [36].

For this research it was decided to adopt the main features of Christie's [34] test rig which was the preheating chamber. However, other features were design to specifically suit the measuring instrument, other supporting elements (such as air supply) and environmental constraints (such as the kiln type, kiln orientation and the external temperature).

2.2.1 Empirical relationships for airflow resistivity at high temperatures

After modifying the flow resistivity to account for the higher temperatures Christie [34] demonstrated considerable agreement between both Delany and Bazley model [22] and Christie's model [34]. Christie [34] concluded that the power law relationship for the flow resistivity was successful. The characteristic impedance $Z_{o,pm}$ is a complex number which can

be denoted in the form of *A+iB*. According to Delany and Bazley [22], *A* and *B* can be expressed in terms of airflow resistivity and frequency parameter. Therefore, Christie's [34] modified empirical formulae can be expressed as follows:

$$\frac{A}{\rho_0 c_0} = 1 + 0.0566 \left(\frac{1}{X}\right)^{0.754} \tag{24}$$

$$\frac{B}{\rho_0 c_0} = -0.0861 \left(\frac{1}{X}\right)^{0.732} \tag{25}$$

where the frequency parameter *X* is given by:

$$X = \rho_0 f / r \tag{26}$$

The formulae above are based on air density (ρ_o) of 1.19 kg/m^3 and for temperature and pressure of 20 ℃ and 750 mm respectively.

However, according to Wang et al [37, 38], the acoustic properties at room temperature are not always dependent on the air density. As mentioned in above section, Giese et al [39] carried out research on novel porous sound absorbent ceramic tiles as heat shields in combustion chambers with respect to their sound absorption. For this, a theory describing the bulk properties of a homogenous porous absorber layer was combined with a transfer matrix approach to account for the temperature gradient within the absorber.

Usually, the acoustic losses are mainly caused by viscous friction of the gas and because of that, the airflow resistance of the material is the most important parameter with respect to sound absorption. According to Giese et al [39], there are two different approaches to measure the bulk properties. i.e. two load method or two source method and the Theory of Homogenous Medium (THM) method. The two load or two source method establish the parameters by

measuring acoustic transfer functions in front of and behind the sample and the theory of homogenous medium follows a phenomenological approach. According to the literature [39], the THM originated from the theory of lossy electrical conductors. In Giese et al [39] investigations, they selected the THM method as the most appropriate method since it allows the calculation of Z_a and τ_a using measurable microstructure properties of the observed material such as porosity $\emptyset$, airflow resistivity r or structural factor x. The structural factor *x* is defined as the proportion of volume porosity to surface porosity and is often described as the ratio of total pore volume to the pore volume, which is directly involved in sound propagation while the rest of the pore volume acts as a spring.

According to Giese et al [39], the values of $\emptyset, r, k$ are not independent. Normally, a high porosity obtains a lower airflow resistance and vice versa. However, the value *k* depends on the pore size distribution and the pores are connected. THM can be used for a wide field of absorbent material, such as traditional used fibres, metallic fibres, and porous ceramic structures. Based on THM, the connection between Z_a , τ_a , Ω can be expressed as follows.

$$Z_a = \frac{Z_{o,\mathrm{pm}}}{\emptyset} . \sqrt{\frac{k}{\gamma}\left(1 - \frac{i}{\Omega}\right)} \tag{27}$$

$$\tau_a = k_{\mathrm{pm}} . j \sqrt{\gamma . k . \left(1 - \frac{i}{\Omega}\right)} \tag{28}$$

$$\Omega = k \frac{2\pi f \rho_o}{\emptyset r} \tag{29}$$

where Z_a is specific impedance (kg/m^{2}s), $\emptyset$ is volume porosity, γ is heat capacity ratio; *i*= $\sqrt{-1}$, Ω is a frequency variable and τ_a is the propagation constant (1/m).

Giese et al [39] performed high temperature experiments on an absorption layer to investigate the relationship between porosity and airflow resistance at high temperatures. Through

numerous observations and regression analysis, they found the following relationship between r and $\emptyset$:

$$r \sim (1 - \emptyset)^{1.5} \tag{30}$$

Giese et al [39] built the empirical model for porous ceramic foams which have a porosity between 0.8 and 0.9. Note that in this project the typical porosity of AES materials is 0.95.In this research the aim is to build up an empirical model based on experimental data for the airflow resistivity of AES material up to 800 ℃.

2.3 Summary

It is concluded that the use of direct airflow method for high temperature airflow resistivity measurement is preferable because the variable airflow method requires microphones that work at high temperatures as well as other expensive equipment that needs to be kept at a cool operating temperature. Hence, the direct airflow method was used for room temperature and high temperature airflow resistivity measurements of porous materials. The room temperature test rig was designed according to the ISO 9053-1 and ASTM C522 standards. For high temperature test rig, some features of Christie [34] test rig were incorporated such as the preheater to ensure that the temperature of the air in the specimen holder is at the correct high temperature.

Although the empirical relationship of Christie [34] for airflow resistivity was valid over the temperature range of the acoustic measurements, Christie [34] only measured up to 490 °C which can be considered a practical upper limit for the usability of rock fibrous material.

Chapter 3. EMPIRICAL THEORY

3.1 Empirical relationships between airflow resistivity and material properties

As airflow resistance depend on various material properties, studies have been carried out to build up empirical relationship between airflow resistance and the physical properties. In Bies and Franken [40] and Nichols et al [41], empirical relationships were established between airflow resistance and bulk density for mineral wool, such as glass and rock wool. The empirical relationship can be expressed as follows [40, 41].

$$r = \frac{K_1 \rho_{\text{bulk}}^{1+k_2}}{d_{\text{fibre}}^2} \tag{31}$$

where k_1 is a constant for a fibre material that is manufactured particular way, k_2 is a constant that depends upon fibre orientation and d_{fibre} is the fibre diameter and units used are microns. For one type of mineral wool with a known average fibre diameter, the constant K_1 and K_2 can be found from measured airflow resistivity data for a range of bulk densities. Bies et al [14] plotted $\log r$ against $\log \rho_{\text{bulk}}$ and determined K_1 and K_2 through linear regression. Hopkins [6] carried out a large number of measurements on rock wool and found that K_1=353 and K_2=0.63 for the lateral airflow resistivity for the bulk density range varying from 31 to 155 kg/m^3. For the longitudinal airflow resistivity the values for K_1 and K_2 are 780 and 0.59 respectively for a bulk density range between 38 and 162 kg/m^3. To cover the full density range for a material it may be necessary to have more than one empirical relationship. This can occur with fibrous materials that can be produced in a wide range of fibre diameter. However, for materials other than rock wool the above empirical relationships may not be appropriate [6].

According to Bies and Hansen [14], an empirical relationship between flow resistivity, fibre diameter and fibre density for fiberglass batts and blankets is known to be of the form:

$$r d_{\text{fibre}}^2 \rho_{\text{fibre}}^{-1.53} = constant \tag{32}$$

This equation assumes uniform fibres (uniform fibre diameter less than 15 μm) and negligible binder content to give a constant of 3.8×10^{-9}. However, for polyester fibres, the fibre diameters are uniform for a given denier, the binder is in the form of binding polyester fibres rather than sprayed thermocuring resin. Therefore, Narang et al [42] investigated the effect of material parameters such as mass or area, fibre type, crimpness and binding fibre content. Narang [42] measured the airflow resistivity of polyester fibre materials in order to determine the suitability of an empirical prediction equation developed for fiberglass to polyester fibres. The equation relating the airflow resistivity to the number of fibres per volume was as follows:

$$r = 4.44 \times 10^{-6}.N - 19 \approx 4.44 \times 10^{-6}.N \tag{33}$$

where N is the number of fibres per m^3.

By applying the Bies-Hansen equation [14] to polyester fibre samples, Garai and Pompoli [18] found that the airflow resistivity values were grossly underestimated. They concluded that this was a result of polyester sample having larger fibre diameters than the fibre glass samples Bies-Hansen [14] originally modelled. Therefore, the constants of 1.53 and 3.18×10^{-9} which were fitted in the Bies–Hansen model [14] were not sufficiently accurate for the prediction of the actual value of airflow resistivity. Garai and Pompoli [18] proposed another two values for the equation instead of above mentioned constants. They modified the Bies and Hansen equation [14] as follows:

$$r = A\rho_{fibre}^{B} \tag{34}$$

where A= $3.18 \times 10^{-9} d_{fibre}^{-2}$ and B=1.53. According to Garai and Pompoli [18], A and B are free parameters and can be calculated for varying sample compositions to obtain the best fit. They reported that values of A= 25.989 and B=1.404 provided the best fit for polyester fibres. Furthermore, Garai et al [18] presented their analysis of four different types of fibrous

materials, the binder fibre percentage did not seem to affect the precision of the equation and it was not affected by surface smoothing treatments.

By considering, Bies and Hansen [14] and Garai and Pompoli [18] equations, it can be concluded that the airflow resistivity of a sample is inversely dependent to the fibre diameter squared. However, the coefficients in these equations differ from each other [43, 44].

Attenborough [45, 46] developed an empirical model which predicts the airflow resistivity of rigid fibrous absorbents such as sands and soils which was same as Kozeny-Carmen [43] based on the characteristic length l. The airflow resistance per unit length in a single pore, r_p, can be presented as follows

$$r_p = \frac{8\mu s}{l^2} \tag{35}$$

where s denotes the steady flow or static shape factor which is equal to one if the pore is cylindrical and to 1.5 if the pore is parallel side slit. If the pore has a cylindrical shape, the characteristic length is equal to the radius and equal to semi width if the pore is parallel side slit [47].

In addition, the fluid velocity, averaged over a single pore's cross section $,\langle v\rangle$, can be related to the velocity u, averaged over unit cross section of the porous medium can be denoted by as follows.

$$\langle v\rangle = qu/\emptyset \tag{36}$$

where $\emptyset$ is the volume porosity of connected pores and q is the tortuosity factor.

Based on the above formulae, the pressure gradient along a stream line in a single pore during laminar flow gives,

$$-\frac{dp}{dx} = q^2 r_p \frac{u}{\emptyset} \tag{37}$$

In Attenborough's approach [46], by assuming that all of the pores are identical, the flow resistance through a porous medium can be denoted as follows.

$$r = \frac{8\mu q^2}{l^2 \emptyset} \tag{38}$$

The Voronina model [48] is another model which is based on the porosity of a material. This model uses the frequency, porosity of the material and the average pore diameter for defining the acoustical characteristics of the material. They extended the empirical model for porous materials with a rigid frame and high porosity and compared the model with Attenborough's approach [47]. There can be seen a significant agreement between both model and the structural characteristic, *Q*, which represents the quantitative estimation of the energy losses in the porous medium is defined as follows [49].

$$Q = \frac{(1-\emptyset)}{\sqrt{\emptyset} d_{fibre}} \sqrt{\frac{200\mu}{2\pi\rho_o}} \tag{39}$$

where the air viscosity μ=1. 85×10^{-5} Pa.s.

3.2 Empirical relationships between airflow resistivity and characteristic impedance

The characteristic impedance for air in a porous material, $Z_{0,pm}$, can be defined as the ratio between the acoustic pressure (*P*) and volume velocity (*U*) [6].

$$Z_{0,pm} = \frac{P}{U} = \rho_{\text{eff}} c_{\text{pm}} \tag{40}$$

where ρ_{eff} is the effective density and the sound velocity through the porous material , c_{pm}, is given by

$$c_{pm} = \sqrt{\frac{1}{\emptyset \rho_{\text{eff}} k_{\text{eff}}}} \tag{41}$$

Characteristic impedance is a measure of the ability of a sound wave propagates through a particular medium and can be calculated from the effective density and the effective gas compressibility k_{eff}. The effective density and the effective gas compressibility can be calculated if the structure of the porous material can be represented using idealized geometry [6, 50].

As note in previous sections, Delany and Bazley [22] provided the first comprehensive empirical relationship relating airflow resistivity to the characteristic impedance at room temperature. Delany and Bazley [22] investigated the acoustical properties of a range of fibrous absorbent materials. The propagation of sound in an isotropic homogenous material is determined by the characteristic impedance and the propagation coefficient. The characteristic impedance and the propagation coefficient can be easily evaluated by using the specific flow resistance per unit thickness and the specific flow resistance is mainly depended on the bulk density and the fibre diameter [51]. Measured values of characteristic impedance and propagation coefficient were used with measured airflow resistance to give simple power law functions. Delaney and Bazley provided empirical expressions derived from many measurements as follows [22].

$$Z_{0,pm} = \rho_0 c_0 [1 + 0.0571 X^{-0.754} - i 0.087 X^{-0.732}] \tag{42}$$

$$k_{pm} = \frac{2\pi f}{c_0}[(1 + 0.0978X^{-0.700}) - i0.189X^{-0.595}] \quad (43)$$

where, k_{pm} is for complex wave number and $c_0$is representing the sound velocity of the air, and *X* is the frequency parameter.

Delaney and Bazley [22] proposed the following bounds for the validity of their empirical expressions in terms of the frequency parameter as follows:

$$0.01 < X < 1.0 \quad (44)$$

However, based on measurements, Bies [40] suggested the following limits for small and large values of the frequency parameter *X*;

$$\lim_{x\to 0}(|\rho_1|/\rho_0) = r/\rho_0 2\pi f \quad (45)$$

$$\lim_{x\to 0} \emptyset = -\frac{\pi}{2} \quad (46)$$

$$\lim_{x\to 0}(|K|/\gamma P) = \frac{1}{\gamma} \quad (47)$$

$$\lim_{x\to 0} \emptyset = -\frac{\pi}{2} \quad (48)$$

$$\lim_{x\to 0}(|K|/\gamma P) = \frac{1}{\gamma} \quad (49)$$

$$\lim_{x\to 0} \theta = 0.0 \tag{50}$$

$$\lim_{x\to \infty} (|\rho_1|/\rho_0) = 1.0 \tag{51}$$

$$\lim_{x\to \infty} \emptyset = 0.0 \tag{52}$$

$$\lim_{x\to \infty} (|K|/\gamma P) = 1.0 \tag{53}$$

$$\lim_{x\to \infty} \theta = 0.0 \tag{54}$$

As noted in the following literature [52, 53, 54], the empirical expressions of Delaney and Bazley [22] approach the correct limits and therefore, the upper bound which they proposed may be relaxed. Delany and Bazley's [22] equations can be used to determine ρ_1 and *K* for medium and large values of the frequency parameter. However, their empirical expressions do not approach the correct lower limits and an alternative means is for necessary to calculate ρ_1 and *K* small values of the frequency parameter.

In addition to Delany and Bazley's [22] empirical relationships between the airflow resistivity and the characteristic impedance, Allard et al [21] provided alternative expressions. Allard's equations [21] provide similar predictions as Delany and Bazley [22] in the range of validity. However, their equations are valid at low frequencies where the equations of Delany and Bazley provide non-physical predictions. These equations were built on the general frequency dependence of the viscous forces in porous materials proposed by Johnson et al [55]. In Allard et al's [21] approach they considered two functions which had different frequency parameter values, $F_1(X)$ and $F_2(X)$ respectively.

$$F_1(X) = (1 + i\pi(X))^{\frac{1}{2}} \tag{55}$$

$$F_2(X) = \left(F_1((X)4N_{pr}\right) \tag{56}$$

where N_{pr} is the Prandtl number.

The relationship between the characteristic impedance and the frequency parameter (which can be considered as the function of airflow resistivity) is given by [21]

$$Z_{0,pm} = \left(\left(1.2 + (-0.0364X^{-2} - i0.1144X^{-1})^{\frac{1}{2}}\right)\left(101320\frac{i29.64+(2.82X^{-2}+i24.9X^{-1})^{1/2}}{i21.17+(2.82X^{-2}+i24.9X^{-1})^{1/2}}\right)\right)^{1/2} \tag{57}$$

The equation is valid for atmospheric pressure of 101,320 Pa, air density of 1.21 kg/m^3, a Prandtl number of 0.702 and a specific heat capacity ratio of 1.4.

As an improvement on the Delany and Bazley model [22], Yasushi et al [56] published an empirical model giving a relationship between the characteristic impedance and the airflow resistivity. They applied modifications to the Delany and Bazley [22] model in order to improve the model across a broader frequency range, where

$$Z_{o,pm} = 1 + 0.070\left(\frac{X}{\rho_0}\right)^{-0.632} + i0.107\left(\frac{X}{\rho_0}\right)^{-0.632} \tag{58}$$

From Voronina's approach [48], the characteristic impedance was calculated based on the structural characteristic parameter by means of the following simplified equations.

When Q<1

$$Z_{o,pm} = (1 + Q) - i\frac{Q}{2} \tag{59}$$

When Q>1

$$Z_{o,pm} = (1 + Q) - i\frac{Q}{2+Q/(1+\sqrt{Q})^2} \quad (60)$$

Although these empirical models are highly advantageous since they only need a single input, flow resistivity which is easily measurable, they are only suitable for one type of material and a certain frequency ranges [57].

The model from Mechel and Vèr [58] differentiates two families of absorbing materials and two areas for the normalised frequency parameter of X. According to Beranek and Vèr [58], the Mechel and Vèr model [58] can be considered as a more refined adjustment than the Delany–Bazley model [22]. The defined an empirical relationship for the characteristic impedance in Mechel and Vèr model [58] as follows:

$$Z_{o,pm} = \rho_o c_o(1 + b'X^{-\beta'} - ib''X^{-\beta''}) \quad (61)$$

The values of the coefficients and exponents are summarised in Table 2.

Table 2. Characteristic impedance calculation: Coefficients and exponents of the Mechel-Vèr model [58].

Material	Region	b'	β'	b''	β''
Rock wool and basalt	$X \leq 0.025$	0.0810	0.699	0.1910	0.556
	$X > 0.025$	0.0563	0.725	0.1270	0.655
Fibre glass	$X \leq 0.025$	0.0668	0.707	0.1960	0.549
	$X > 0.025$	0.0235	0.887	0.0875	0.770

3.3 Empirical relationships for airflow resistivity, air viscosity and temperature

The viscosity, η of a gas was first defined by Maxwell [59, 60] showing that it was independent of static pressure, except at very low (< 0.02 atm) and very high pressures (> 1 atm) [59, 61]. Maxwell's kinetic theory of gases also showed that viscosity was proportional to the square root of the absolute temperature [62].

Maxwell's [59, 60] kinetic theory is given by Maitland et al [63] as

$$\eta(T) = \frac{5\sqrt{\pi M/N_A k_B T}}{16\pi\delta^2} \tag{62}$$

where N_A is the Avogadro constant, k_B is the Boltzmann constant, δ is the Lennard-Jones diameter, and M is the molecular mass.

However, Sutherland [64] noted that experimental work with natural gases showed that viscosity changed more rapidly with temperature and was proportional to T^n where n ranged from 0.7 for hydrogen to 1.0 for less perfect gases.

Following from Equation 63, Giese et al [39] developed theory to predict the absorption coefficient at different temperatures and noted that the airflow resistance, $r(T)$ at a temperature, T, is a function of air viscosity as follows:

$$r(T) = \frac{r_0}{\eta_0}\eta(T) = \frac{r_0}{\sqrt{T_0}}\sqrt{T} \tag{63}$$

where r_0 and η_0 are the airflow resistance and air viscosity respectively at a specified temperature, T_0.

Based on the Poiseuille law, Miglietta et al [65] noted from Biot [66] that for air flowing through a capillary in the low-frequency range, the airflow resistance is directly proportional to air viscosity such that

$$r(T) \propto \frac{8\eta(T)}{a_{eq}^2(T)} \tag{64}$$

where $a_{eq}(T)$ is the radius (m) of the capillary at a temperature, *T*.

Hence when relationships are sought between the airflow resistance and temperature it is reasonable to assume that airflow resistance will be proportional to T^n because airflow resistance is directly proportional to air viscosity. Miglietta et al [65] carried out measurements between 0 and 30°C on a range of materials (including generic materials such as polyethylene, rubber, glass wool, rock wool, cotton waste, polyester) and showed that the airflow resistivity varied with $T^{1.2}$.

Christie [34] stated that the air viscosity varied with $T^{0.7}$; however, no reference was given to indicate the source of the exponent of 0.7. In this work Sutherland's equation [64] has been used to analyse the relationship between the air viscosity and the absolute temperature. Sutherland's equation is given by [64]:

$$\frac{\eta}{\eta_0} = \left(\frac{T}{T_0}\right)^{3/2} \frac{T_0+T_s}{T+T_s} \tag{65}$$

where η_0 correspond to temperature T_0. If these formulas hold for any given choice of T_0, they also hold for any other choice of T_0. The constant T_s= 110 K for T_0=300 K and η_0= 1.846 × 10^{-5} kg/ (ms). Sutherland's equation is valid for a wider range of temperatures between 100 K and 1900 K. [67]. Using Equation 65, the viscosity η is plotted against a range of absolute temperatures from room temperature to 873 K as shown in Figure 10. Power law regression was then used to identify the exponent for the absolute temperature. This indicates that the air viscosity varies with the absolute temperature where the exponent is 0.68. As this is approximately equal to 0.7 which was quoted by Christie [34] it is assumed that Sutherland's equation was the source of this value.

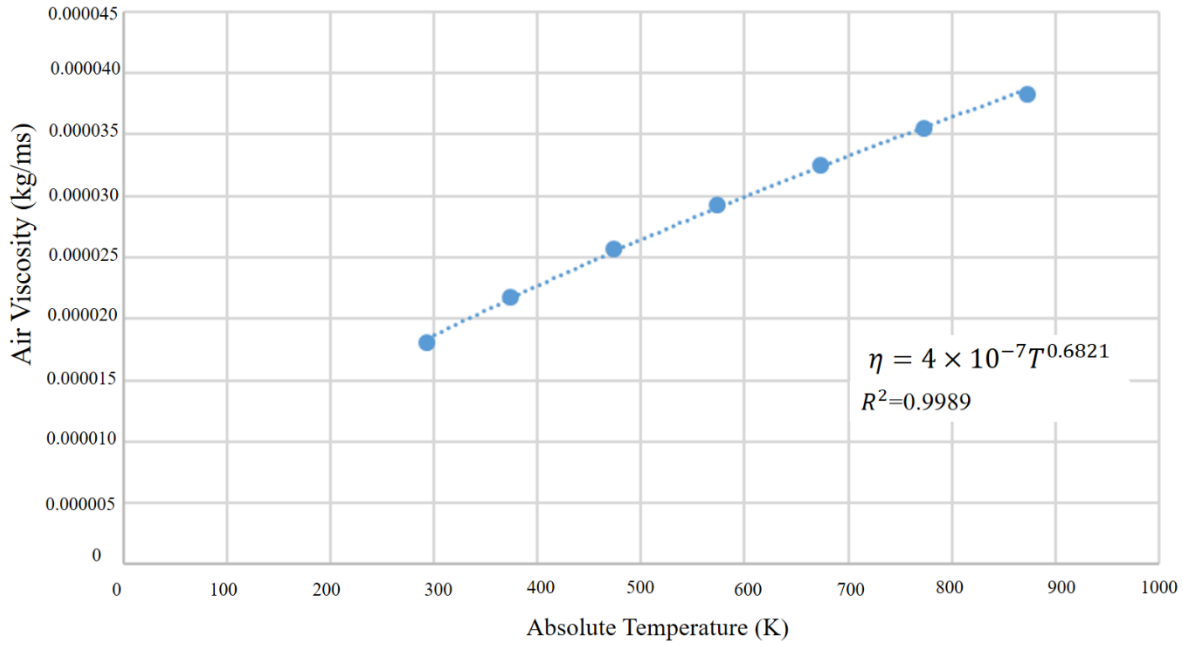

Figure 10. The relationship between air viscosity and absolute temperature according to Sutherland's equation.

Experimental data for constituent gases that make air can be found in tabulated form in the monograph by Present [62] for nitrogen, oxygen and carbon dioxide. These data are plotted in Figures 11 to 13 and power law regression is carried out to determine the exponent values. The exponent ranges from 0.72 to 0.79 which is similar to the value of 0.7 derived from Sutherland's equation [64].

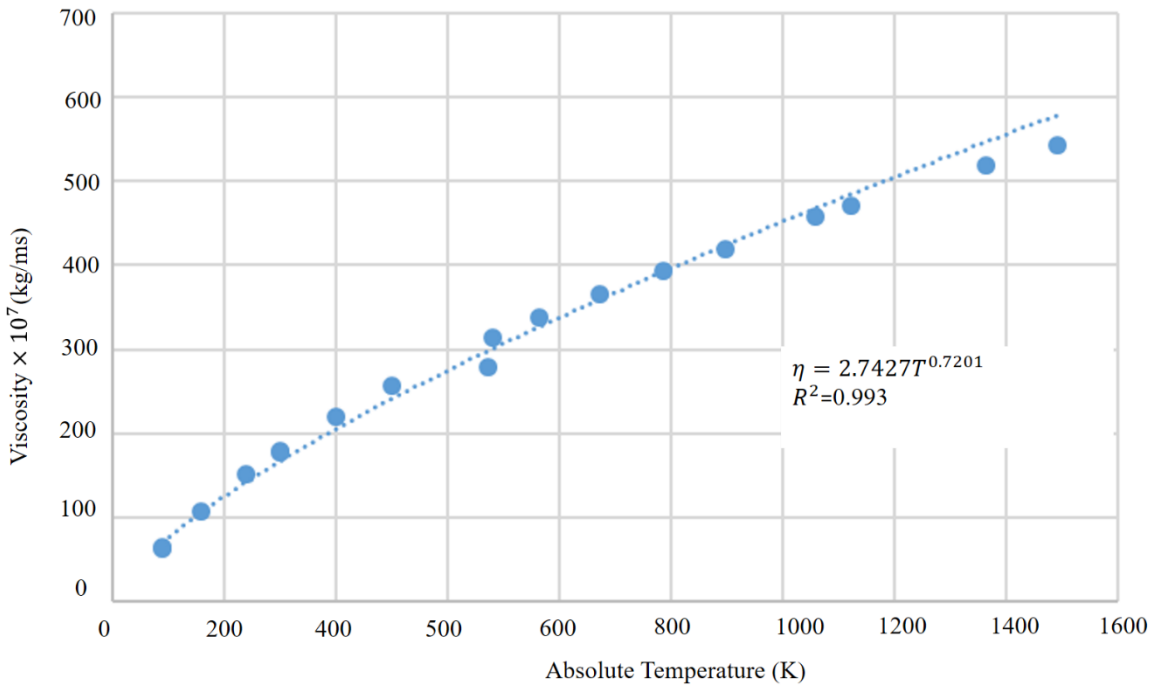

Figure 11. Experimental data for viscosity of nitrogen at different absolute temperatures.

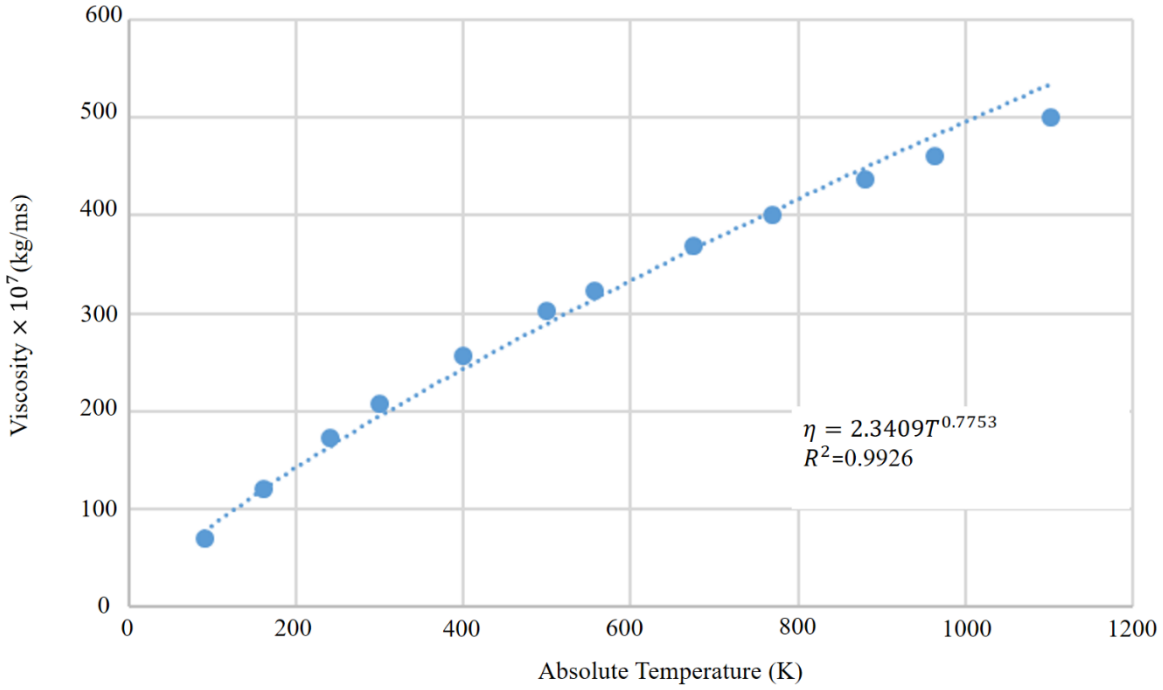

Figure 12. Experimental data for viscosity of oxygen at different absolute temperatures.

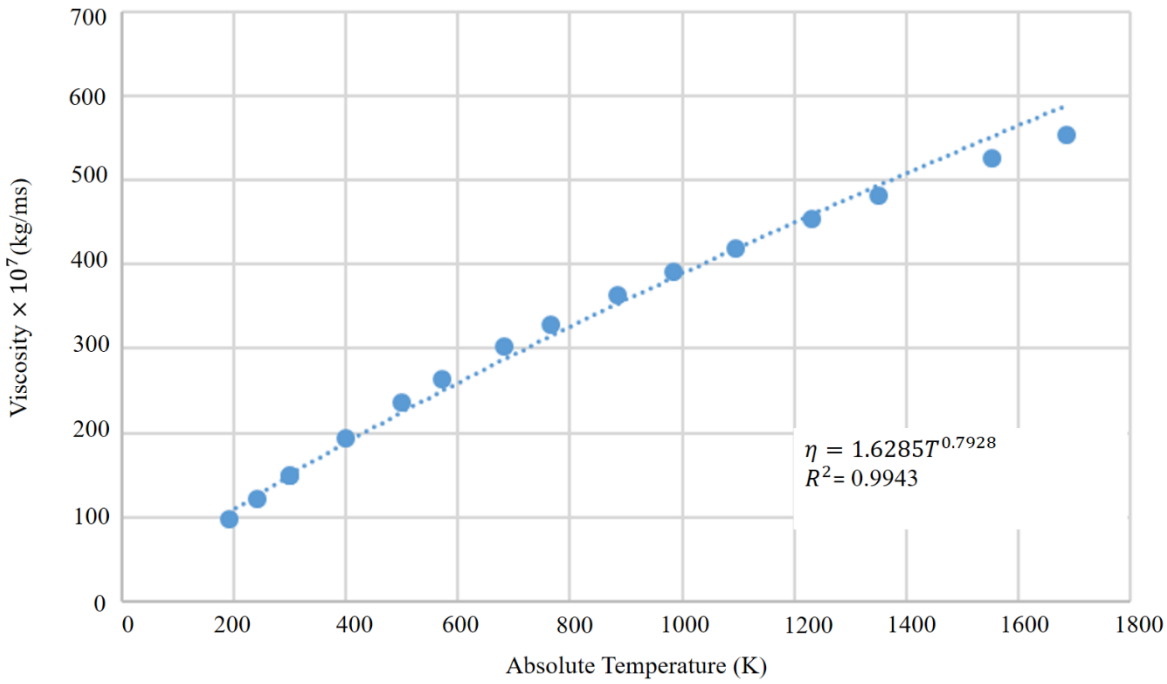

Figure 13. Experimental data for viscosity of carbon dioxide at different absolute temperatures.

3.4 Summary

According to empirical theories of airflow resistivity and material properties, the airflow resistivity of a porous material sample increases with increasing bulk density and is inversely dependent to the fibre diameter squared.

The airflow resistivity can be used to calculate the characteristic impedance and the propagation constant. According to Delaney and Bazley's empirical relationship [9], their frequency parameter which is dependent on airflow resistivity can be used to calculate the both characteristic impedance and the propagation constant. Furthermore, since theory indicates that the airflow resistivity is proportional to the air viscosity and the absolute temperature, it is useful to develop a specific power law relationship between absolute temperature and airflow resistivity (or specific airflow resistance) for AES materials.

Chapter 4. DESIGN OF EXPERIMENTAL APPARATUS

The experimental apparatus assembly for both room and high temperature consists of a specific test rig, differential pressure, flow meter and a pressure regulator. The relevant information regarding to each component is described in this chapter.

4.1 Test samples

The funder supplied ten different AES materials with three different densities as indicated in Table 3.

Table 3. List of AES materials used for the measurements.

Density (kg/m^3)	64	96	128
Material name and ID No.	Superwool® HT-0034 (Material ID No.0034)	Superwool®Plus-0059 (Material ID No.0059)	Superwool®Plus-0058 (Material ID No.0058)
	Superwool®AC2-0048 (Material ID No.0048)	Superwool®Plus-0062 (Material ID No.0062)	Superwool®Plus-0061 (Material ID No.0061)
	Superwool®Plus-0055 (Material ID No.0055)	Superwool®Plus-0064 (Material ID No.0064)	Superwool®Plus-0063 (Material ID No.0063)
	Superwool®Plus-0057 (Material ID No.0057)		
	Superwool®Plus-0060 (Material ID No.0060)		

Cylindrical samples were cut using a 101.8 mm diameter metal cutter. Each sample was weighed using scales (Ohaus Explorer 627) to an accuracy of 0.001 g.

4.2 Measuring equipment for airflow

A Furness Control FCS 523 measuring instrument is used to measure the differential pressure and the airflow rate – see Figure 14.

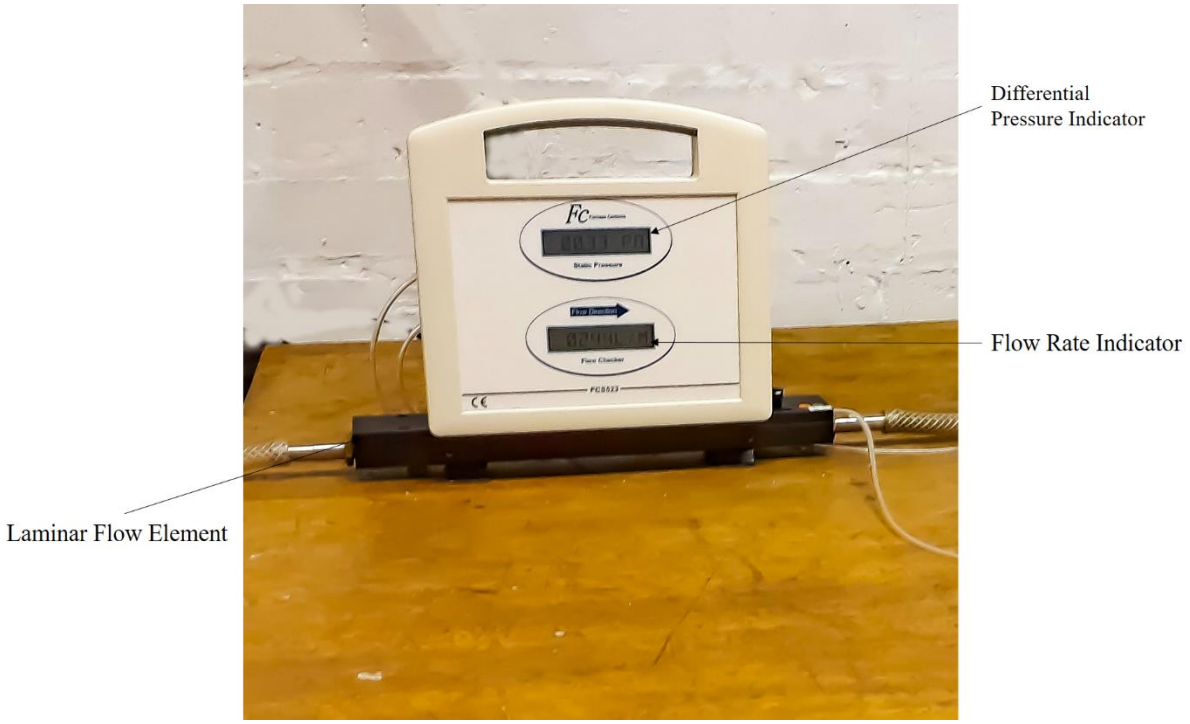

Figure 14. Flow rate and differential pressure measuring instrument.

This consists of two main parts including a laminar flow element and a differential pressure meter. The laminar flow element has the ability to measure volumetric gas flow rates from 0 to 2 l/min. The element measures volumetric gas flow rate and is based on the physics of the Poiseuille equation [68].

$$\Delta P = \frac{8\mu L Q}{\pi r^4} \tag{66}$$

where ΔP is the pressure loss (Pascal), μ is the dynamic viscosity (Pa.s), L is the length of laminar flow element (m), Q is the volumetric flow rate (m^3/s) and r is the radius of the laminar flow element (m).

Since the equation is valid only for incompressible fluids which are Newtonian, the laminar flow element only can be used to measure the flow rate of Newtonian and incompressible flows. The flow is laminar through the pipe of constant circular cross section which is substantially longer than its diameter; and there is no acceleration of fluid in the pipe. Furthermore, the flow element forces the gas flow to be parallel to the pipe. This eliminates flow turbulence and produces a very small differential pressure (ΔP) which is proportional to volumetric flow rate [69]. The linear relationship between differential pressure and the flow of laminar flow element gives a very large turndown ratio. According to the manufacturer, the device generates a very low differential pressure, while offering little restriction to flow, typically a pressure drop of 100 Pa at full flow rate of 2 l/min. The differential pressure device can measure to two decimal places with an accuracy of <0.25%. Only the display was calibrated. The reference flow was measured using a standard laminar flow element and digital micro manometer. For the apparatus, the calibration medium was dry air with a relative humidity less than 80% [70].

4.3 Air supply

Since the measuring instrument for airflow can only withstand pressure ≤300 Pa, it is necessary to reduce the supply air pressure which is at 12 Bar. In addition, it is an essential requirement to dehumidify the supply air before enter to the measuring instrument. By considering all these factors, a pressure regulator with an air filter was used with the main air supply for both room temperature and high temperature experiments. The pressure regulator has the ability to regulate the pressure between 0.5 and 16 bar and it has 5μ m^3 of filtration [71]. The pressure regulator is shown in Figure 15.

ISO 9053-1 [2] and ASTM C522 [7] require a minimum flow velocity of 0.5×10^{-3} m/s, and with the control on this valve it is possible to control the flow to $\pm0.01\times10^{-3}$ m/s. As the cross-section of the sample holders are all 100 mm diameter, this gives the range of volumetric flow rates as between 0.231 and 0.240 l/min. In order to assess the effect of other airflow velocities on the airflow resistance at room temperature and at 800 °C, airflow velocities of 1×10^{-3}, 2×10^{-3} and 4×10^{-3} m/s were also tested; these correspond to sound pressure levels indicated in Table 1.

Figure 15. Pressure regulator with the filter.

4.4 Room temperature test rig

The room temperature test rig was designed to satisfy the requirements of ISO 9053-1 [2], and ASTM C522 [7]. Using the direct airflow method with controlled unidirectional airflow through the test specimen. The test rig consists of three parts; specimen holder, plunger assembly and a metal sleeve. A three-dimensional model was created using AutoCAD software and the drawings are in Appendix A. The fabricated room temperature test rig is shown in Figure 16.

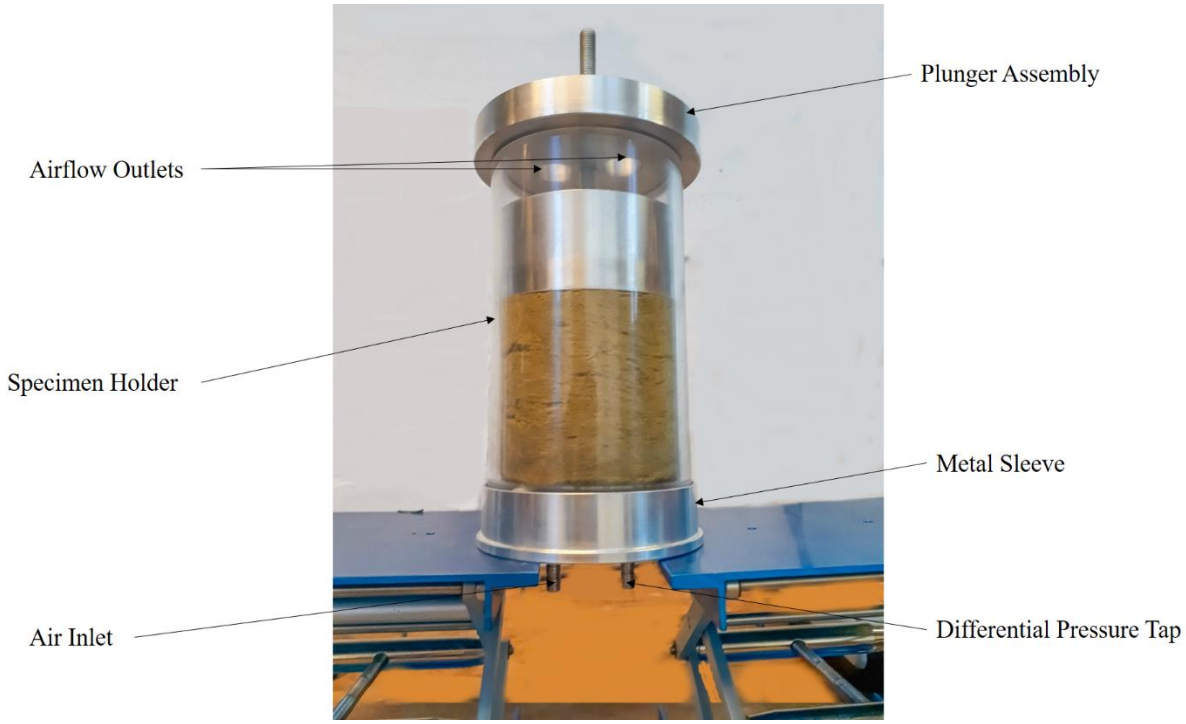

Figure 16. ISO test rig for room temperature experiments.

A transparent material (Perspex) was used to manufacture the specimen holder to allow the position of the test sample to be visually checked. This holder is a cylinder with an internal diameter of 100 mm. The height of the specimen holder is 200 mm. A perforated metal mesh is used to support the sample at the bottom of the specimen holder. The mesh has an open area of 50% which satisfies the requirements in ISO 9053-1 [2] and ASTM C522 [7] standards. The mesh is formed from a metal plate that is perforated with holes of 3 mm diameter.

At the top of the specimen holder is a metal plunger assembly which consists of a lid and a perforated metal screen.

At the bottom of the specimen holder there is a metal sleeve with (a) an air inlet tube (12 mm diameter) and (b) a tube to measure differential pressure (5 mm diameter). The differential pressure is measured between the volume of air underneath the sample and atmospheric pressure.

At room temperature the airflow resistivity was measured using the room temperature test rig, the differential and flow measuring apparatus and the precision air regulator – see Figure 17

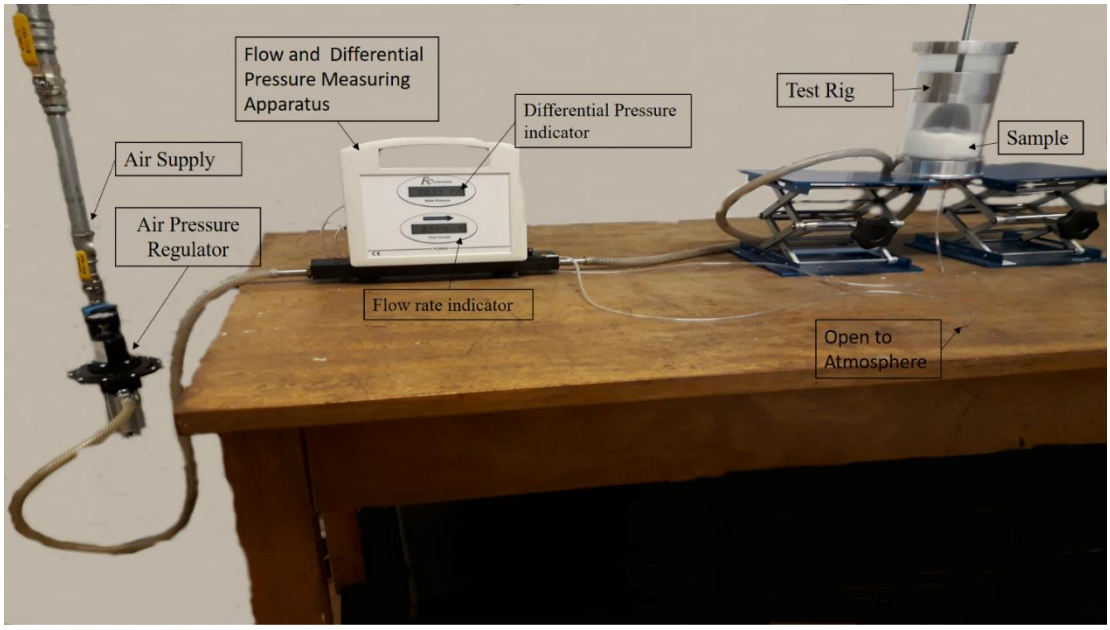

Figure 17. ISO test rig for room temperature measurements and associated measurement equipment.

4.5 High temperature test rig

In order to carry out the high temperature measurements of airflow resistance, it was necessary to design a new test rig that would satisfy the requirements of the ISO 9053-1 [2] and ASTM C522 [7] standards but withstand high temperatures. The following steps describe the design of the high temperature test rig.

4.5.1 Initial design considerations

The test rig for high temperature airflow resistance measurements was designed to give nominally identical results at room temperature to the ISO test rig described in ISO 9053-1 [2] and ASTM [7] standards. However, as it needed to operate at temperatures up to 1000 °C (later the operating temperature was reduced to 800°C), the test rig design from Christie [34] was used as a starting point because it was used up to 500 °C.

Christie [34] introduced a preheater into the design that was packed with high density mineral wool. It was stated that this was necessary to ensure that (1) the air entered the sample at the same temperature as the internal kiln temperature and that (2) the flow of air was uniform across the surface of the sample. The first reason is logical because the cool air from the

compressor reservoir needs to be heated up for a valid measurement. The second reason seems to have been given because the air inlet comes from a tube that has a diameter which is a fraction of the test sample diameter. However, this may not be a critical reason due to the low flow velocity and the fact that a small air inlet is also used in the ISO 9053-1 test rig where no issues have been reported with non-uniform flow through the sample. It is possible that the perforated metal screen helps to avoid such a problem, and this is also incorporated in the high temperature test rig. It is assumed that Christie's [34] preheater achieved the required air temperature because they used thermocouples to check the air temperature. Christie's [34] preheater used mineral wool as the preheater packing but its material properties change significantly above 500 °C [34] so a similar AES material to the test samples was considered instead.

In contrast to the room temperature test rig where the differential pressure was referenced to atmospheric pressure outside the test rig, the high temperature test rig measures differential pressure across the sample because the outlet from the test rig does not enter the kiln. Therefore, it was necessary to measure the differential pressure across the sample.

A three-dimensional model of the high temperature test rig was created in AutoCAD as shown in Figure 18 with additional drawings given in Appendix B.

As shown in Figure 18, the rig consists of a cylindrical specimen holder and cylindrical preheating chamber. There is one air inlet, one air outlet, two outlets for the differential pressure measurement and one tapping point for the temperature probe. The specimen holder has two perforated meshes to hold the sample in place and a preheating chamber consisted of air inlet and the differential pressure meter probe inlet. One mesh is a moveable mesh and the other is fixed in the preheater. The internal diameter of the cylinders is 97 mm (NB It was not possible to purchase 100 mm internal diameter tubes for compatibility with the room temperature test rig) and the specimen holder has a height of 150 mm which allowed vertical orientation of the test rig within the kiln.

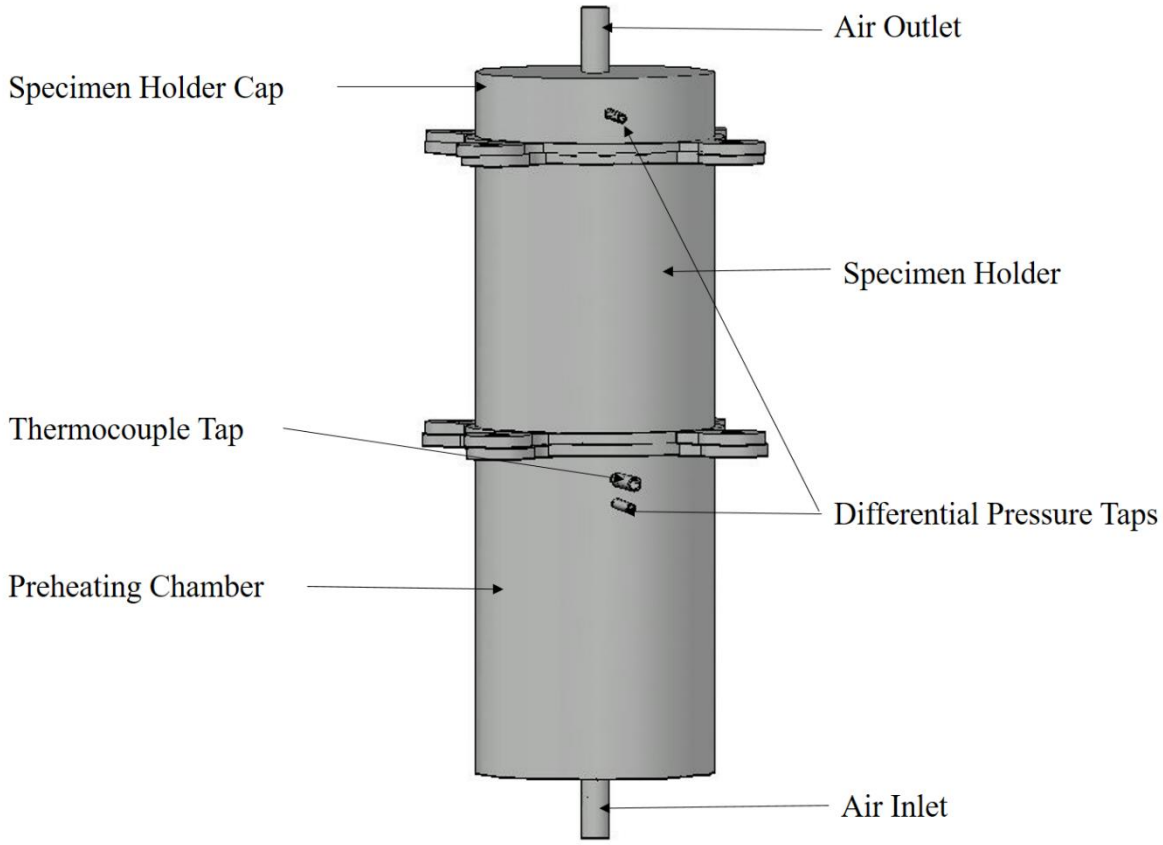

Figure 18. 3D model of high temperature test rig.

4.5.2 Kiln

The kiln used for the high temperature experiments is a front loading, medium-sized kiln (see Figure 19) that was rated for a maximum temperature of 1100 ℃. The kiln case was powder coated steel with internal insulation provided by 2” thick mineral wool and firebricks.

The kiln door is a heavy-duty door with the hinge on the left side. The door can open all the way so that the door opening is completely unobstructed. There is a tadpole gasket around the door for tightness of seal.

To provide uniform distribution of heat inside the kiln, the heavy-duty heating elements are positioned on three sides of the kiln. The kiln has a control panel to set the required temperature and temperature ramp rate.

Figure 19. The Kiln

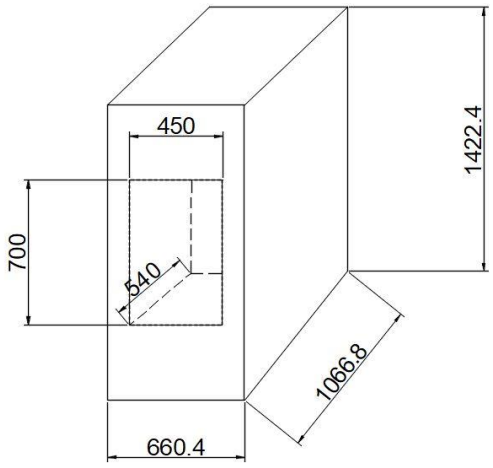

Figure 20. Kiln dimensions.

4.5.3 Assessing a suitable length for the preheating chamber

As the high temperature test rig in this project needed to work up to 1000 ℃ it was necessary to check whether the length of the preheating chamber might need to be significantly longer than that used by Christie [34] to ensure that the air reached the same temperature as the air in the kiln. The process is modelled using Matlab Simulink software to identify a suitable length for the preheating chamber to achieve the required temperature output. It was assumed that heat transfer occurs from the kiln to the preheating chamber due to convection and conduction (ignoring the radiation from the surfaces of the kiln). As it is not possible to simulate fibrous ceramic material as the preheater packing in the simulation, an empty tube is used under the same effective temperature and environmental conditions.

The inside diameter of the preheating chamber is identical to the room temperature test rig (100 mm), and the cylinder is 10 mm thick austenitic stainless steel. Based on these values and the input data below, different lengths for the preheating chamber were modelled until the air in the chamber reached 1373 K (1100 ℃) which was slightly beyond the temperature requirement of 1000 ℃.

According to the simulation results, the air in the preheating chamber reaches 1170 K after it has travelled a distance of 250 mm without preheater material. Hence, 250 mm was proposed as the length of preheating chamber.

The simulation data are as follows

Input data

Room temperature	:	291.15 K (18℃)
Kiln temperature	:	1400.15 K (1127.15℃)

Air at room temperature

Specific gas constant (R)	:	0.287 kJ/kg/K
Density of air (ρ)	:	1.198 kg/m^3
Compressibility factor (Z)	:	0.9999

Specific enthalpy at reference temperature *(h_E)*	:	291.544 kJ/kg
Specific heat at constant pressure (C_P)	:	1.005 kJ/kg/K
Thermal conductivity of austenitic stainless steel (*k*)	:	15 MW/mK

Preheating chamber

Length of preheating chamber (*l*)	:	0.25 m
Thickness (*t*)	:	0.01 m
Outside diameter *($d_{outside}$)*	:	0.11 m

The simulation was built up based on the following equation (67) to include conduction and convection heat transfer from the kiln to the preheating chamber [72].

$$\dot{m}C_p\left(T_{upstream} - T_{\ room}\right) = hA(T_{oven} - T_{wall}) + \frac{KA}{t}(T_{upstream} - T_{wall}) \qquad (67)$$

where;

$\dot{m}$	Mass flow rate (kg/s)
$T_{upstream}$	Temperature at preheating chamber outlet (K)
T_{room}	Room temperature (K)
h	Convection heat transfer coefficient (W/m^{2}K)
A	Surface area ($\pi \times d_{outside} \times l$) (m^2)
T_{kiln}	Kiln temperature (K)
T_{wall}	Preheating chamber wall temperature (K)
K	Thermal conductivity of austenitic stainless steel (W/mK)

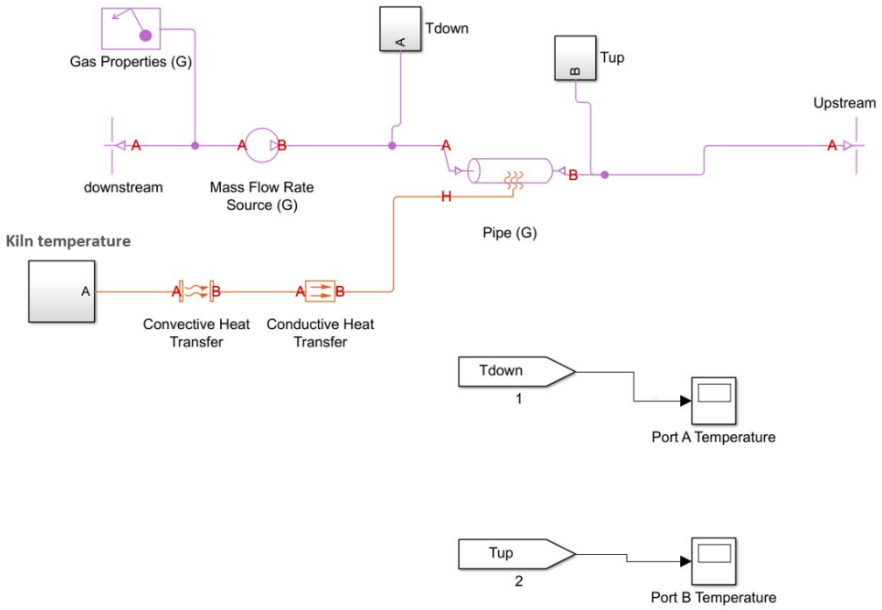

Figure 21. Matlab Simulink: Model for the preheater length.

The heat transfer from the kiln wall to the test rig occurs through convection and then heat transfer occurs from the heated air to the preheater tube wall through conduction. This was shown in Matlab Simulink (Figure 21) using convective and conductive heat transfer blocks and using the kiln temperature block. T_{down} and $T_{upstream}$ blocks were used to indicate the temperature change of both downstream and upstream respectively.

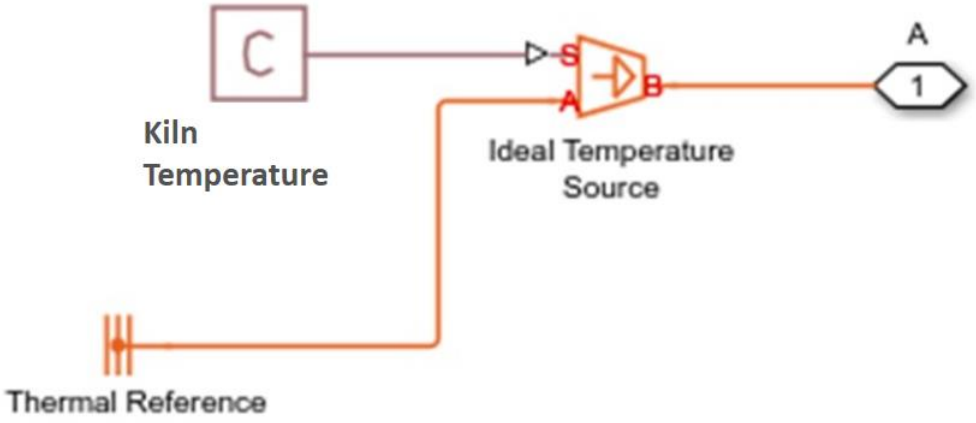

Figure 22. Matlab Simulink: Kiln temperature subsystem.

The kiln temperature subsystem represents the temperature of the oven and consists of three main blocks, kiln temperature, thermal reference and the ideal temperature source. In the subsystem, the kiln temperature is assigned to a Physical Signal (PS) constant block that generates a constant value of 1400.15 K representing the kiln temperature. The thermal reference block represents a thermal reference point that is at absolute zero temperature with respect to all other temperatures in the system. The ideal temperature source block represents an ideal source of thermal energy that is powerful enough to maintain specified temperature at its outlet regardless of the heat flow consumed by the system [73]. Here in the subsystem, connections *A* and *B* are thermal conserving ports and port *S* is a physical signal port, through which the control signal that drives the source is applied. The temperature difference across the source is directly proportional to the signal at the control port *S* and therefore the subsystem generates 1400.15 K as the final output.

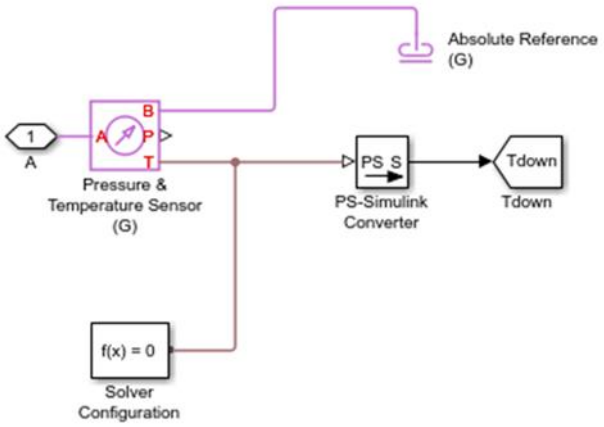

Figure 23. Matlab Simulink: Downstream temperature measurement subsystem.

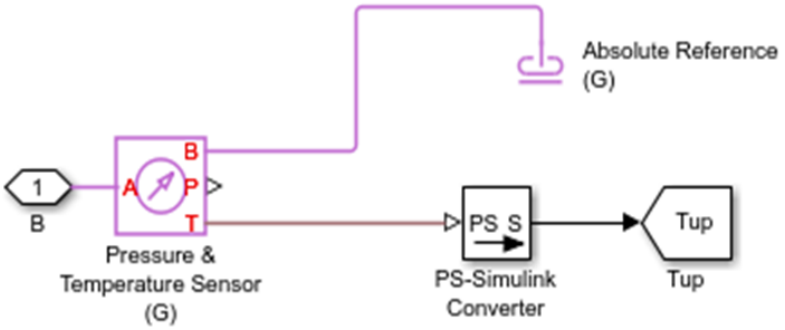

Figure 24. Matlab Simulink: Upstream temperature measurement subsystem.

The downstream and upstream measurement subsystems are to measure the temperature of the main system. This subsystem consists of four elements such as pressure and temperature sensor, PS Simulink converter, solver configuration and two "Go to" elements which are indicated as T_{down} and T_{up}. The pressure and temperature sensor block represent an ideal sensor which measure pressure and temperature in a gas network. No mass or energy flow is associated with the sensor [73]. The physical signal ports *P* and *T* report the pressure difference and the temperature difference respectively. The measurements are positive when the values at port *A* are greater than the values at port *B*. In order to measure the absolute temperature at port *A*, the port *B* connected to the absolute reference block. PS Simulink converter is used to convert the physical signal for the port *A* temperature to a Simulink output signal. The solver parameters such as tolerance is associated with the solver configuration and the value is 1×10^{-9} for current system. The "Go to" block is used to pass the result of the subsystem to outside corresponding block.

The results relating to Port *A* temperature (i.e. downstream temperature) and the Port *B* temperature (i.e. upstream temperature) are shown in Figure 25 and Figure 26 respectively.

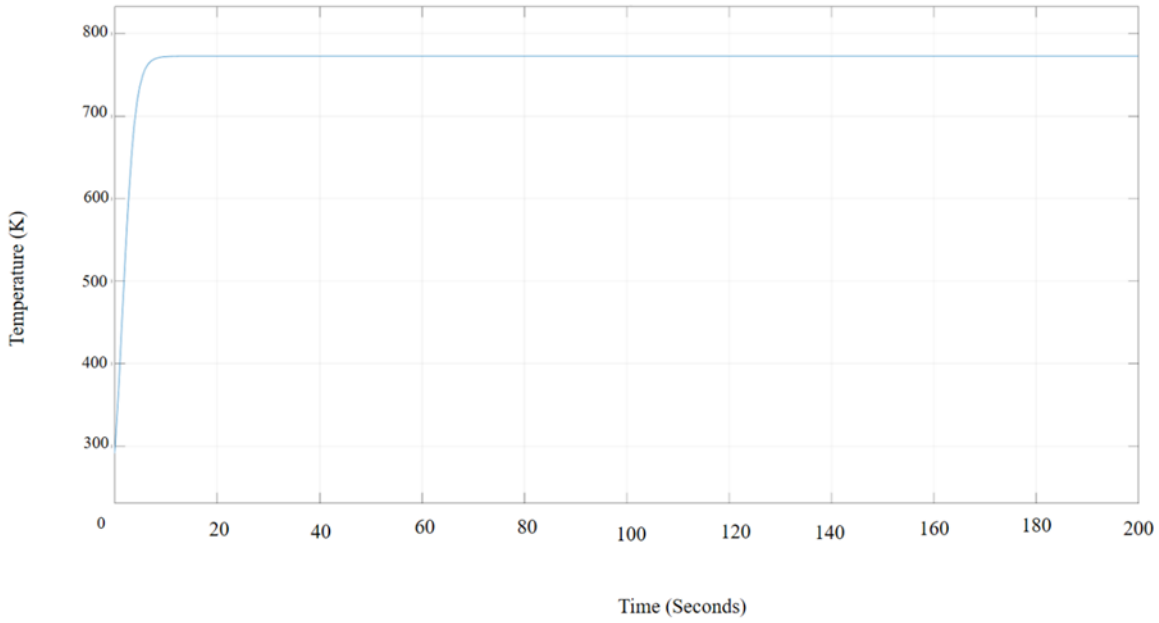

Figure 25. Matlab Simulink: Results for Port *A* (downstream temperature).

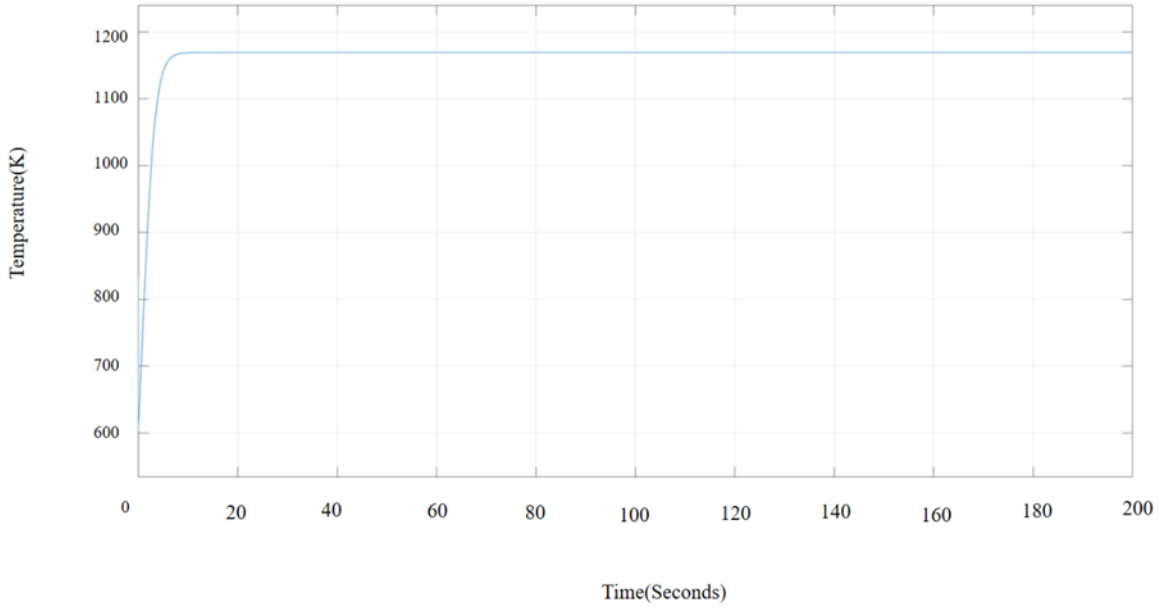

Figure 26. Matlab Simulink: Results for Port *B* (upstream temperature).

4.5.4 Assessment of potential materials for the test rig

The most demanding applications for high temperature materials are found in aircraft jet engines, industrial gas turbines and nuclear reactors. Other than those common applications, furnaces, ducting and electronic devices (such as electronics in downhole instrument in oil and

gas industry, control circuits mounted in aircraft engines , high temperature printed board circuits (PCB) and etc.) also can be identified as high temperature applications [74]. For high temperature performance, a material must have at least two essential characteristics. Firstly, since increasing temperature tends to reduce strength, the material must be strong. Secondly, since oxidation and corrosion attack also increase with the temperature, it must have resistance to its environment. Materials which can be used at high temperatures are considered in this section.

4.5.4.1 Quartz

Fused quartz, as an industrial raw material, can be used to make various refractory shapes such as crucibles, trays, shrouds and rollers for high temperature thermal processes such as steel making investment casting and glass manufacture.

Refractory shapes made from quartz glass have excellent thermal shock resistance and are chemically inert to most substances [75, 76]. Translucent fused silica tube options are normally used to replace electric elements in room heaters, industrial furnaces and other similar applications [77]. When compared to other materials, quartz is extremely hard and requires specialists for processing.

4.5.4.2 Ultra-high temperature ceramics

According to William et al [78], ultra-high temperature ceramics are an emerging class of materials that have melting points above 3000°C [79, 80]. Ultra-high temperature ceramics are binary compounds in which boron, carbon, or nitrogen combine with one of the early transition metals such as zirconium, titanium, and tantalum. Due to the strong covalent bonds with one of two those elements, these ceramic materials have high hardness, stiffness and melting points. Furthermore, these compounds also exhibit higher electrical and thermal conductivities than oxide ceramics because of their varying degrees of metallic bond character [81]. They are mostly used in furnaces, rocket motors, heat shields and structural components of aircrafts.

4.5.4.3 Nickel based super alloys

Nickel based super alloys are mostly used in boilers, boiler tubes and turbines at steam temperatures of 700 ℃ where they have been thoroughly tested [82]. These alloys have been evaluated at temperatures up to 760 ℃ and have been modified to meet the services requirements of those components [83].

4.5.4.4 Stainless steel

Stainless steel for high temperature applications can be classified by two types: martensitic and austenitic stainless steel [84]. Martensitic stainless steel is classified as a creep-resistant steel in European standards EN 10088-1 and EN 10302 [85] and due to their low chromium content, they are not primarily specified as heat resistant grades. However, they are specified when the application requires good tensile strength. Normally martensitic stainless steel can withstand 650 ℃ [86].

Austenitic stainless steels provide the best combination of high temperature corrosion resistance and high temperature mechanical strength of any alloy group. Hence, there are heat–resistant austenitic grades listed in EN 10095 and creep-resistant austenitic grades in EN 10302 [87]. Heat resistant austenitic grades are widely used in high temperature applications up to ≈1000 ℃ in dry air [88]. Typical examples include supporting elements and pipes in furnaces, annealing bells, cementation and hardening boxes and annealing pots [88].

Stainless steel for high temperature applications is designed to have a protective oxide such as chromium oxide (Cr_2O_3), aluminium oxide (Al_2O_3) and silicon dioxide (SiO_2) [89, 90].The effect of chromium oxide is particularly evident above 500℃. It forms a tight, adherent layer of chromium–rich oxide on the surface of the metal, retarding the inward diffusion of oxygen and impeding further reaction. Other elements, besides chromium also be added to stainless steel to increase oxidation resistance. Silicon and aluminium act very similarly to chromium. Stainless steel can be supplied in either wrought or cast forms. Although their chemical compositions are similar, the properties and costs of the two forms vary.

4.5.4.5 Choice of material for the test rig

Based on the above review of materials for high temperature applications, austenitic stainless steel was chosen for the high temperature test rig fabrication purpose. This is because when compared to ceramic and quartz, austenitic stainless steel is readily available, cost-effective, can easily be machined. According to the literature [91, 92], they can be used at temperatures up to 1000 ℃ and the melting point of the austenitic stainless steel is much above 1005 ℃ [93]. Whilst ceramic and quartz can also withstand high temperature and quartz could provide a transparent test rig, specialised labour is needed for machining which gives higher manufacturing costs. Nickel based alloys were not chosen due to a lower range of service temperature than stainless steel.

By considering the above factors, grade 310 austenitic stainless steel was initially selected to fabricate the test rig. However, due to the lack of availability of grade 310 in the sizes required and the cost of making hollow tube from grade 310 austenitic stainless steel bar is high, the only option was to use grade 316 austenitic stainless steel to fabricate the high temperature test rig. Since grade 316 is not designed to withstand a temperature of 1100 ℃, the maximum temperature feasible for measurements in this project was reduced to approximately 900 ℃. [94]

In the following sections, thermal analysis is carried out on grade 316 austenitic stainless steel to assess any differences in case future projects need to go to higher temperatures.

4.5.5 Thermal stress analysis of the high temperature test rig

As the upper temperature limit of grade 316 austenitic stainless steel is not known exactly but for measurements to ≈800 ℃ is the lower temperature limit used in Finite Element Analysis (FEA) to assess the thermal stability and thermal stress for components of the test rig was 900 ℃. The aim with FEA is to calculate the thermal stress von Mises over each component of the test rig and check that the maximum value is less than the yield stress and make a comparison with the ultimate tensile stress for the grade of austenitic stainless steel. von Mises stress is usually used to analyse the yield point of design under the action of complex loads. The stress value indicates the load per unit area at which material will yield or fracture. It helps designers to check whether their design will withstand a given load condition. [95, 96]

Thermal stress is simulated by coupling heat transfer and structural analyses for which the process consists of two main steps:

1. Perform heat transfer analysis to determine the temperature distribution
2. Apply the temperature results as a load in a structural analysis to determine the stress caused by the temperature load.

FEA was carried out using mechanical simulation Autodesk software with transient heat transfer analysis for grade 316 austenitic stainless steel. Since the model will be analysed using brick elements, solid mesh type was selected and the selected finite element mesh size was 6 mm [97].

It is assumed that the heat transfer occurs due to both convection and conduction inside the test rig. Based on the available kiln, it can be assumed that the temperature could rise from 800 ℃ to 900 ℃ in 540 s (9mins) which allows time-varying temperature to be assessed towards the upper temperature limit. The initial temperature of the inner and outer surfaces of the test rig are assumed to be 800 ℃. The airflow velocity (u) is the same as the experimental situation, i.e. 0.5 $\times 10^{-3}$ m/s. However, when considering the results, the grade 316 austenitic stainless steel design failed at temperatures similar and above 900 ℃ and because of that, the focused experimental temperature was reduced for 800 ℃.

The calculations which were conducted as follows for the convection heat transfer coefficient.

Prandtl number of the air at 800 ℃ (Pr): 0.70538 [98]
Kinematic viscosity of air at 800℃ (γ) : 13.17×10^{-5} m^2/s [98]
Thermal conductivity of air at 800℃ (k) = 7.0746×10^{-2} W/mK [98]
The hydraulic diameter (D_h): (For this case the internal diameter of the cylinder was considered) 100 mm

Therefore the Reynolds Number (Re) =$\frac{uD}{\gamma}$ = 3.7965

The Nusselt number (Nu) = $\frac{hD}{k}$ =$0.989Re^{0.330}Pr^{\frac{1}{3}}$ (For 0.4 < Re <4) [72]

From calculation, *Nu* =1.3673 therefore, the convection heat transfer coefficient (*h*) = 0.9673 W/m^2K

Temperature distribution and von-Mises stress distribution results for main three components of the test rig are presented in Figure 27 to Figure 32.

According to the material property data of Grade 316 austenitic stainless steel has the yield stress of 250 MPa and 565 MPa of ultimate tensile stress [93]. As shown in Figure 28, most of the parts of the specimen holder cap have the stress less than the yield stress of the material and however, the connecters exceed the yield stress of 250 MPa. In the specimen holder (see Figure 30), the stress of most of areas of the body as well as the connecting parts exceed the yield stress. Furthermore, both of those designs have a maximum stress which exceeds the ultimate tensile stress of the material. Therefore, the specimen holder cap and the specimen holder cannot be considered as safe at the temperature of 900 ℃. As shown in Figure 32 , only the preheater has the stress which is lower than the yield stress. Therefore the preheater can be considered as safe at 900 ℃.

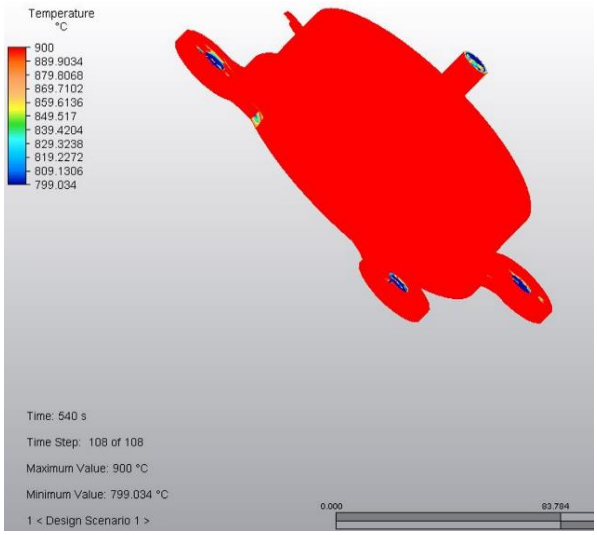

Figure 27. Temperature distribution of specimen holder cap

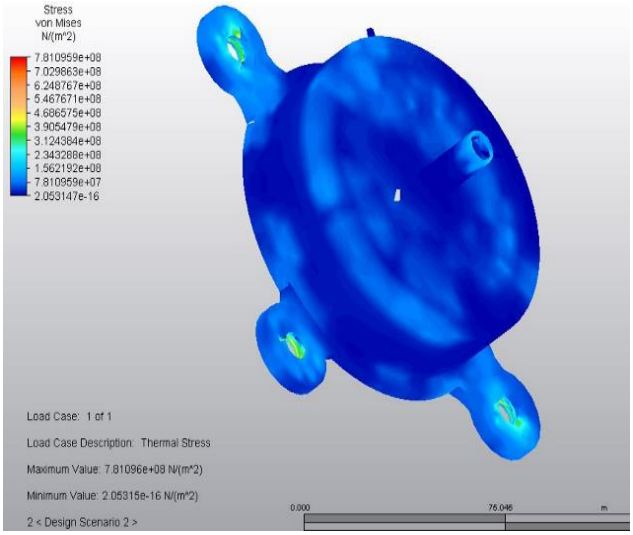

Figure 28. von-Mises stress distribution of specimen holder cap

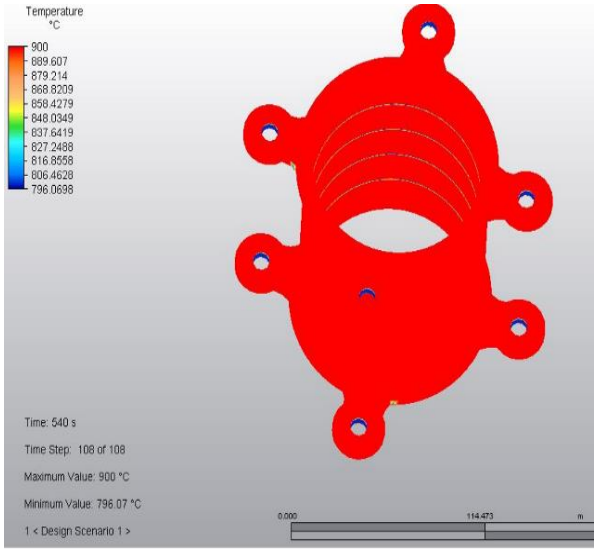

Figure 29. Temperature distribution of specimen holder

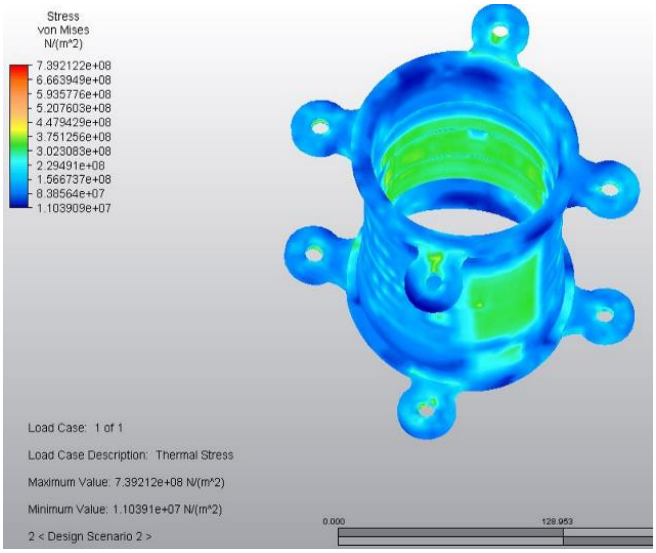

Figure 30. von-Mises stress distribution of specimen holder

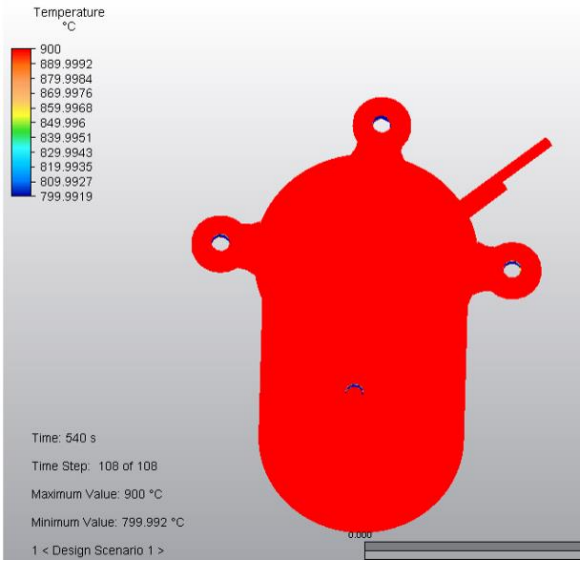

Figure 31. Temperature distribution of preheater

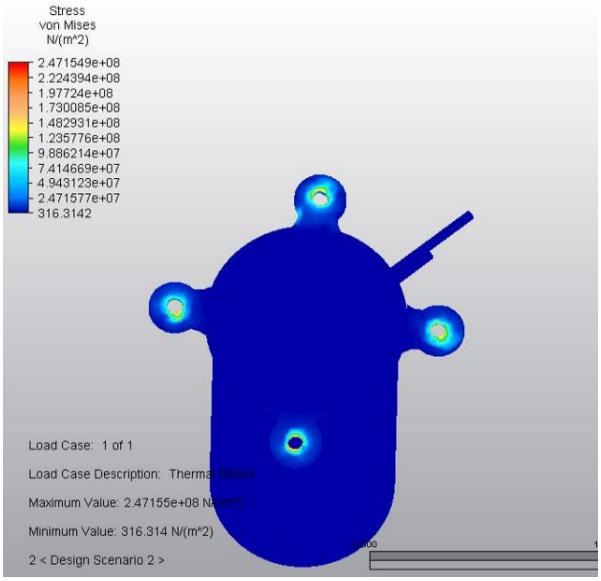

Figure 32. von-Mises stress distribution of preheater

4.5.6 Pipe connections

The airflow and differential pressure measuring instruments are situated outside the kiln and are connected via grade 316 austenitic stainless steel pipes to the test rig inside the kiln. This can be seen in Figure 33 and Figure 34. Details on the connections and the components associated with the whole system are in Appendix C and Appendix D.

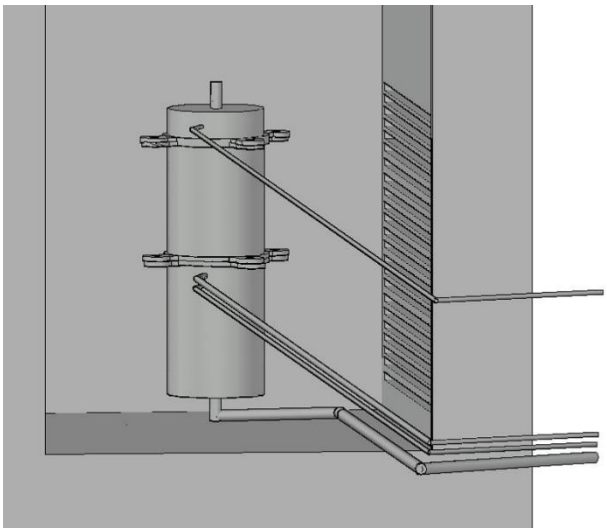

Figure 33. AutoCAD 3D model of high temperature test rig with connecting pipes.

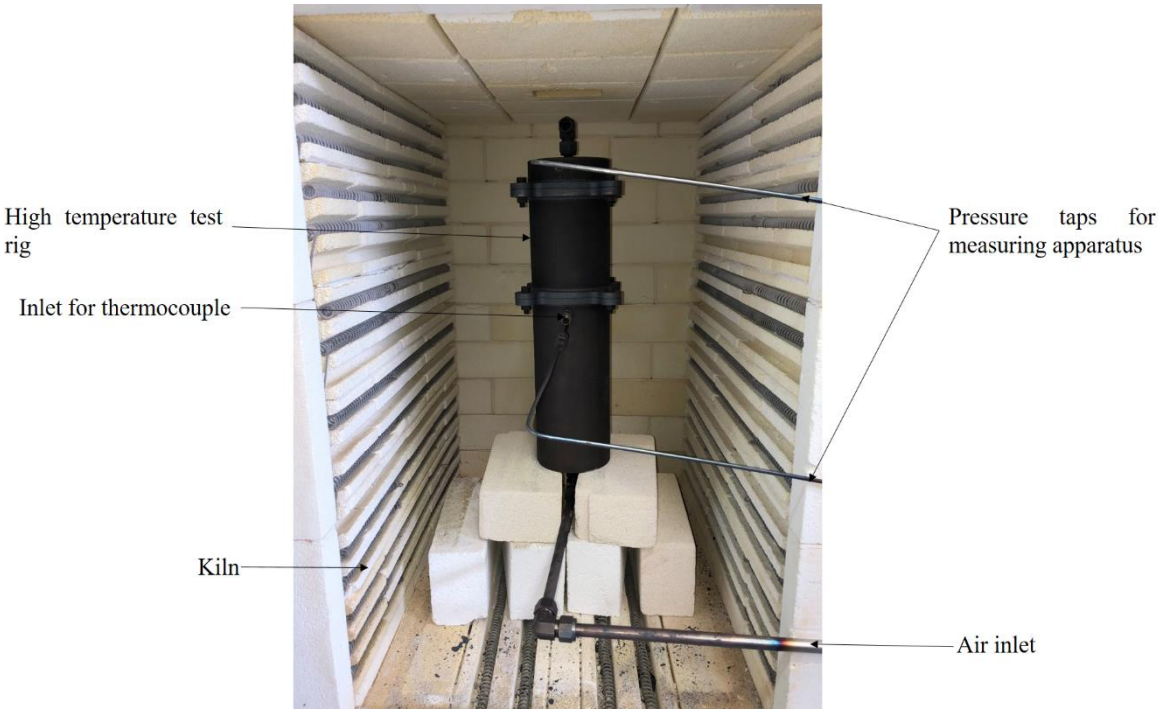

Figure 34. Photo of high temperature test rig with connecting pipes.

An assessment was needed to avoid the heat damaging the instruments because (a) the measuring instruments cannot withstand the air temperatures that are generated inside the kiln, and (b) the high temperature of the pipes inside the kiln could potentially be conducted outside the kiln and melt the connections to the measuring instruments.

4.5.7 Simulink modelling to determine the length of pipe needed to ensure sufficient cooling

The measuring instrument used to measure the differential airflow and flow rate is intended for air temperatures below 34 ℃; however, the exhaust air is at a high temperature hence it needs to be cooled before measurements can take place. As the kiln is rated to 1100 ℃, this is chosen as the upper temperature for this analysis.

A heat exchanger is designed for the exhaust air tubes consisting of a wrapped copper pipe containing cold water and austenitic stainless steel pipe. The temperature of the cold water from the chiller is 5 ℃.

Simulink modelling was used to assess the length of austenitic stainless steel tube that would be needed to ensure that the air inside the pipe was cooled before it reached the measuring instrument.

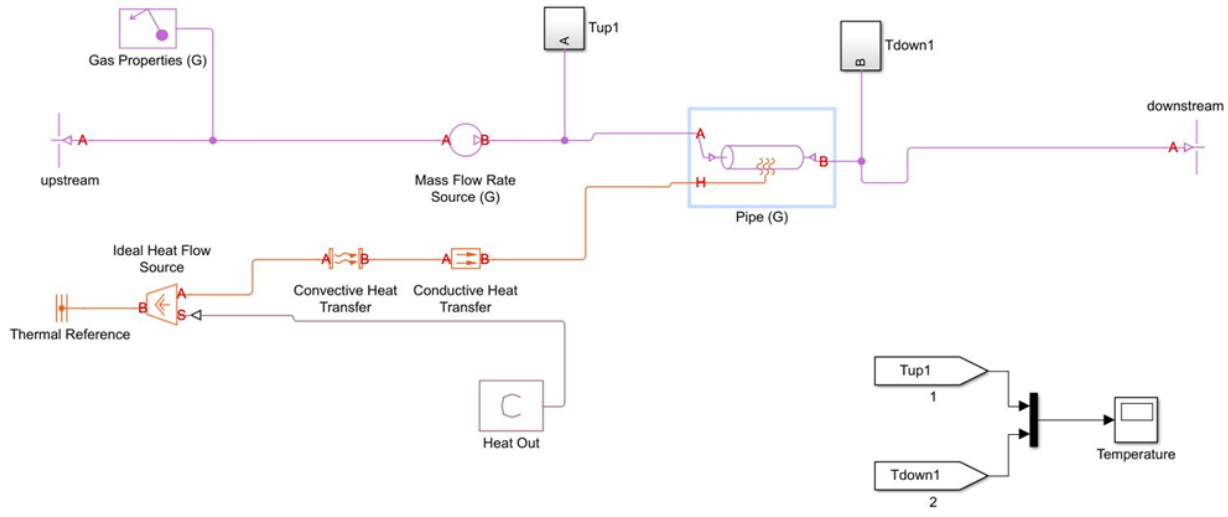

Figure 35. Matlab Simulink: System to assess pipe cooling.

As shown in Figure 35, the heat outflow from pipe wall to the environment is represented using conductive and convective heat transfer blocks. They represent heat transfer from the pipe wall to the copper wrapping through conductivity and from copper wrapping to the cold water from convection. T_{up1} and T_{down1} represent the upstream and downstream temperatures respectively.

Properties of chilled water at 5 °C are [99]**:**

Density (ρ) : 1000 kg/m^3 Prandtl number (Pr): 11.2

Thermal conductivity (k): 0.571 W/m^{2}C

Kinematic viscosity (γ) = dynamic viscosity/density = $\frac{1.319\times10^{-3}}{1000}$: 1.319x10^{-6} m^2/s

Properties of air at 1100 °C are [98]**:**

Density (ρ) : 0.26156 kg/m^3 Prandtl number (Pr): 0.72168

Thermal conductivity (k): 0.082142 W/m^{2}C Kinematic viscosity (γ) : 1.920x10^{-4}

Heat transfer coefficient for 1100 ºC (h_h):

Hydraulic diameter for the pipe (D_h): 6.25 x10^{-3} m

Mean velocity of air (V_m) : 5x 10 $^{-4}$ m/s

Reynolds number for air (Re) = $\frac{V_m D_h}{\gamma}$ = $\frac{5x10^{-4}x6.25x10^{-3}}{1.920x10^{-4}}$: 0.01627604167

As the Reynolds number is significantly lower than 4000, the flow can be assumed to be laminar.

Since 100<Re, Nusselt number (Nu) from Nusselt number data table [72, 100], with respect to the value of D_i/D_o (6.25/7.35) = 0.85

$$Nu=6.62 = \frac{h_h D_h}{k}$$

Therefore, h_h = $\frac{6.62\times0.082142}{6.25x10^{-3}}$: 87.0048064 W/m^{2}C

Heat transfer coefficient for 5 ºC chilled water (*hc*):

Chiller outlet diameter =12.7 mm = 12.7×10^{-3} m (According to manufacturer's data)

Chilled water outlet flow rate (m^3/s) = 0.00025 m^3/min= 4.1667×10^{-6} m^3/s

Therefore the mean velocity (V_m) = $\frac{4.1667x10^{-6}}{0.0127^2 x 0.25 x 3.14}$= 0.0329$ms^{-1}$

Reynolds number (*Re*) = $\frac{0.0329x0.0127}{1.319x10^{-6}}$ = 316.8648 (flow remains laminar)

Since 100< Reynolds number (*Re*) <2000 [72];

$Nu=\frac{h_c D_h}{k}$ =0.664 $Re^{0.5}Pr^{1/3}$= 0.023x $(316.8648)^{0.5}$x $(11.2)^{1/3}$ =26.445

Therefore, h_c = 1188.98 $W/m^{2o}C$

The overall heat transfer coefficient (*U*) = $\frac{1}{\frac{1}{h_h}+\frac{1}{h_c}} = \frac{1}{\frac{1}{87.0048}+\frac{1}{1188.98}}$= 81.072 $W/m^{2o}C$

$$Q = U\ A\ \Delta T \tag{68}$$

According to the manufacturer's data, the capacity of the chiller is 2500 W,

By assuming the efficiency is 50 %,

$2500 \times 0.5 = 81.072 \times \pi dl$x (1100 - 34)

$=81.072 \times \pi \times 6.25 \times 10^{-3} \times l \times (1100 - 34)$

L= 0.7366 m = 73.7cm

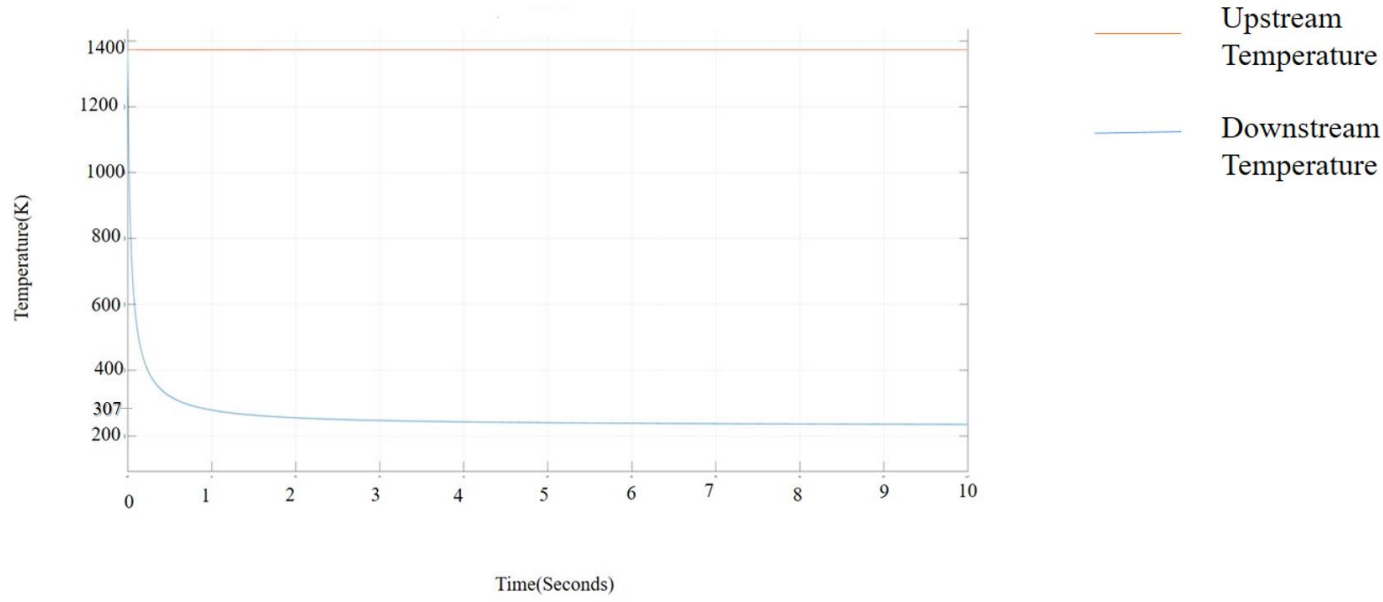

Figure 36. Matlab Simulink: Results for the temperature of pipe.

From Figure 36, it is seen that the upstream temperature is at a constant temperature of 1400 K (1127℃) whilst the downstream temperature reduces from 1400 K (1127 ℃) to 307 K (34 ℃) due to conductive and convective heat transfer.

4.5.7.1 Experiments to assess the effect of heating and cooling the pipe connections

Experiments were carried out to assess heat transfer along grade 316 austenitic stainless steel tubes and the cooling provided by the proposed heat exchanger. These experiments were used to check the efficiency of the heat exchanger to cool the exhaust tube before reaching the differential pressure and flow measuring apparatus because the operating range of this apparatus is limited to 34 ℃. The kiln temperature for the experiment was 900 ℃ with the dwell time set at 4 hours. The applied ramp rate for the kiln was 400 ℃ and within approximately 4 hours the kiln achieved the target temperature of 896 ℃ within 4 ℃.

The measurements used two 90 cm long, grade 316 austenitic stainless steel hollow tubes where 30 cm of the tube was inside the kiln and 60 cm was outside the kiln. The smaller diameter tube for the differential pressure tap had an internal diameter of 3.85 mm and an external diameter of 6.43 mm. The larger diameter tube for the air inlet had an internal diameter of 10.37 mm and an external diameter of 12.79 mm.

The tubes were inserted into the kiln (through a hole that was a slightly larger diameter than the largest pipe diameter) located in the kiln front door as indicated in Figure 37.

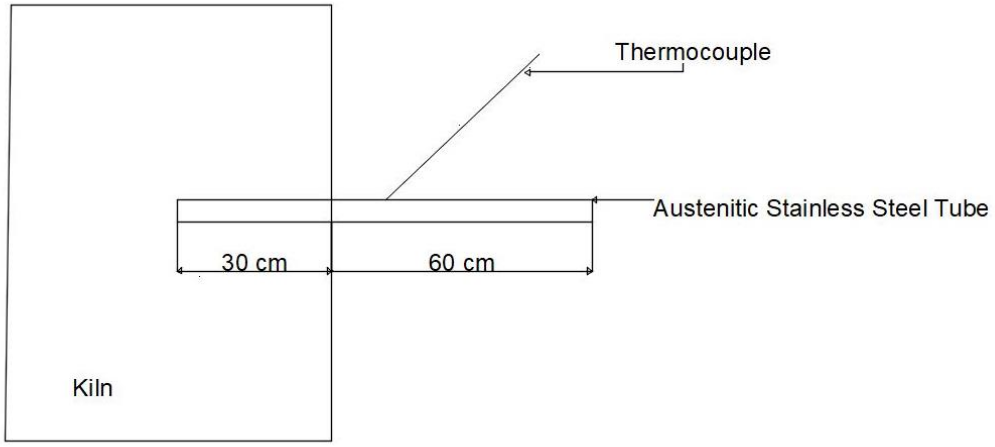

Figure 37. Experimental set-up used to assess cooling of the connecting pipes.

The temperature in the kiln was 900 ^{o}C and the room temperature was 12 ^{o}C. Measurements were taken 30 minutes after inserting the tube into the kiln. The temperature along the tube was measured at 20 cm intervals using a digital thermometer TENMA 72-10390A and a K-type thermocouple. The temperature results for the two different diameter pipes are given in Table 4. The larger diameter pipe has a lower temperature than the small diameter pipe outside the kiln at a distance of 20 cm. This can be caused by the larger surface area that is exposed to the cool air outside the kiln so the rate of heat transfer from the pipe surface to the outside is higher than the small pipe, as described by the following equation

$$\dot{Q} = (UA\Delta T)/t \tag{69}$$

where $\dot{Q}$ is the heat transfer rate from the pipe surface to the outside, U is the overall heat transfer coefficient (W/m^2.K), A is the surface area, t is time and ΔT is the temperature difference ($\Delta T = T_{surface} - T_{Environment}$). As U, $T_{Environment}$, and t are constant, the larger surface area of the larger diameter pipe gives a higher heat transfer rate; hence the larger diameter pipe is cooler than the small diameter pipe at a distance of 20 cm from the kiln. However, after this distance the temperature of both pipes is similar to room temperature.

Table 4. Measured change in temperature along the length of pipe that was outside the kiln when the inside of the kiln was at 900 °C.

	Pipe diameter (mm) at room temperature		Temperature (^{o}C)		
	Internal	External	Outside the kiln at a distance of 20 cm from the kiln door	Outside the kiln at a distance of 40 cm from the kiln door	Outside the kiln at a distance of 60 cm from the kiln door
Smaller diameter pipe	3.85	6.43	37.1	15.1	13.5
Larger diameter pipe	10.37	12.79	15.0	14.8	14.2

The heat exchanger used in the experiment consisted of 5 mm diameter copper tubing wrapped around the austenitic stainless steel pipe that was surrounded by foam. The chiller supplied cool water at 4 ℃. One end of the austenitic stainless steel tube was inserted into the kiln. The temperature in the kiln was 900 ^{o}C and the room temperature was 12 ^{o}C and the measurements were taken after 30 minutes.

Surface temperature measurements were taken on the steel pipe and the foam wrapping and air temperature measurements were taken at the exhaust of the pipe. The arrangement is shown in Figure 38 and the results are given in Table 5.

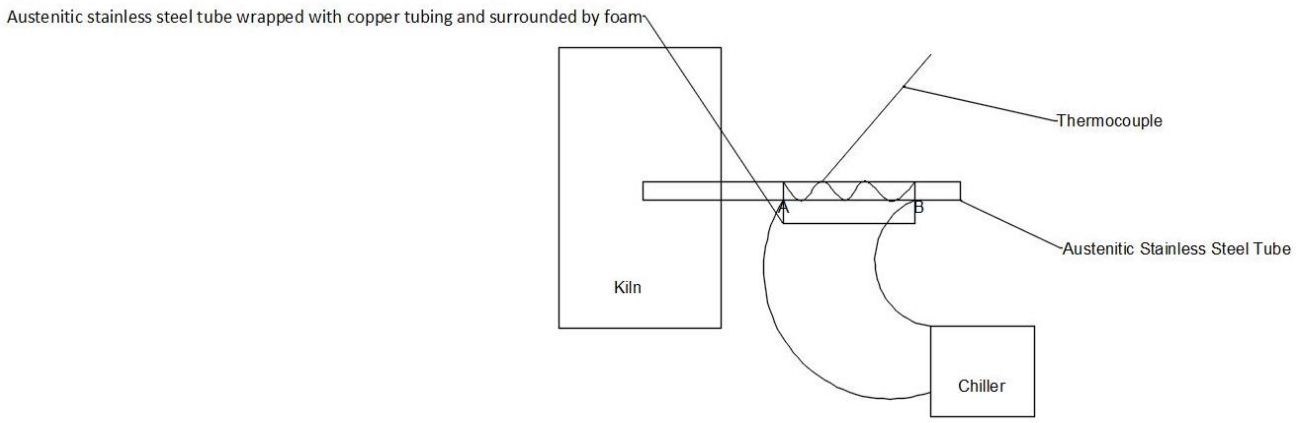

Figure 38. Experimental cooler arrangement indicating temperature measurement points A and B.

Table 5. Temperature changes of pipework with cooler arrangement.

Inside pipe diameter at room temperature (mm)	Outside pipe diameter at room temperature (mm)	Surface temperature at Point A – near to kiln door (°C)	Surface temperature at Point B – at air outlet (°C)	Surface temperature at Point C – on foam (°C)	Air temperature inside the tube at Point D – underneath the copper cooler (°C)
3.85	6.43	37.1	14.6	15.3	11.1
10.37	12.79	32.8	14.7	14.1	10.9

At the exhaust point which would connect to the measuring instrument, the air temperature with and without the cooler is below 34 °C; hence there was no need to use a heat exchanger.

4.5.7.2 Expansion of pipes

To assess the expansion of taps and their external connecting pipes based on diameters (d) some manual calculations were carried out. These used equation (70) and the results are given in Table 6 and Table 7. Here, the room temperature is assumed to be 20 °C and it is assumed that the kiln temperature is 900 °C. The thermal expansion coefficient (α) for austenitic stainless steel is 15.6 x10^{-6} /°C [93].

$$\Delta d = d\alpha\Delta T \tag{70}$$

where;

ΔT: Temperature difference

Δd: Diameter change

Table 6. Measured expansion for connectors of the test rig.

Test rig tap type				Expansion (mm) ($d\alpha\Delta T$)				Expansion (%)			
Air inflow		Differential pressure		Air inflow		Differential pressure		Air inflow		Differential pressure	
Inside diameter (mm)	Outside diameter (mm)	Inside diameter (mm)	Outside diameter (mm)	Inside diameter (mm)	Outside diameter (mm)	Inside diameter (mm)	Outside diameter (mm)	Inside diameter (%)	Outside diameter (%)	Inside diameter (%)	Outside diameter (%)
8.00	10.25	2.95	3.72	0.110	0.141	0.040	0.051	1.38	1.38	1.38	1.38

Table 7. Measured expansion of external connecting pipes.

External pipe type				Expansion (mm) ($d\alpha\Delta T$)				Expansion (%)			
Air inflow		Differential pressure		Air inflow		Differential pressure		Air inflow		Differential pressure	
Inside diameter (mm)	Outside diameter (mm)	Inside diameter (mm)	Outside diameter (mm)	Inside diameter (mm)	Outside diameter (mm)	Inside diameter (mm)	Outside diameter (mm)	Inside diameter (%)	Outside diameter (%)	Inside diameter (%)	Outside diameter (%)
10.37	12.79	3.85	6.43	0.143	0.176	0.053	0.088	1.38	1.38	1.38	1.38

The experiments were performed for test rig connectors and external pipes for the expansion and the results for the change in pipe diameters are given in Table 8 and Table 9. These results indicate that the pipes shrink after heating to 900℃ and cooling down to room temperature. As the test rig will be used on multiple heating cycles, the shrinkage is not expected to cause air tightness problems over time.

Table 8. Measured expansion or shrinkage of test rig connectors.

Test rig tap type				After heating to 900 ℃ and having cooled down to room temperature				Percentage of expansion or shrinkage (%)			
Air inflow		Differential Pressure		Air inflow		Differential Pressure		Air inflow		Differential Pressure	
Inside diameter (mm)	Outside diameter (mm)	Inside diameter (mm)	Outside diameter (mm)	Inside diameter (mm)	Outside diameter (mm)	Inside diameter (mm)	Outside diameter (mm)	Inside diameter (mm)	Outside diameter (mm)	Inside diameter	Outside diameter
8.00	10.25	2.95	3.72	8.08	10.36	2.36	3.53	1.05	1.12	-0.20	-0.05

Table 9. Measured pipe diameter change for external connecting tubes after heating to 900 °C and cooling down to room temperature (measurements carried out after the tube had cooled down to room temperature).

Inside pipe diameter at room temperature (mm)	Outside pipe diameter at room temperature (mm)	Pipe end which was inside the kiln		Pipe end which remained outside the kiln		Pipe end which was inside the kiln		Pipe end which remained outside the kiln	
		Inside diameter (mm)	Outside diameter (mm)	Inside diameter (mm)	Outside diameter (mm)	Shrinkage of inside diameter (%)	Shrinkage of outside diameter (%)	Shrinkage of inside diameter (%)	Shrinkage of outside diameter (%)
3.85	6.43	3.83	6.35	3.79	6.34	0.52	1.24	1.56	1.40
10.37	12.79	9.84	12.78	10.27	12.69	5.11	0.078	0.96	0.78

In order to make sure there is no issue with the airtightness, room temperature airflow resistivity of samples were measured for two randomly selected material IDs and the results before heating up the test rig without external connecting pipes and after heating up the test rig with external connecting pipes are given in Table 10.

Since the percentage difference in the majority of airflow resistivity values between both scenarios is less than 10% it is concluded that there is no significant issue associated with the airtightness of the assembly.

Table 10. Airflow resistivity results of material before heating the test rig without pipes and after heat up and cool down the test rig with connected pipes.

Material ID No	Before heating the test rig without pipes		After heating the test rig with pipes up to 800℃ and cooling down to room temperature		Percentage difference of airflow resistivity values without pipes and with pipes (%)
	Thickness (mm)	Airflow Resistivity ($Pa.s/m^2$)	Thickness (mm)	Airflow Resistivity ($Pa.s/m^2$)	
0063	53	44,646	48	45,954	-2.93
	53.4	43,749	50	48,126	-10.00
	50	43,929	50	41,932	4.55
	51.3	43,780	50	48,527	-10.84
	50	44,495	46	44,901	-0.91
	48	42,015	47	43,091	-2.56
	50.3	43,853	48	41,292	5.84
	52	44,159	50	40,105	9.18
	50	44,937	49	42,970	4.38
	50.6	39,630	50	44,116	-11.32
0064	40	36,630	48	34,527	5.74
	48	34,528	50	36,095	-4.54
	46	36,029	50	36,897	-2.41
	47	36,265	45	36,540	-0.76
	40	36,596	48	33,696	7.92
	39	36,506	50	37,140	-1.74
	38	36,411	47	35,838	1.57
	43	35,292	46	37,606	-6.56
	50	36,897	54	35,278	4.39
	40	36,630	49	36,422	0.57

4.6 Choice of preheater material

Following the approach of Christie [34], a preheater was used to try and ensure that the temperature of the air inside the test rig is nominally identical to the kiln temperature. To achieve this it is necessary to use packing material inside the preheater. After performing several experiments with different packing material, Superwool plus tank car blanket (64 kg/m^3) was selected as the preheater material. This material has a high melting point, is mechanically stable with very low shrinkage at high temperatures and is mechanically needled for added tensile strength and surface integrity. Its thermal conductivity is 0.27 W/mK at 816 ℃. One issue occurs because the material is thermally insulating. Initial experiments showed that if the preheater was filled with this material then the air temperature at the top of the preheater (just before it enters the test specimen holder) was only 536 ℃. Therefore, only a 50 mm layer was used as indicated in Figure 39.

According to the manufacturer, the thermal conductivity values of the packing material are as indicated in Table 11. According to the EN 12939:2000 [101] since, all of those values are less than 0.3 W/mK, the material can be considered as a thermally insulating material.

Table 11. Thermal conductivity of the packing material along with the temperature

Temperature (℃)	Thermal conductivity (W/mK)
260	0.07
538	0.14
816	0.27

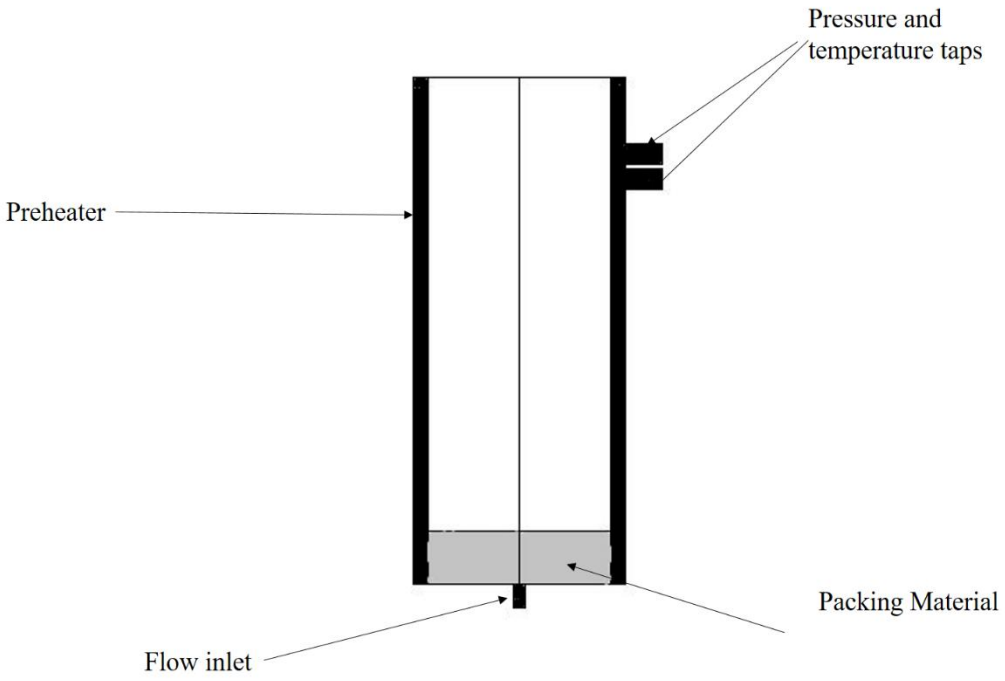

Figure 39. Packing material inside preheater.

4.6.1.1 Sample thickness measurement

The material thickness varied between 40 and 60 mm and was measured before placing it inside the test rig using a standard pin and disc technique according to ISO 10635 [102]. After the sample was positioned inside the test chamber it was possible to check that the compression of the sample using the five grooves that were marked as indicators inside the test rig (25 mm spacing).

4.7 Measurement of differential pressure

The Furness Control FCS 523 measurement instrument that was used to measure the differential airflow and flow rate is intended for air temperatures below 34 ℃. However, for the high temperature rig it is necessary to measure the differential pressure for air in the kiln that varies between room temperature and 800 ℃. The air from the two tapping points for differential pressure on the test rig is connected to pipes that lead to the measurement instrument. These pipes lose heat along their length so that air temperatures are below 34 ℃ when the air reaches the instrument.

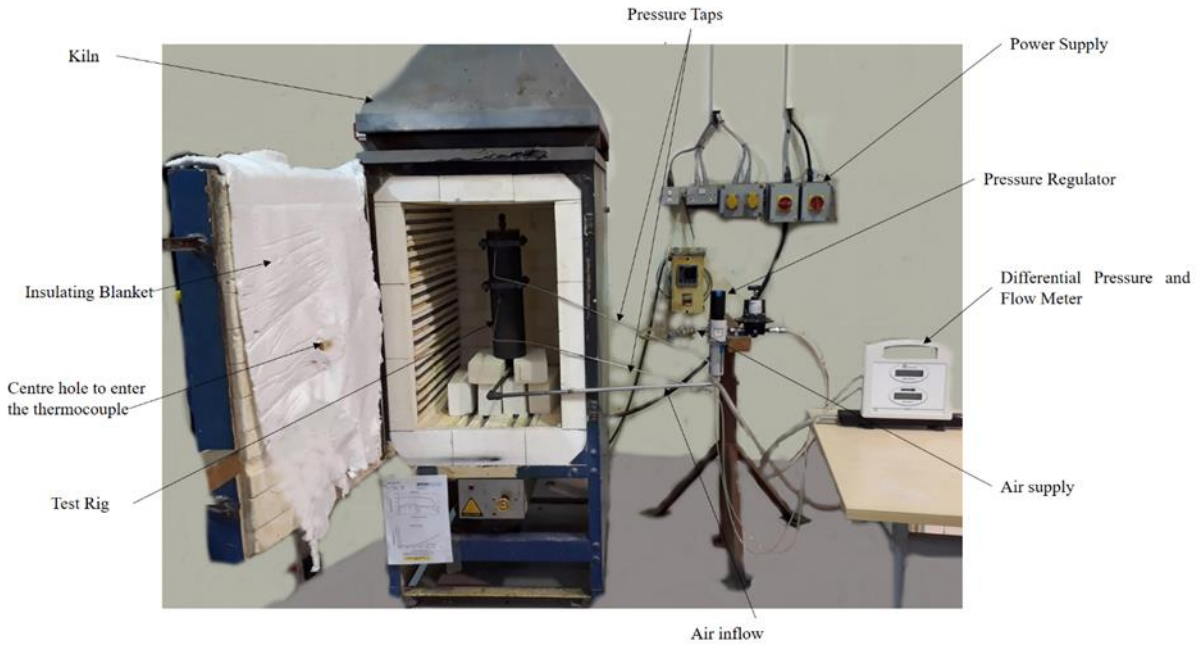

Figure 40. High temperature experimental assembly.

4.7.1 Simulink modelling of differential pressure measurements in the high temperature test rig

To assess the potential change in the differential pressure between measurements at 18 ℃ and 800 ℃, simulations were carried out using Matlab Simulink – see model in Figure 41.

The local restriction block in Simulink was used to represent a porous material by changing its parameters to recreate experimental data for 100 mm Rockwool (100 kg/m^3) from Hopkins [6] at room temperature (assumed to be 18 ℃) which gave a differential pressure of 2.3 Pa .

The laminar flow velocity for the model is 5×10^{-4} m/s (i.e. the same as the measurement). The Simulink model requires the mass flow rate that is calculated from the product of the cross-sectional area, flow velocity and air density. At 18 ℃, the mass flow rate is 4.728×10^{-6} kg/s whereas at 800 ℃ (where air density is lower) it is 1.01×10^{-6} kg/s.

The differential pressure result from the simulation is 0.62 Pa at 800 ℃, which is significantly lower than the room temperature value of 2.3 Pa. For this reason, the next section investigates the correction that is needed to ensure that the differential pressure measured at room temperature corresponds to the differential pressure that exists at high temperature.

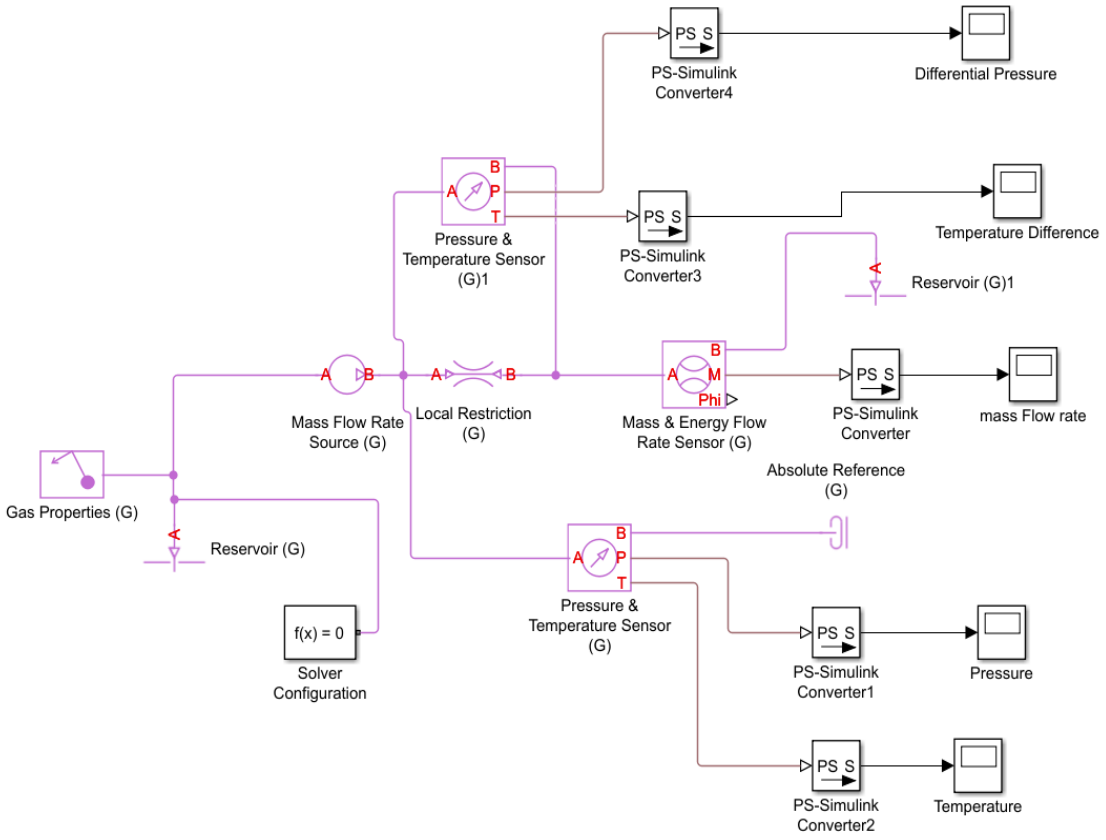

Figure 41. Simulation of the high temperature rig measurement using a local restriction to simulate a porous material.

4.7.2 Manual calculation for differential pressure variation according to the temperatures

Calculations and simulations related to the differential pressure were performed according to temperature variation using ideal gas law [103]. The relationship linking differential pressure at room temperature and high temperature is discussed here.

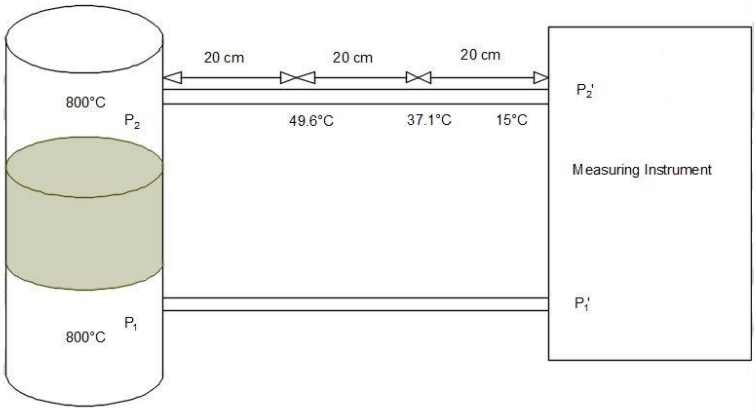

Figure 42. Arrangement of high temperature test rig and the measuring instrument.

Calculations were carried out using the ideal gas equation (71) as follows.

The ideal gas equation is given by

$$PV = n\,RT \tag{71}$$

where,

P : Pressure (Pa)

V : Volume (m^3)

n : Number of moles (mol)

R : Universal gas constant (8.314 J/mol/K)

T : Absolute temperature (K)

Number of moles, $n = \frac{m}{M}$

where:

m : Mass of air (kg)

M : Molecular mass of air (28.6×10^{-3} kg/mol)

Applying the ideal gas equation to the preheating chamber to calculate the pressures P_1 and P_2 which is given in the Figure 41.

$$P_1(\pi \times (100 \times 10^{-3})^2 \times 0.25 \times 150 \times 10^{-3}) = \frac{0.5\times10^{-3}\times(\pi\times(100\times10^{-3})^2\times0.25\times0.3289\times8.314\times1073}{28.6\times10^{-3}}$$

$$P_1 = \quad 341.96 \text{ Pa}$$

Using the cross-sectional area with the porosity which is calculated from the previously conducted Matlab Simulink program, and assuming the quantity of moles are equal in both situations gives

$$P_2(7.80152 \times 10^{-3} \times 150 \times 10^{-3}) = \frac{0.5 \times 10^{-3} \times \pi \times (97 \times 10^{-3})^2 \times 0.25 \times 0.3289 \times 8.314 \times 1073}{28.6 \times 10^{-3}}$$

$$P_2 = 344.26 \text{ Pa}$$

Hence the differential pressure is 2.30 Pa (344.26 – 341.96 Pa).

By considering the long pipe, the gas volume along the pipe is constant and only the temperature and the pressure vary along the tube. Because of that, from the ideal gas equation, pressure is proportional to temperature; hence it is possible to relate the pressure at high and low temperatures using

$$\frac{P_1}{T_1} = \frac{P_1'}{T_1'}$$

Therefore,

$$P_1' = \frac{P_1 T_1'}{T_1}$$

$$= \frac{341.96\times291}{1073}$$

$$= 92.74 \text{ Pa}$$

$$\frac{P_2}{T_2} = \frac{P_2'}{T_1'}$$

$$P_2' = \frac{P_2 T_1'}{T_2}$$

$$= \frac{344.27 \times 291}{1073}$$

=93.36 Pa

Therefore, the differential pressure is only 0.62 Pa (93.36 – 92.74 Pa) at 291 K (18 ℃) Since the manual calculation results are same as the simulation results which is indicated in above, it can be concluded that the differential pressure varies with temperature

4.8 Summary

The design of room temperature test rig and high temperature test rig has been described along with the measuring apparatus for airflow and differential pressure, and other supporting elements which were associated with the airflow supply and the kiln. Simulations were carried out in order to determine the length of the preheater of the high temperature test rig by considering the heat transfer between the test rig and the kiln.

The materials selected for the fabrication of high temperature test rig are discussed and assessed. Due to the lack of availability of Grade 310 austenitic stainless steel hollow tubes, Grade 316 austenitic stainless steel was used for the fabrication. Since it was found that the thermal stability of high temperature test rig is below 900℃, the high temperature experimental temperature was reduced to 800 ℃. Calculations were carried out to assess the effect of temperature on the differential pressure and these calculations were checked using the simulation results.

Chapter 5. RESULTS AND ANALYSIS

5.1 Room temperature measurements

5.1.1 Comparison of ISO 9053-1 and ASTM C522 results

Airflow resistivity measured using the ISO 9053-1 standard is compared with measurements according to ASTM C522 from another laboratory that were provided by the funder. The results for the sixteen different material ID numbers are shown in Table 12. Average values of airflow resistivity are shown from 10 samples for ISO 9053-1 and 5 samples for ASTM C522 measurements.

For the majority of materials there is <10% difference between the two sets of measurements. The agreement between the average values indicates that the samples had a similar fitting in the different test rigs. The difference is attributed to the following factors: different samples (although they were cut from the same production batch), different measurement standards and different operators inserting the samples in the test chamber. However, a statistical independent samples test in Table 13 shows that the results of both methods have equal variance at the 95% confidence interval of the difference (since p>0.05). It is concluded that the ISO 9053-1 and ASTM C522 measurements can be considered to be similar.

Table 12. Comparison between room temperature airflow resistivity measurements using ISO 9053-1 and ASTM C522 for different AES materials.

Material ID No.	Airflow resistivity according to ISO 9053-1 (Pa.s/m^2)	Airflow resistivity according to ASTM C522 (Pa.s/m^2)	Percentage difference (%)
0048	8,981	7,338	22.4
0050	82,366	78,742	8.7
0051	54,249	48,527	11.8
0052	42,765	42,805	0.1
0053	36,368	36,841	1.3
0054	28,373	26,899	5.5
0055	18,714	19,355	3.3

0056	14,397	14,749	2.4
0057	90,692	97,378	6.9
0058	102,016	105,496	3.3
0059	82,664	88,087	6.2
0060	50,211	54,493	7.9
0061	48,291	46,065	4.8
0062	33,728	36,677	8.0
0063	44,366	44,150	0.5
0064	36,479	37,345	2.3

Table 13. Statistical test results on the comparison of ISO 9053-1(10 samples) and ASTM C522 (5 samples).

Independent Samples Test										
		Levene's Test for Equality of Variances		t-test for Equality of Means						
		F	Sig.	t	df	Sig. (2-tailed)	Mean Difference	Std. Error Difference	95% Confidence Interval of the Difference	
									Lower	Upper
Airflow resistivity ($Pa.s/m^2$)	Equal variances assumed	.022	.884	-0.064	30	.950	-642.938	10068.14	-21204.83	19918.96
	Equal variances not assumed			-0.064	29.929	.950	-642.938	10068.14	-21206.88	19921.01

5.1.2 Assessing the effect of air leaks in the pipes

To assess the effect of a leak in the air supply and the differential pressure pipes with the ISO test rig, two materials were chosen: a sample of material ID No.0055 (64 kg/m^3) which had a low airflow resistivity and a 20 mm thick porous aluminium disk which had a high airflow resistivity.

The experiment was used to assess what would happen if there was a leak in the air supply and when there are leaks in both the air supply and the differential pressure pipe which is connected to the test rig (i.e. the pressure tap underneath the sample on the ISO test rig). These leaks were artificially created by drilling a 2 mm diameter hole in the plastic pipe close to the taps on the ISO 9053 test rig.

The airflow resistivity results for one (randomly selected) sample of material ID No.0055 (64 kg/m^3) is given in (a) Table 14 when there are no leaks, (b) Table 15 when there is a 2 mm diameter hole in the air supply and (c) Table 16 when there is a 2 mm diameter hole in the air supply and the differential pressure pipe. The results indicate that there is a negligible effect when there is a leak in the supply because the flow rate is always manually adjusted to give the required flow velocity. However, the leak in the differential pressure pipe causes a drop in the differential pressure that gives a 0.42% error in the airflow resistivity.

Table 14. Airflow resistivity results without leaks – sample of material ID No.0055 (64kg/m^3)

Thickness (mm)	Flow velocity (l/min)	Differential pressure (Pa)	Airflow resistivity (Pa.s/m^2)
43	0.236	0.37	17,181

Table 15. Airflow resistivity results with a 2 mm diameter hole in the air supply – sample of material ID No.0055 (64 kg/m^3). Percentage error is based on the value in Table 14.

Thickness (mm)	Flow velocity (l/min)	Differential pressure (Pa)	Airflow resistivity (Pa.s/m^2)	Percentage error (%)
43	0.236	0.37	17,181	0.00

Table 16. Airflow resistivity results with a 2 mm diameter hole in the air supply and the differential pressure pipe – sample of material ID No.0055 (64 kg/m^3). Percentage error is based on the value in Table 14.

Thickness (mm)	Flow velocity (l/min)	Differential Pressure (Pa)	Airflow resistivity (Pa.s/m^2)	Percentage error (%)
43	0.236	0.35	17,254	0.42

The airflow resistivity results for the 20 mm porous aluminium disk are given in (a) Table 17 when there are no leaks, (b) Table 18 when there is a 2 mm diameter hole in the air supply and (c) Table 19 when there is a 2 mm diameter hole in the air supply and the differential pressure pipe. As with the low airflow resistivity sample, the results confirm that a hole in the air supply has negligible effect but the hole in the differential pressure pipe gives rise to a higher error in the airflow resistivity (2.7%) with the high airflow resistivity sample. However, considering the similar differences between ISO 9053-1 [2] and ASTM C522 [7] this error would not be problematic; hence the test rig design is resistant to errors from air leaks.

The results from the 20 mm porous aluminium disk are useful in trying to assess the error that might occur if there were leaks in the high temperature test rig because when measurements are taken at high temperatures, it has been shown in section 5.2.2 that the differential pressure is much lower at high temperatures. The value of differential pressure of 1.08 Pa in Table 19 is similar to the lower values that are expected for the fibrous ceramic materials at high temperatures. Hence, if leaks were to occur due to thermal expansion in the test rig and/or pipes the resulting error in the airflow resistivity could be considered negligible.

Table 17. Airflow resistivity results without leaks – 20 mm porous aluminium

Differential Pressure (Pa)	Flow velocity (l/min)	Airflow resistivity ($Pa.s/m^2$)
1.11	0.235	111,292

Table 18. Airflow resistivity results with a 2 mm diameter hole in the air supply - 20mm porous aluminium. Percentage error is based on the value in Table 17.

Differential pressure (Pa)	Flow velocity (l/min)	Airflow resistivity ($Pa.s/m^2$)	Percentage error (%)
1.11	0.235	111,292	0.0

Table 19. Airflow resistivity results with a 2 mm diameter hole in the air supply and the differential pressure pipe – 20 mm porous aluminium. Percentage error is based on the value in Table 17.

Differential pressure (Pa)	Flow velocity (l/min)	Airflow resistivity ($Pa.s/m^2$)	Percentage error (%)
1.08	0.235	108,284	2.7

5.1.3 Comparison of the ISO and high temperature test rigs

To check that the high temperature test rig gave nominally identical results to the ISO 9053-1 test rig when both measurements were carried out at room temperature (20°C), experiments were carried out with three different densities of alkaline earth silicate fibrous materials, 64, 96 and 128 kg/m^3 (i.e. Material ID Nos. 0048, 0064 and 0058). In these measurements, the high temperature test rig incorporates the packing material in the preheating chamber.

The reason to look for differences using different density materials is that the test sample holders are different and therefore 'soft' (low density) and 'stiff' (high density) samples might be fitted differently in the two test rigs. This is partly due to the ISO rig being transparent which allows the experimenter to see the fitted sample (which is not possible with the high temperature rig) and partly due to the different length of the sample holder tubes.

Single samples

The results for single samples at room temperature are given in Table 20 and Table 21. These results show that the airflow resistivity increases with increasing density. In order to assess the extent of variability in relation to the mean population and the reproducibility of the data, coefficient of variation (CoV) is also calculated. CoV is defined as the ratio of the standard deviation to the mean and they show that the CoV is highest for the low density material; this could be due to distortion (e.g. compression) of these 'soft' test specimens when positioned in the test holder or due to larger variation in the physical properties between samples. The CoV is also higher for the 128 kg/m^3 samples than the 96 kg/m^3 samples; this might be due to air gaps around the edges occurring with the relatively stiff, high density samples that would have led to lower values of airflow resistivity.

The next step is to carry out statistical tests to compare the results from the two test rigs. For material ID No. 0048 (64 kg/m^3), differences between the ISO 9053 and high temperature test rigs for single samples are assessed using an independent samples test for which the SPSS output is given in Table 22. Equal variances can be assumed; hence there is a statistically significant difference (p<0.05) between the airflow resistivity of single samples in the ISO test rig (M=10,303.0 SD=1063.6) and the high temperature test rig (M=7940.2 SD=1158.5). Single samples in the ISO test rig have higher airflow resistivity than those in the high temperature test rig; t (18) = 4.75 p=0.00.

Table 20. Airflow resistivity measured in the ISO test rig for single samples of AES material at room temperature.

Density (kg/m^3)	Material ID No.	Thickness (mm)	Differential pressure (Pa)	Volumetric flow rate (l/min)	Airflow resistivity ($Pa.s/m^2$)	Average ($Pa.s/m^2$)	Std. deviation ($Pa.s/m^2$)	CoV (-)
64	0048	40	0.25	0.236	12,480	10,373	983	0.094
		43	0.23	0.236	10,680			
		44	0.23	0.236	10,438			
		38	0.18	0.236	9,633			
		44	0.23	0.236	10,438			
		56	0.26	0.236	9,271			
		50	0.24	0.236	9,585			
		46	0.23	0.236	9,984			
		40	0.23	0.236	11,481			
		41	0.20	0.236	9,740			
96	0064	50	0.94	0.237	37,381	36,479	706	0.019
		54.8	0.97	0.236	35,344			
		48	0.88	0.235	36,763			
		43	0.78	0.236	36,220			
		49.8	0.92	0.236	36,888			
		49.2	0.91	0.235	37,089			
		49	0.89	0.235	36,422			
		48.8	0.90	0.235	36,982			
		54	0.95	0.235	35,278			
		49	0.89	0.235	36,422			
128	0058	51	2.36	0.235	92,793	102,016	6710	0.066
		42.6	2.26	0.226	110,619			
		48	2.32	0.235	96,921			
		45	2.31	0.235	102,937			
		51	2.35	0.235	92,400			
		45	2.32	0.236	103,383			
		47	2.35	0.235	99,839			
		42	2.34	0.234	111,722			
		46	2.34	0.234	102,443			
		44	2.31	0.231	107,100			

Table 21. Airflow resistivity measured in the high temperature test rig for single samples of AES material at room temperature.

Density (kg/m^3)	Material ID No.	Thickness (mm)	Differential pressure (Pa)	Volumetric flow rate (l/min)	Airflow resistivity ($Pa.s/m^2$)	Average ($Pa.s/m^2$)	Std. deviation ($Pa.s/m^2$)	CoV (-)
64	0048	48	0.18	0.236	7,488	7,940	1158	0.146
		50	0.20	0.235	8,021			
		42	0.14	0.236	6,656			
		41	0.20	0.236	9,887			
		43	0.15	0.236	6,965			
		48	0.23	0.236	9,568			
		50	0.17	0.236	6,789			
		51	0.23	0.236	9,005			
		48	0.18	0.236	7,488			
		53	0.20	0.236	7,535			
96	0064	42	0.78	0.236	37,083	37,448	624	0.017
		35	0.65	0.236	37,083			
		40	0.74	0.236	36,940			
		46	0.87	0.236	37,765			
		40	0.75	0.236	37,439			
		35	0.68	0.236	38,794			
		35	0.66	0.236	37,653			
		39	0.73	0.236	37,375			
		35	0.64	0.236	36,512			
		38	0.72	0.236	37,834			
128	0058	47	2.54	0.236	107,829	107,102	2349	0.022
		44	2.33	0.236	105,738			
		48	2.57	0.236	106,766			
		46	2.49	0.236	108,078			
		45	2.41	0.236	106,938			
		49	2.67	0.235	109,145			
		52	2.65	0.236	101,759			
		49	2.65	0.236	107,989			
		48	2.64	0.236	110,552			
		50	2.66	0.236	106,228			

Table 22. Statistical output from an independent samples test for the ISO and high temperature test rigs: Single samples of material ID No.0048 (64 kg/m^3).

Group Statistics					
	Test rig	N	Mean (Pa.s/m^2)	Std. Deviation (Pa.s/m^2)	Std. Error Mean (Pa.s/m^2)
Airflow resistivity (Pa.s/m^2)	ISO rig	10	10303.0	1063.6	336.3
	High temperature test rig	10	7940.2	1158.5	366.3

Independent Samples Test										
		Levene's Test for Equality of Variances		t-test for Equality of Means						
									95% Confidence Interval of the Difference	
		F	Sig.	t	df	Sig. (2-tailed)	Mean Difference	Std. Error Difference	Lower	Upper
Airflow resistivity (Pa.s/m^2)	Equal variances assumed	.267	.611	4.751	18	.000	2362.800	497.331	1317.946	3407.654
	Equal variances not assumed			4.751	17.870	.000	2362.800	497.331	1317.401	3408.199

For material ID No. 0064 (96 kg/m^3), differences between the ISO 9053 and high temperature test rigs for single samples are assessed using an independent samples test for which the SPSS output is given in Table 23. Equal variances can be assumed and there is a statistically significant difference (p<0.05) between the airflow resistivity of single samples in the ISO test rig (M=36,478.9 SD=706.3) and the high temperature test rig (M=37,447.8 SD=624.4). Single samples in the high temperature test rig have higher airflow resistivity than in the ISO 9053 test rig; t (18) = -3.25 p=0.004.

Table 23. Statistical output from an independent samples test for the ISO and high temperature test rigs: Single samples of material ID No.0064 (96 kg/m^3).

Group Statistics					
	Test rig	N	Mean (Pa.s/m^2)	Std. Deviation (Pa.s/m^2)	Std. Error Mean (Pa.s/m^2)
Airflow resistivity (Pa.s/m^2)	ISO rig	10	36478.9	706.4	223.4
	High temperature test rig	10	37447.8	624.4	197.5

Independent Samples Test										
		Levene's Test for Equality of Variances		t-test for Equality of Means						
		F	Sig.	t	df	Sig. (2-tailed)	Mean Difference	Std. Error Difference	95% Confidence Interval of the Difference	
									Lower	Upper
Airflow resistivity (Pa.s/m^2)	Equal variances assumed	.244	.627	-3.25	18	.004	-968.900	298.144	-1595.28	-342.522
	Equal variances not assumed			-3.25	17.733	.005	-968.200	298.144	-1595.96	-341.845

For material ID No. 0058 (128 kg/m^3), differences between the ISO 9053 and high temperature test rigs for single samples are assessed using an independent samples test for which the SPSS output is given in Table 24. Equal variances can be assumed; hence there is a statistically non-significant difference (p>0.05) between the airflow resistivity of single samples in the ISO test rig (M=102,015.7 SD=6709.8) and the high temperature test rig (M=107,102.2 SD=2348.9); t (18) = -2.263 p=0.066.

Table 24. Statistical output from an independent samples test for the ISO and high temperature test rigs: Single samples of material ID No.0058 (128 kg/m^3).

Group Statistics					
	Test rig	N	Mean (Pa.s/m^2)	Std. Deviation (Pa.s/m^2)	Std. Error Mean (Pa.s/m^2)
Airflow resistivity (Pa.s/m^2)	ISO rig	10	102015.7	6709.8	2121.8
	High temperature test rig	10	107102.2	2348.9	742.8

Independent Samples Test										
		Levene's Test for Equality of Variances		t-test for Equality of Means						
									95% Confidence Interval of the Difference	
		F	Sig.	t	df	Sig. (2-tailed)	Mean Difference	Std. Error Difference	Lower	Upper
Airflow resistivity (Pa.s/m^2)	Equal variances assumed	7.498	.614	-2.263	18	.066	-5086.5	2248.085	-9809.552	-363.448
	Equal variances not assumed			-2.263	11.173	.065	-5086.5	2248.085	-10025.16	-147.841

The finding that there were significant differences for the lowest density and non-significant differences for the highest density could be due to different fixing of the low density samples in the test rigs. The ISO test rig is transparent which allows a clear check on the sample position and therefore the fitting is expected to be better with this test rig than with the high temperature test rig which is opaque.

The airflow resistivity was measured at room temperature using the ISO test rig according to ISO 9053-1 [2] (which also satisfies the requirements of ASTM C522 [7]). Ten samples were measured for each of the sixteen different types of material. The measured airflow resistivity data are given in Table 25.

Table 25. Airflow resistivity results at room temperature for the ISO test rig.

Material ID No.	No of samples tested	Average thickness (mm)	Airflow resistivity ($Pa.s/m^2$)		
			Average	Std. deviation	CoV (-)
0048	10	64	8,981	353	0.039
0050	10	49	82,366	8,709	0.106
0051	10	46	54,249	1,418	0.026
0052	10	48	42,765	1,110	0.026
0053	10	47	36,368	933	0.026
0054	10	47	28,373	1,657	0.058
0055	10	43	18,714	1,198	0.064
0056	10	48	14,397	270	0.019
0057	10	45	90,692	6,944	0.077
0058	10	46	102,016	6,710	0.066
0059	10	50	82,664	4,605	0.056
0060	10	50	50,211	4,255	0.085
0061	10	45	48,291	13,237	0.274
0062	10	48	33,728	2,088	0.062
0063	10	52	44,366	935	0.021
0064	10	50	36,479	706	0.019

Double samples

From Section 5.2.2 the differential pressure at high temperatures is lower than at room temperature; hence it is expected that instead of a single sample, two samples might need to be stacked on top of each other (i.e. a double sample) to give a measurable differential pressure. Measurements of double samples at room temperature were carried out for the same three densities of material as with the single samples. Results are given in Table 26 and Table 27.

The CoV values for all double samples are lower than the corresponding single samples, particularly for the low density material (this is attributed to the mixing of two different samples of this more variable material). The lower CoV is beneficial as it allows for a more rigorous assessment of any differences between the ISO and high temperature test rigs.

Table 26. Airflow resistivity from the ISO test rig for double samples of AES material at room temperature.

Density (kg/m^3)	Material ID No.	Thickness (mm)	Differential pressure (Pa)	Volumetric flow rate (l/min)	Airflow resistivity ($Pa.s/m^2$)	Average ($Pa.s/m^2$)	Std. deviation ($Pa.s/m^2$)	CoV (-)
64	0048	103	0.55	0.236	10,662	10,106	331	0.033
		106	0.53	0.236	9,984			
		96	0.48	0.236	9,984			
		100	0.51	0.236	10,184			
		82	0.41	0.236	9,984			
		100	0.52	0.236	10,383			
		96	0.47	0.236	9,776			
		86	0.44	0.236	10,216			
		84	0.40	0.236	9,508			
		102	0.53	0.236	10,375			
96	0064	80	1.50	0.236	37,439	37,312	605	0.016
		75	1.43	0.236	38,072			
		80	1.51	0.236	37,689			
		77	1.46	0.236	37,861			
		82	1.53	0.236	37,257			
		80	1.50	0.236	37,439			
		85	1.55	0.236	36,412			
		82	1.55	0.236	37,744			
		80	1.48	0.236	36,940			
		87	1.58	0.236	36,263			
128	0058	90	4.64	0.236	102,945	103,145	4879	0.047
		96	4.68	0.236	97,343			
		86	4.60	0.231	109,116			
		90	4.69	0.236	104,054			
		87	4.68	0.236	107,413			
		85	4.53	0.236	106,416			
		100	4.71	0.236	94,048			
		95	4.70	0.236	98,788			
		87	4.63	0.236	106,265			
		88	4.63	0.236	105,057			

Table 27. Airflow resistivity from the high temperature test rig for double samples of AES material at room temperature.

Density (kg/m^3)	Material ID No.	Thickness (mm)	Differential pressure (Pa)	Volumetric flow rate (l/min)	Airflow resistivity ($Pa.s/m^2$)	Average ($Pa.s/m^2$)	Std. deviation ($Pa.s/m^2$)	CoV (-)
64	0048	90	0.48	0.236	10,649	9,961	581	0.059
		88	0.43	0.236	9,757			
		92	0.44	0.236	9,550			
		90	0.47	0.236	10,428			
		86	0.42	0.236	9,752			
		87	0.46	0.236	10,558			
		85	0.41	0.236	9,631			
		83	0.40	0.236	9,623			
		84	0.45	0.236	10,697			
		98	0.44	0.236	8,965			
96	0064	79	1.49	0.236	37,661	37,766	394	0.010
		74	1.41	0.236	38,047			
		80	1.49	0.236	37,190			
		77	1.45	0.236	37,602			
		80	1.50	0.236	37,439			
		79	1.48	0.236	37,408			
		79	1.52	0.236	38,419			
		80	1.53	0.236	38,188			
		78	1.47	0.236	37,631			
		75	1.43	0.236	38,072			
128	0058	87	4.61	0.236	105,806	105,284	1948	0.0185
		88	4.65	0.236	105,511			
		90	4.80	0.236	106,494			
		92	4.87	0.236	105,699			
		85	4.55	0.236	106,886			
		98	4.92	0.236	100,246			
		100	5.20	0.236	103,832			
		93	4.94	0.236	106,065			
		87	4.63	0.236	106,265			
		87	4.62	0.236	106,035			

For material ID No. 0048 (64 kg/m^3), differences between the ISO and high temperature test rigs for double samples are assessed using an independent samples test for which the SPSS output is given in Table 28. Equal variances can be assumed and hence there is a statistically non-significant difference at the significance level of 0.05 for airflow resistivity of double samples in the ISO test rig (*M*=10,105.6 *SD*=331.2) and for double samples in the high temperature test rig (*M*=9,961.0 *SD*=583.0); *t* (18) = 0.682, *p*=0.504.

Table 28. Statistical output from an independent samples test for the ISO and high temperature test rigs: Material ID No.0048 (64 kg/m^3).

Group Statistics					
	Test rig	N	Mean (Pa.s/m^2)	Std. Deviation (Pa.s/m^2)	Std. Error Mean (Pa.s/m^2)
Airflow resistivity (Pa.s/m^2)	ISO test rig	10	10105.6	331.3	104.8
	High temperature test rig	10	9961.0	583.0	184.4

Independent Samples Test										
		Levene's Test for Equality of Variances		t-test for Equality of Means						
									95% Confidence Interval of the Difference	
		F	Sig.	t	df	Sig. (2-tailed)	Mean Difference	Std. Error Difference	Lower	Upper
Airflow resistivity (Pa.s/m^2)	Equal variances assumed	5.704	.068	0.682	18	.504	-144.600	212.040	-300.879	590.079
	Equal variances not assumed			0.682	14.263	.506	-144.600	212.040	-309.396	598.596

For material ID No. 0064 (96 kg/m^3), differences between the ISO and high temperature test rigs for double samples are assessed using an independent samples test for which the SPSS output is given in Table 29. Equal variances can be assumed and hence there is a statistically non-significant difference at the significance level of 0.05 for airflow resistivity of double samples in the ISO rig (*M*=37,311.6 *SD*=604.8) and airflow resistivity of double samples in high temperature test rig (*M*=37,765.7 *SD*=394.4); *t* (18) = -1.99 *p*=0.062.

Table 29. Statistical output from an independent samples test for the ISO and high temperature test rigs: Material ID No.0064 (96 kg/m^3)

Group Statistics					
	Orientation	*N*	Mean (Pa.s/m^2)	Std. Deviation (Pa.s/m^2)	Std. Error Mean (Pa.s/m^2)
Airflow resistivity (Pa.s/m^2)	ISO test rig	10	37311.6	604.8	191.2
	High temperature test rig	10	37765.7	394.4	124.7

Independent Samples Test										
		Levene's Test for Equality of Variances		t-test for Equality of Means						
									95% Confidence Interval of the Difference	
		F	Sig.	t	df	Sig. (2-tailed)	Mean Difference	Std. Error Difference	Lower	Upper
Airflow resistivity	Equal variances assumed	1.369	.257	-1.99	18	.062	-454.100	228.325	-933.794	25.594
	Equal variances not assumed			-1.99	15.483	.065	-454.100	228.325	-939.445	31.245

For material ID No. 0058 (128 kg/m^3), differences between the ISO and high temperature test rigs for double samples are assessed using an independent samples test for which the SPSS output is given in Table 30. Equal variances can be assumed and hence there is a statistically non-significant difference at the significance level of 0.05 for airflow resistivity of double samples in ISO test rig (*M*=103,144.5 *SD*=4878.8) and airflow resistivity of double samples in high temperature test rig (*M*=105,283.9 *SD*=1948.0); t (18) = -1.29 p=0.21.

Table 30. Statistical output from an independent samples test for the ISO and high temperature test rigs: Material ID No.0058 (128 kg/m^3).

Group Statistics					
	Rig	N	Mean (Pa.s/m^2)	Std. Deviation (Pa.s/m^2)	Std. Error Mean (Pa.s/m^2)
Airflow resistivity (Pa.s/m^2)	ISO test rig	10	103144.5	4878.8	1542.8
	High temperature test rig	10	105283.9	1948.0	616.0

Independent Samples Test										
		Levene's Test for Equality of Variances		t-test for Equality of Means						
									95% Confidence Interval of the Difference	
		F	Sig.	t	df	Sig. (2-tailed)	Mean Difference	Std. Error Difference	Lower	Upper
Airflow resistivity (Pa.s/m^2)	Equal variances assumed	7.549	.213	-1.29	18	.214	-2139.4	1661.256	-5629.57	1350.77
	Equal variances not assumed			-1.29	11.799	.222	-2139.4	1661.256	-5765.83	1487.03

These statistical tests show that for double samples, there is no significant difference between the two test rigs. This is a more reliable conclusion than with single samples because the CoV values are lower with double samples.

Thickness of single and double samples

The next consideration is whether the use of double samples leads to increased compression of the material inside the test rigs than with single samples. Compression of fibrous materials means that the airflow resistivity is related to the material density inside the test rig rather than the density quoted by the manufacturer. This makes it important to measure the thickness of the sample when fitted inside the test rig as this thickness is needed to calculate airflow resistivity.

The difference between the thickness of single samples and the equivalent single sample thickness (i.e. the double sample thickness divided by two) are assessed using an independent samples test for each test rig which the SPSS output is given in Table 31 and Table 32. Equal variance can be assumed and hence there is a statistically significant difference (p<0.05)

between the thickness of single samples in both ISO rig (*M*=49.56 *SD*=3.24) and high temperature test rig (*M*=43.45 *SD*=4.34) and equivalent single sample thickness when both ISO rigs have double samples (*M*=40.40 *SD*=1.74) and high temperature rig have double samples (*M*=40.92 *SD*=1.02); t (18) = 7.88 p=0.000 , t (18) = 3.59 p=0.002 (p<0.05). This statistical test indicates that with double samples, the material is more compressed than when single samples are used.

Table 31. Statistical output from an independent samples test for the thickness of single samples and the equivalent single sample thickness from double samples - ISO test rig.

Group Statistics					
	Sample type	N	Mean (mm)	Std. Deviation (mm)	Std. Error Mean(mm)
Thickness (mm)	Single	30	49.56	3.24	1.02
	Double	30	40.40	1.74	0.55

Independent Samples Test										
		Levene's Test for Equality of Variances		t-test for Equality of Means						
									95% Confidence Interval of the Difference	
		F	Sig.	t	df	Sig. (2-tailed)	Mean Difference	Std. Error Difference	Lower	Upper
Thickness (mm)	Equal variances assumed	.906	.354	7.880	18	.000	9.1600	1.1625	6.7177	11.6023
	Equal variances not assumed			7.880	13.826	.000	9.1600	1.1625	6.6638	11.6562

Table 32. Statistical output from an independent samples test for the thickness of single samples and the equivalent single sample thickness from double samples - high temperature test rig.

Group Statistics					
	Sample type	N	Mean (mm)	Std. Deviation (mm)	Std. Error Mean(mm)
Thickness (mm)	Single	30	43.55	4.34	1.31
	Double	30	40.92	1.02	0.29

Independent Samples Test										
		Levene's Test for Equality of Variances		t-test for Equality of Means						
									95% Confidence Interval of the Difference	
		F	Sig.	t	df	Sig. (2-tailed)	Mean Difference	Std. Error Difference	Lower	Upper
Thickness (mm)	Equal variances assumed	40.717	.000	3.592	18	.002	4.6288	1.2887	1.9489	7.3087
	Equal variances not assumed			3.448	11.008	.005	4.6288	1.3425	1.6743	7.5832

Comparison of airflow resistivity from single and double samples in each test rig

In theory, the airflow resistivity measured for single and double samples should be the same if the fitting, and any compression of the samples inside the sample holder is identical. However, as there was evidence of compression when fitting double samples the following analysis compares the average airflow resistivity from single samples with double samples that were all taken from the same material code/batch. This assessment was carried out for both the ISO and high temperature test rigs.

For the ISO test rig

For material ID No.0048 (64 kg/m^3) differences between single and double samples in the ISO test rig are assessed using an independent samples test for which the SPSS output is given in Table 33. Equal variances cannot be assumed and there is a statistically non-significant

difference (p=0.05) for airflow resistivity of single samples (M=10,373.0 SD=983.5) and airflow resistivity of double samples (M=10105.6 SD=331.3) indicating both single and double samples inside the ISO test rig have approximately similar airflow resistivity; t (18) = -0.815 p=0.432.

For material ID No: 0064 (96 kg/m^3) differences between single and double samples in the ISO test rig are assessed using an independent samples test for which the SPSS output is given in Table 34. Equal variances can be assumed and there is a statistically significant difference (p=0.05) for airflow resistivity of single samples (M=36,478.9 SD=706.4) and airflow resistivity of double samples (M= 37,311.6 SD=604.8); t (18) = -2.83 p=0.01.

For material ID No.0058 (128 kg/m^3) differences between single and double samples in the ISO test rig are assessed using an independent samples test for which the SPSS output is given in Table 35. Equal variances can be assumed and there is a statistically non-significant difference (p=0.05) for airflow resistivity of single samples (M=102,015.7 SD=6709.8) and of double samples (M=103,144.5 SD=4878.8); t (18) =-0.43 p=0.67.

In conclusion for the ISO test rig, there is a statistically significant difference in the airflow resistivity between single and double samples of the 96 kg/m^3 material but not for the 64 and 128 kg/m^3 materials.

Table 33. Statistical output from an independent samples test for single and double samples in the ISO test rig: Material ID No.0048 (64 kg/m^3).

Group Statistics					
	Sample type	N	Mean (Pa.s/m^2)	Std. Deviation (Pa.s/m^2)	Std. Error Mean (Pa.s/m^2)
Airflow resistivity (Pa.s/m^2)	Single	10	10373.0	983.5	311.0
	Double	10	10105.6	331.3	104.8

Independent Samples Test										
		Levene's Test for Equality of Variances		t-test for Equality of Means						
		F	Sig.	t	df	Sig. (2-tailed)	Mean Difference	Std. Error Difference	95% Confidence Interval of the Difference	
									Lower	Upper
Airflow resistivity (Pa.s/m^2)	Equal variances assumed	5.434	.032	0.815	18	.426	267.400	328.166	-422.050	956.850
	Equal variances not assumed			0.815	11.01	.432	267.400	328.166	-454.758	989.558

Table 34. Statistical output from an independent samples test for single and double samples in the ISO test rig: Material ID No.0064 (96 kg/m^3).

Group Statistics					
	Sample type	N	Mean (Pa.s/m^2)	Std. Deviation (Pa.s/m^2)	Std. Error Mean (Pa.s/m^2)
Airflow resistivity (Pa.s/m^2)	Single	10	36478.9	706.4	223.4
	Double	10	37311.6	604.8	191.2

Independent Samples Test										
		Levene's Test for Equality of Variances		t-test for Equality of Means						
		F	Sig.	t	df	Sig. (2-tailed)	Mean Difference	Std. Error Difference	95% Confidence Interval of the Difference	
									Lower	Upper
Airflow resistivity (Pa.s/m^2)	Equal variances assumed	0.155	.698	-2.83	18	.011	-832.700	294.065	-1450.507	-214.893
	Equal variances not assumed			-2.83	17.583	.011	-832.700	294.065	-1451.560	-213.840

Table 35. Statistical output from an independent samples test for single and double samples in the ISO test rig: Material ID No.0058 (128 kg/m^3).

Group Statistics					
	Sample type	N	Mean (Pa.s/m^2)	Std. Deviation (Pa.s/m^2)	Std. Error Mean (Pa.s/m^2)
Airflow resistivity (Pa.s/m^2)	Single	10	102015.7	6709.8	2121.8
	Double	10	103144.5	4878.8	1542.8

Independent Samples Test										
		Levene's Test for Equality of Variances		t-test for Equality of Means						
									95% Confidence Interval of the Difference	
		F	Sig.	t	df	Sig. (2-tailed)	Mean Difference	Std. Error Difference	Lower	Upper
Airflow resistivity	Equal variances assumed	0.816	.378	-0.43	18	.672	-1128.80	2623.442	-6640.448	4382.848
	Equal variances not assumed			-0.43	16.438	.673	-1128.80	2623.442	-6678.240	4420.640

For the high temperature test rig:

For material ID No: 0048 (64 kg/m^3) differences between single and double samples in the high temperature test rig at room temperature are assessed using an independent samples test for which the SPSS output is given in Table 36. Equal variances can be assumed and there is a statistically significant difference (p=0.05) for airflow resistivity of single samples (M=7,940.2 SD=1158.4) and of double samples (M=10105.6 SD=331.3); t (18) = -5.68 p=0.00.

For material ID No: 0064 (96 kg/m^3) differences between single and double samples in the high temperature test rig at room temperature are assessed using an independent samples test for which the SPSS output is given in Table 37. Equal variances can be assumed and there is a statistically non-significant difference (p=0.05) for airflow resistivity of single samples (M=37,447.8 SD=624.4) and of double samples in the high temperature test rig (M= 37,765.7 SD=394.4; t (18) = -1.36 p=0.19.

For material ID No: 0058 (128 kg/m^3) differences between single and double samples in the high temperature test rig at room temperature are assessed using an independent samples test for which the SPSS output is given in Table 38. Equal variances can be assumed and there is a statistically non-significant difference (p=0.05) for airflow resistivity of single samples (M=107,102.2 SD=2348.9) and of double samples (M=105,283.9 SD=1948.0; t (18) =1.88 p=0.08.

For the high temperature test rig, there is a statistically significant difference in the airflow resistivity between single and double samples of the 64 and 128 kg/m^3 materials but not the 96 kg/m^3 material. These results are opposite to the ISO rig which indicates an effect due to the different fitting of the samples in the two test rigs. The commercial implication is that when measurements are made using double (or more) stacks of samples, the measured airflow resistivity will not always correspond to the thickness of the product which is sold and installed. Since different fitting of samples in the two test rigs causes a statistically significance difference in the airflow resistivity of samples in the two test rigs, it is recommended to fabricate future high temperature test rigs using a material which is transparent. However fabrication costs for material such as quartz will often be prohibitive.

Table 36. Statistical output from an independent samples test for single and double samples in high temperature test rig: Material ID No.0048 (64 kg/m^3).

Group Statistics					
	Sample type	N	Mean (Pa.s/m^2)	Std. Deviation (Pa.s/m^2)	Std. Error Mean (Pa.s/m^2)
Airflow resistivity (Pa.s/m^2)	Single	10	7940.2	1158.5	366.3
	Double	10	10105.6	331.3	104.8

Independent Samples Test										
		Levene's Test for Equality of Variances		t-test for Equality of Means						
		F	Sig.	t	df	Sig. (2-tailed)	Mean Difference	Std. Error Difference	95% Confidence Interval of the Difference	
									Lower	Upper
Airflow resistivity	Equal variances assumed	12.135	.003	-5.683	18	.000	-2165.400	381.026	-2965.91	-1364.895

	Equal variances not assumed			-5.683	10.462	.000	-2165.400	381.026	-3009.33	-1321.475

Table 37. Statistical output from an independent samples test for single and double samples in the high temperature test rig: Material ID No.0064 (96 kg/m^3).

Group Statistics					
	Sample type	N	Mean (Pa.s/m^2)	Std. Deviation (Pa.s/m^2)	Std. Error Mean (Pa.s/m^2)
Airflow resistivity (Pa.s/m^2)	Single	10	37447.8	624.4	197.5
	Double	10	37765.7	394.4	124.7

Independent Samples Test										
		Levene's Test for Equality of Variances		t-test for Equality of Means						
									95% Confidence Interval of the Difference	
		F	Sig.	t	df	Sig. (2-tailed)	Mean Difference	Std. Error Difference	Lower	Upper
Airflow resistivity (Pa.s/m^2)	Equal variances assumed	0.712	.410	-1.361	18	.190	-317.900	233.556	-808.583	172.783
	Equal variances not assumed			-1.361	15.195	.190	-317.900	233.556	-815.156	179.356

Table 38. Statistical output from an independent samples test for single and double samples in the high temperature test rig: Material ID No.0058 (128 kg/m^3).

Group Statistics					
	Sample type	N	Mean (Pa.s/m^2)	Std. Deviation (Pa.s/m^2)	Std. Error Mean (Pa.s/m^2)
Airflow resistivity (Pa.s/m^2)	Single	10	107102.2	2348.9	742.8
	Double	10	105283.9	1948.0	616.0

Independent Samples Test										
		Levene's Test for Equality of Variances		t-test for Equality of Means						
		F	Sig.	t	df	Sig. (2-tailed)	Mean Difference	Std. Error Difference	95% Confidence Interval of the Difference	
									Lower	Upper
Airflow resistivity (Pa.s/m^2)	Equal variances assumed	12.135	.003	-5.683	18	.000	-2165.400	381.026	-2965.91	-1364.895
	Equal variances not assumed			-5.683	10.462	.000	-2165.400	381.026	-3009.33	-1321.475

5.1.4 Regression analysis for different density materials

In Chapter 3, a review of the literature indicated that it is possible to use regression analysis to give relationships between airflow resistivity and bulk density by taking the logarithm of both parameters. This section assess the regression curves from the two test rigs for which linear regression using the three densities of material (64, 96, 128 kg/m^3). As noted there are differences between single and double samples which gives a reason to carry out two different regression analyses. The first considers only single samples to give regression lines that correspond to the manufactured thickness. The second considers both single and double samples to give the best estimate of a relationship between airflow resistivity and bulk density that could apply to any thickness of material.

5.1.4.1 Single samples

For single samples the straight-line regression coefficients are shown in Table 39. These regression lines are plotted along with the individual data points in Figure 43.

Table 39. Regression coefficients for single samples in the ISO and high temperature test rigs at room temperature.

Test rig	No of Samples	Gradient	Intercept	Coefficient of determination, R^2	Standard error
ISO	30	3.36895	-2.08043	0.9975	0.0210
High temperature	30	3.526	-2.41167	0.9941	0.0371

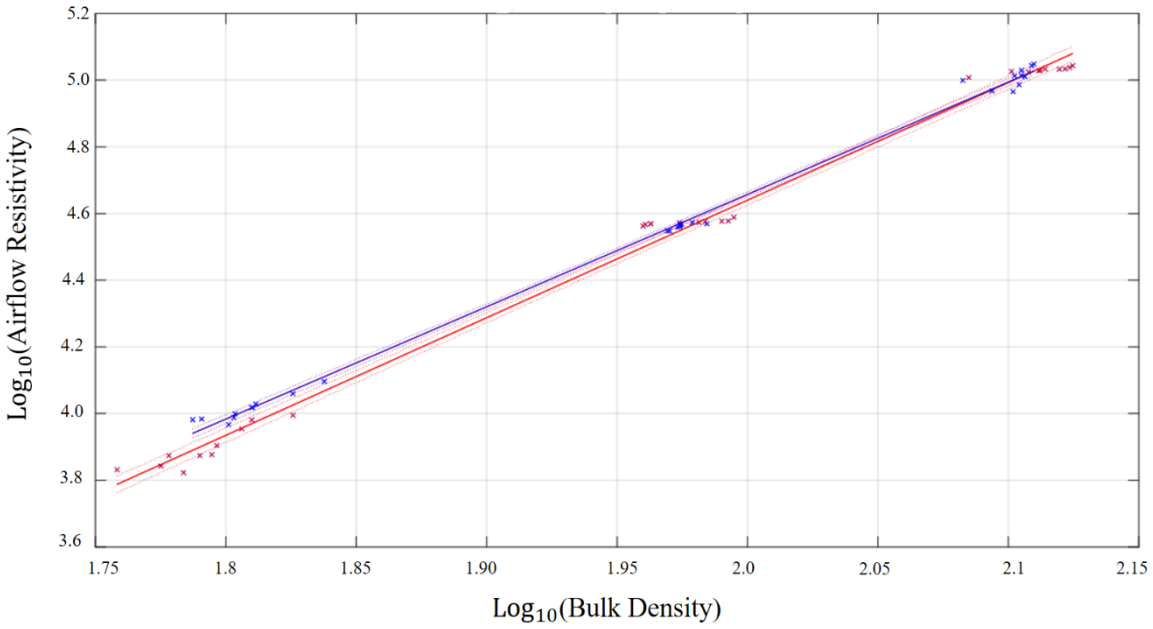

Figure 43. Relationship between airflow resistivity of single samples and bulk density at room temperature: Regression plots for the ISO test rig (blue) and the high temperature test rig (red).

To assess whether there is a statistically significant difference between the regression lines from the two test rigs, the following analysis of variance considers the combination of data from both test rigs. For this combination of test rigs, this gives the following regression equation with an R^2 of 0.995:

$$\log_{10}(r) = -2.41167 + 3.526 \log_{10}(\rho_{bulk}) + 0.331241(Rig) - 0.157048 * \log_{10}(\rho_{bulk}) * (Rig) \quad (72)$$

where Rig is an indicator variable which takes the value 1 if it is the ISO test rig and 0 if it is the high temperature test rig.

The results of a one-way analysis of variance on these two linear regression models are shown in Table 40 by considering intercepts (F (1, 3) =8.94, p<0.05) and gradients (F (1, 3) =6.46, p<0.05). This shows that there is a statistically significant difference (p=0.05) between the intercepts and gradients for the two different types of rigs. It is therefore concluded that the airflow resistivity at room temperature depends on the rig type.

Table 40. Relationship between airflow resistivity of single samples and bulk density at room temperature: ANOVA for regression variables in the order fitted

Source	Sum of squares	Degrees of freedom	Mean square	F-ratio	p value
$\log_{10}(\rho_{bulk})$	11.4678	1	11.4678	12612.73	0.0000
Intercepts	0.0081328	1	0.0081328	8.94	0.0041
Slopes	0.00587577	1	0.00587577	6.46	0.0138
Model	11.4819	3			

To try and gain more insight into the influence of the test rig, two different types of regression models were considered:

Model 1 considered the effect of the test rig as an addition effect only, i.e.
$\log_{10}(r) \sim \log_{10}(\rho_{bulk}) + Rig$

Model 2 considered the effect of the test rig as an addition and interaction effect, i.e.
$\log_{10}(r) \sim \log_{10}(\rho_{bulk}) * Rig$

For Model 1 the regression analysis gives the following:

$\log_{10}(r)$ =-2.27155+3.45451*$\log_{10}$ (ρ_{bulk}) +0.02329*(Rig)

Parameter	Estimated values	Standard error	T Statistic	*p* value
Constant	-2.27155	0.06339	-35.835	0.0000
$\log_{10}(\rho_{bulk})$	3.45451	0.03220	107.265	0.0000
Rig	0.02329	0.00815	2.857	0.00596

R^2 = 99.51%

R^2 (adjusted for degrees of freedom) = 99.49%

Residual standard error of estimate =0.03157

For Model 2 the regression analysis gives the following:

$\log_{10}(r)$ =-2.41167+3.52600*$\log_{10}$ (ρ_{bulk}) +0.33124*(Rig) - 0.15705*$\log_{10}$ (ρ_{bulk})*(Rig)

Parameter	Estimated values	Standard error	T Statistic	*p* value
Constant	-2.41167	0.08188	-29.452	0.00000
$\log_{10}(\rho_{bulk})$	3.52600	0.04168	84.594	0.00000
Rig	0.33124	0.12139	2.729	0.00848
$\log_{10}(\rho_{bulk})$*Rig	-0.15705	0.06178	-2.542	0.01381

R^2 = 99.56%

R^2 (adjusted for D.F.) = 99.53%

Residual standard error = 0.03015

Null Hypothesis: Model 1 is statistically better than Model 2.

Table 41. Likelihood ratio test results.

Model 1: $\log_{10}(\text{Output}) \sim \log_{10}(\rho_{\text{bulk}}) + \text{Rig}$					
Model 2 : $\log_{10}(\text{Output}) \sim \log_{10}(\rho_{\text{bulk}}) * \text{Rig}$					
Model	Degrees of freedom	Log likelihood	Degrees of freedom	Chi square value	Pr(>chi square value)
1	4	123.75			
2	5	127.02	1	6.5528	0.01047

The likelihood ratio test was conducted for two nested regression models based on the null hypothesis that Model 1 is statistically better fitted than Model 2. The test is based on the ratio of the likelihoods of the two models. The ratio expresses how many times more likely the data are under one model than the other. This likelihood ratio can be used to compute a *p*-value, or compared to a critical value to decide whether to reject the null model. Since there is a statistically significant difference ($p<0.05$), the null hypothesis is rejected by the likelihood ratio test's results which indicates that Model 2 is better fitted than Model 1, i.e. the effect of the test rig is a multiplicative variable.

5.1.4.2 Combination of single and double samples

For the combination of single and double samples the straight-line regression coefficients are shown in Figure 44. These regression lines are plotted along with the individual data points in Table 42.

Table 42. Regression coefficients for single and double samples in the ISO and high temperature test rigs at room temperature.

Test rig	No of Samples	Gradient	Intercept	Coefficient of determination, R^2	Standard error
ISO	60	3.43456	-2.21386	0.9959	0.0265
High temperature	60	3.40916	-2.16585	0.9945	0.0475

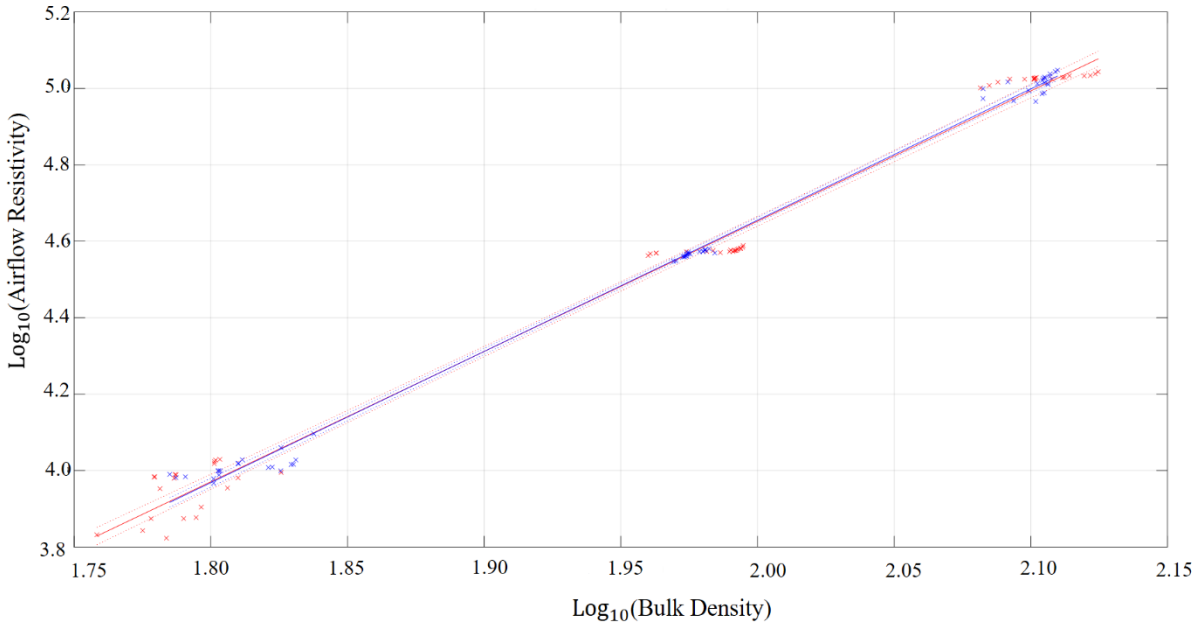

Figure 44. Relationship between airflow resistivity of single and double samples and bulk density at room temperature: Regression plots for the ISO test rig (blue) and the high temperature test rig (red).

To assess whether there is a statistically significant difference between the regression lines from the two test rigs, the following analysis of variance considers the combination of data from both test rigs. For this combination of test rigs, this gives the following regression equation with an R^2 of 0.992:

$$\log_{10}(r) = -2.16585 + 3.40916 \log_{10}(\rho_{bulk}) - 0.0480106(\text{Rig}) + 0.0254 * \log_{10}(\rho_{bulk}) * (\text{Rig}) \quad (73).$$

where Rig is an indicator variable which takes the value 1 if it is the ISO test rig and 0 if it is the high temperature test rig

The results of a one-way analysis of variance on these two linear regression models are shown in Table 49 by considering intercepts (F (1, 3) =0.07, p>0.05) and gradients (F (1, 3) =0.20, p>0.05). This shows that there is a statistically non-significant difference (p=0.05) between the intercepts and gradients for the two different types of rigs. It is therefore concluded that the room temperature airflow resistivity for single and double samples does not depend on the rig type.

Table 43. Relationship between airflow resistivity of single and double samples and bulk density at room temperature: ANOVA for regression variables in the order fitted.

Source	Sum of squares	Degrees of freedom	Mean square	F-ratio	p value
$\log_{10}(\rho_{bulk})$	21.7752	1	21.7752	14678.65	0.0000
Intercepts	0.0000985115	1	0.0000985115	0.07	0.7971
Slopes	0.000297907	1	0.000297907	0.20	0.6549
Model	21.7756	3			

To gain more insight into the influence of the test rig, two different types of regression models were considered:

Model 1 considered the effect of the test rig as an addition effect only, i.e.
$\log_{10}(r) \sim \log_{10}(\rho_{bulk}) + Rig$

Model 2 considered the effect of the test rig as an addition and interaction effect, i.e.
$\log_{10}(r) \sim \log_{10}(\rho_{bulk}) * Rig$

For Model 1 the regression analysis gives the following:

$\log_{10}(r) = -2.188653 + 3.420795 * \log_{10}(\rho_{bulk}) + 0.001812 * (Rig)$

Table 44. Likelihood ratio test results

Parameter	Estimated values	Standard error	T Statistic	*p* value
Constant	-2.188653	0.055378	-39.522	0.0000
$\log_{10}(\rho_{bulk})$	3.420795	0.028141	121.558	0.0000
Rig	0.00182	0.007009	0.259	0.796

R^2 = 99.21%

R^2 (adjusted for degrees of freedom) = 99.20%

Residual standard error of estimate =0.03838

For Model 2 the regression analysis gives the following:

$\log_{10}(r)$ =-2.16585+3.40916*$\log_{10}$ (ρ_{bulk}) -0.04801*(Rig) - 0.02540*$\log_{10}$ (ρ_{bulk})*(Rig)

Table 45. Likelihood ratio test results

Parameter	Estimated values	Standard error	T Statistic	*p* value
Constant	-2.16585	0.07535	-28.744	0.00000
$\log_{10}(\rho_{bulk})$	3.40916	0.03836	88.871	0.00000
Rig	-0.04801	0.11140	-0.431	0.667
$\log_{10}(\rho_{bulk})$*Rig	-0.02540	0.05667	0.448	0.655

R^2 = 99.22%

R^2 (adjusted for D.F.) = 99.2%

Residual standard error = 0.03852

Null Hypothesis: Model 1 is statistically better than Model 2.

Model 1: $\log_{10}$(Output) ~ $\log_{10}(\rho_{bulk})$ + Rig
Model 2 : $\log_{10}$(Output) ~ $\log_{10}(\rho_{bulk})$ * Rig

Model	Degrees of freedom	Log likelihood	Degrees of freedom	Chi square value	Pr(>chi square value)
1	4	222.46			
2	5	222.56	1	0.2076	0.6487

The likelihood ratio test was conducted for two nested regression models based on the null hypothesis that Model 1 is statistically better fitted than Model 2. Since there is a non-statistically significant difference (p=0.05), the null hypothesis is accepted by the likelihood ratio test's results which indicates that Model 1 is better fitted than Model 2, i.e. the effect of the test rig is an additive variable.

In conclusion, it is reasonable to conclude that the room temperature airflow resistivity does not depend on the rig type (even though the statistical tests for single samples indicated this) because the combined dataset for single and double samples is larger and potentially more reliable.

5.1.5 Effect of airflow velocity on the specific airflow resistance of double samples

Specific airflow resistance measurements were carried out for four different airflow velocities (0.5×10^{-3} m/s, 1×10^{-3} m/s, 2×10^{-3} m/s and 4×10^{-3} m/s – these correspond to the sound pressure levels indicated in Table 1). Three different density materials were measured and the results are shown in Table 46 and Figure 45.

Table 46. Specific airflow resistance values for different airflow velocities at room temperature.

Mass (g)	Specific airflow resistance values for different airflow velocities (Pa.s/m)			
	0.5×10^{-3} m/s	1×10^{-3} m/s	2×10^{-3} m/s	4×10^{-3} m/s
22.12	799	800	800	799
24.21	859	880	870	855
29.57	2995	2941	2906	2922
30.86	3015	3122	3027	2892

30.87	3095	3012	3047	3195
47.61	9505	9525	9575	9570
48.32	9604	9645	9665	9650

As shown in Figure 45 , the specific airflow resistance at room temperature for four different airflow velocities is proportional to the sample mass and the four regression lines are nominally identical.

A one-way analysis of variance (ANOVA) with Tukey's post –hoc test was conducted on all specific airflow resistance values for four different airflow velocities – See Table 47. Tukey's post hoc-test can use to determine which groups among the sample have significant differences. It calculates the difference between the means of all the groups and test values are number which acts as a distance between the groups. Tukey's post-hoc test works by defining a value known as Honest Significant Difference (HSD) [104]. Considering the results from four airflow velocities, it can be concluded that there is no significant difference between the specific airflow resistance values.

Table 47. Statistical test results on comparison of specific airflow resistance at room temperature for four different airflow velocities.

Specific airflow resistance (Pa.s/m)								
Airflow velocities (m/s)	N	Mean (Pa.s/m)	Std. Deviation (Pa.s/m)	Std. Error (Pa.s/m)	95% Confidence Interval for Mean (Pa.s/m)		Minimum (Pa.s/m)	Maximum (Pa.s/m)
					Lower Bound	Upper Bound		
0.5E-3 m/s	7	4267.4286	3744.34622	1415.22985	804.4859	7730.3713	799.00	9604.00
1E-3 m/s	7	4275.0000	3757.33026	1420.13735	800.0491	7749.9509	800.00	9645.00
2 E-3 m/s	7	4270.0000	3780.45906	1428.87921	773.6585	7766.3415	800.00	9665.00
4E-3 m/s	7	4269.0000	3777.47870	1427.75275	775.4149	7762.5851	799.00	9650.00
Total	28	4270.3571	3549.61384	670.81396	2893.9606	5646.7537	799.00	9665.00

ANOVA					
Specific airflow resistance (Pa.s/m)					
	Sum of Squares	df	Mean Square	F	Sig.
Between Groups	224.714	3	74.905	.000	1.000
Within Groups	340193251.714	24	14174718.821		
Total	340193476.429	27			

Multiple Comparisons						
Dependent Variable: Specific airflow resistance (Pa.s/m)						
Tukey HSD						
(I) airflow velocities (m/s)	(J) airflow velocities (m/s)	Mean Difference (I-J)	Std. Error	Sig.	95% Confidence Interval	
					Lower Bound	Upper Bound
0.5E-3	1E-3	-7.57143	2012.44122	1.000	-5559.1098	5543.9669
	2 E-3	-2.57143	2012.44122	1.000	-5554.1098	5548.9669
	4E-3	-1.57143	2012.44122	1.000	-5553.1098	5549.9669
1E-3	0.5E-3	7.57143	2012.44122	1.000	-5543.9669	5559.1098
	2 E-3	5.00000	2012.44122	1.000	-5546.5384	5556.5384
	4E-3	6.00000	2012.44122	1.000	-5545.5384	5557.5384
2E-3	0.5E-3	2.57143	2012.44122	1.000	-5548.9669	5554.1098
	1E-3	-5.00000	2012.44122	1.000	-5556.5384	5546.5384
	4E-3	1.00000	2012.44122	1.000	-5550.5384	5552.5384
4E-3	0.5E-3	1.57143	2012.44122	1.000	-5549.9669	5553.1098
	1E-3	-6.00000	2012.44122	1.000	-5557.5384	5545.5384
	2 E-3	-1.00000	2012.44122	1.000	-5552.5384	5550.5384

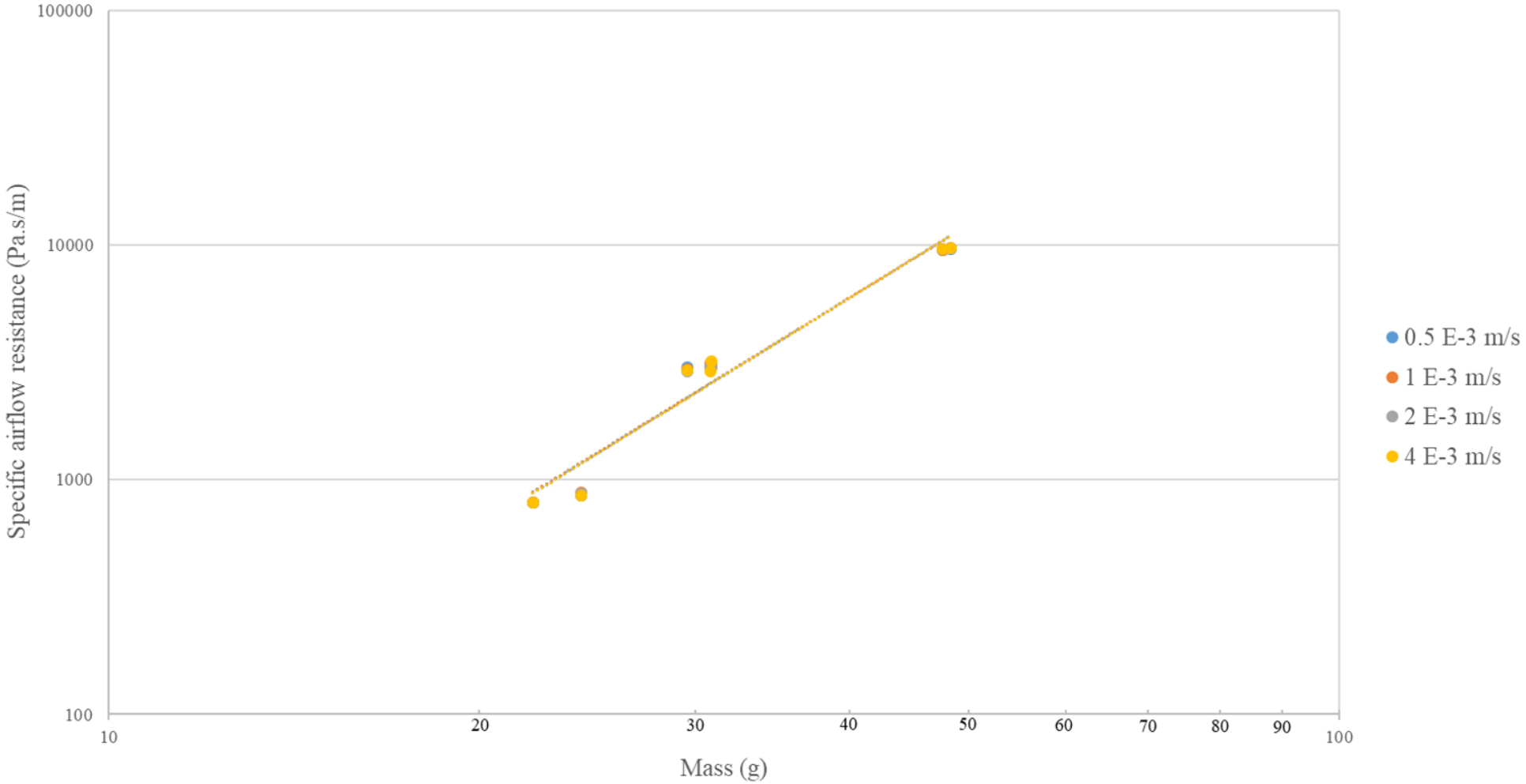

Figure 45. Specific airflow resistance at room temperature for four different airflow velocities.

5.2 High temperature measurements

High temperature experiments were conducted for three types of material samples (material ID Nos. 0048, 0064 and 0058) corresponding to three different densities of 64, 96 and 128 kg/m^3. All the test results at high temperature used double samples to ensure a measurable differential pressure.

5.2.1 Change in material thickness at high temperature

During initial experiments it was observed that the measured thickness of the material was different before and after exposure to high temperatures; hence, the airflow resistivity was calculated using the initial thickness at room temperature. In order to make sure that it was not the test rig that caused the thickness reduction, experiments were conducted under the same experimental condition as the actual high temperature experiments except without an air supply connected to the test rig. Inside the kiln, two separate sets of double samples were considered, one inside and one outside the test rig. Both sets were heated together up to 800 ℃ with a ramp rate of 100 ℃. Initial experiments were conducted up to 600 ℃ and no significant thickness change occurred. However, it was observed that a reduction in thickness occurred above 700 ℃. The thickness of 96 and 128 kg/m^3 samples were measured and shown in Table 48.

These results indicate that the double sample thickness is reduced after heating to 800 ℃ when inside and outside the test rig; hence this effect is not caused by the containment of the material inside the test rig.

According to the literature [105, 106], alkaline earth silicate is almost amorphous at the room temperature but the material undergoes crystallisation and shrinkage with increasing temperature. Crystallisation is expected to start around 900 ℃ but the properties start to change between 750 and 800 ℃ [105]. The thickness reduction is likely to occur due to the compression of the material atoms before the crystallisation.

When there is an unknown reduction in thickness at high temperature it is not appropriate to quote the airflow resistivity as the calculation requires knowledge of the thickness. Therefore when the thickness is unknown it is appropriate to calculate the specific airflow resistance

instead. The results in section 5.2.3 are included for both the specific airflow resistance and airflow resistivity as it seems feasible to continue quoting the airflow resistivity up to 600 ℃. However, in sections 5.2.4 and 1.1 where trends are assessed across the range of temperatures it will be necessary to use only one parameter, the specific airflow resistance.

Table 48. Change in thickness of the double samples when heated in the kiln to 800 ℃.

Material ID No. 0064 (96 kg/m^3)	
Materials outside the test rig	
Thickness before heating	96.5 mm
Thickness after heating	88.7 mm
Percentage change in thickness (%)	8.1
Materials inside the test rig	
Thickness before heating	98.1 mm
Thickness after heating	95.3 mm
Percentage change in thickness (%)	2.9

Material ID No. 0058 (128 kg/m^3)	
Materials outside the test rig	
Thickness before heating	104.9 mm
Thickness after heating	87.0 mm
Percentage change in thickness (%)	17.1
Materials inside the test rig	
Thickness before heating	106.0 mm
Thickness after heating	87.0 mm
Percentage change in thickness (%)	17.9

5.2.2 Differential pressure variation at high temperature

Above 600 ℃ there was not only a reduction in sample thickness but also a reduction in the differential pressure. In section 4.7, it was shown that it was necessary to correct the differential pressure; both the uncorrected and corrected results are given in Table 49 for the high temperature test rig with packing inside the preheater. However, as it is only the corrected differential pressure that is used to calculate the airflow resistivity, it is only these values that are plotted on Figure 46 for the high temperature test rig with packing inside the preheater.

For material ID Nos.0048, 0064 and 0058, from 20 to ≈600 ℃ the results indicate a general increase in the corrected differential pressure with increasing temperature up to 600 - 700 ℃ where there is a peak above which there is a reduction in the corrected differential pressure.

Table 49. Differential pressure variation of double samples in the high temperature test rig with packing.

Material ID No.	Thickness (mm)	Differential pressure (Pa)	Corrected differential pressure (Pa)	Temperature (℃)
0048	90	0.40	0.40	20
		0.47	0.60	100
		0.56	0.90	200
		0.68	1.33	300
		0.73	1.67	400
		0.86	2.26	500
		0.90	2.67	600
		0.58	1.93	700
		0.05	0.18	800
0048	100	0.43	0.43	20
		0.45	0.57	100
		0.55	0.89	200
		0.60	1.17	300
		0.68	1.56	400
		0.70	1.84	500

		0.81	2.41	600
		0.50	1.66	700
		0.04	0.15	800
0064	82	1.55	1.55	23
		1.62	2.04	100
		1.65	2.64	200
		1.68	3.26	300
		1.70	3.86	400
		1.92	5.01	500
		1.94	5.53	571.4
		1.92	5.51	576
		1.85	5.46	600
		1.67	5.24	657.4
		1.55	5.10	700
		1.10	3.99	800
0064	80	1.51	1.51	21.8
		1.55	1.97	100
		1.62	2.60	200
		1.68	3.26	300
		1.88	4.29	400
		2.19	5.74	500
		2.28	6.45	562
		2.28	6.75	600
		1.84	6.07	700
		1.02	3.71	800
0064	80	1.50	1.50	21.3
		1.54	1.96	100
		1.62	2.61	200
		1.65	3.22	300
		1.96	4.49	400
		2.21	5.81	500
		2.30	6.53	563
		2.26	6.71	600
		1.87	6.19	700
		1.08	3.94	800
0058	100	4.76	4.76	15.6
		4.90	6.32	100
		6.35	10.41	200

		8.28	16.48	300
		9.78	22.79	400
		10.64	28.52	500
		12.33	37.24	600
		11.21	32.15	700
		10.54	30.18	716
		5.83	24.80	800
0058	96	4.81	4.81	18.1
		4.96	6.35	100
		6.23	10.09	200
		7.51	14.79	300
		9.84	22.73	400
		10.78	28.67	500
		12.41	37.23	600
		11.22	32.28	700
		10.67	30.11	708
		5.23	24.22	800

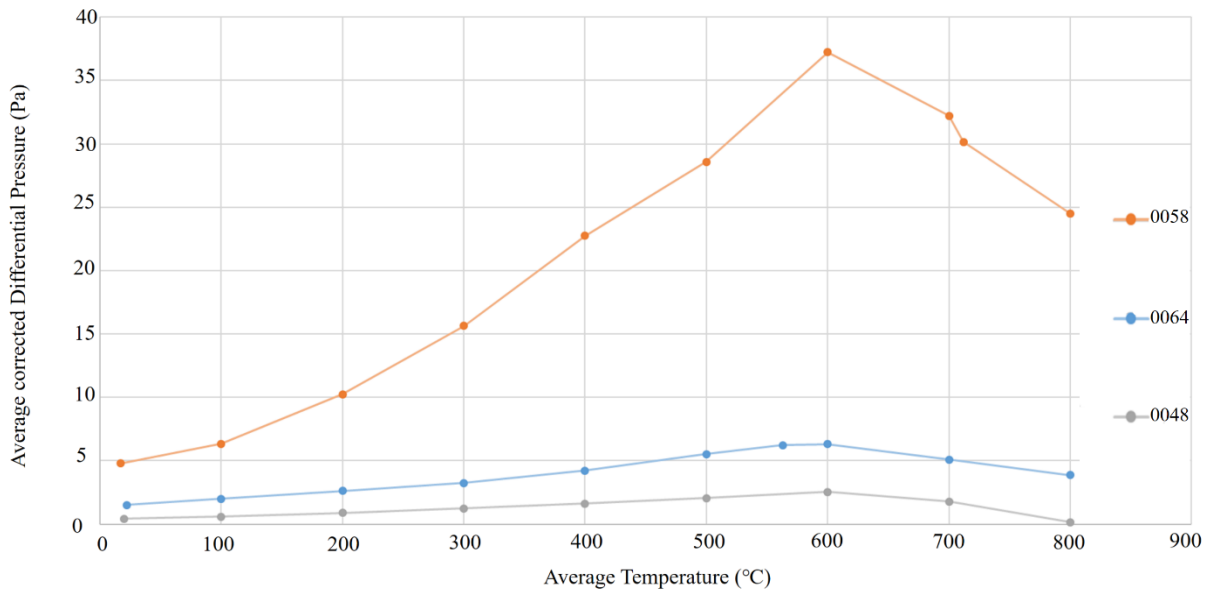

Figure 46. Corrected differential pressure variation for double samples of AES material.

5.2.3 Specific airflow resistance and airflow resistivity of double samples at specific temperatures

Since the differential pressure values were measured at room temperature, the pressure values were corrected based on the temperature ratio of high temperature to room temperature. The calculated and corrected values of specific airflow resistance and airflow resistivity (based on the initial thickness in the test rig at room temperature) are given in Table 50 for double samples of the three material densities (other measured data is in Appendix E).

Measurements were taken on two sets of double samples of material ID Nos. 0048, 0064 and 0058.

Table 50. Corrected specific airflow resistance and airflow resistivity values for double samples in the high temperature test rig with packing inside the preheater.

Material ID No.	Initial thickness at room temperature (mm)	Temperature (°C)	Specific airflow resistance (Pa.s/m)	Corrected specific airflow resistance (Pa.s/m)	Airflow resistivity (Pa.s/m^2)	Corrected airflow resistivity (Pa.s/m^2)
0048	100	20	859	859	8,586	8,586
		100	899	1,141	8,985	11,412
		200	1,103	1,776	11,029	17,757
		300	1,198	2,336	11,981	23,362
		400	1,358	3,109	13,578	31,094
		500	1,398	3,676	13,977	36,761
		600	1,617	4,804	16,174	48,036
		700	998	3,305	9,984	33,047
		800	80	291	799	2,907
0048	90	20	799	799	8,875	8,875
		100	938	1,192	10,428	13,243
		200	1,118	1,800	12,424	20,003
		300	1,358	2,648	15,087	29,419
		400	1,458	3,338	16,196	37,089
		500	1,717	4,516	19,080	50,181

		600	1,797	5,337	19,968	59,304
		700	1,158	3,845	12,868	42,722
		800	100	365	1,109	4,060
0064	82	20	3,095	3095	37,744	37,744
		100	3,249	4,093	39,616	49,916
		200	3,295	5,271	40,179	64,286
		300	3,369	6,536	41,084	79,702
		400	3,409	7,738	41,573	94,370
		500	3,850	10,049	46,953	122,546
		600	3,710	10,944	45,241	133,460
		700	3,095	10,183	37,744	124,177
		800	2,206	8007	26,900	97,647
0064	80	20	2,995	2,995	37,439	37,439
		100	3,075	3,905	38,438	48,816
		200	3,235	5,208	40,435	65,100
		300	3,295	6,425	41,183	80,308
		400	3,930	9,000	49,129	112,506
		500	4,451	11,705	55,632	146,313
		600	4,475	13,290	55,935	166,126
		700	3,734	12,359	46,675	154,493
		800	2,157	7,871	26,956	98,391
0064	80	20	3,015	3,015	37,689	37,689
		100	3,095	3,931	38,687	49,133
		200	3,235	5,176	40,435	64,695
		300	3,355	6,508	41,932	81,348
		400	3,754	8,559	46,924	106,987
		500	4,373	11,457	54,662	143,213
		600	4,572	13,533	57,150	169,164
		700	3,674	12,124	45,926	151,555
		800	2,037	7,414	25,459	92,670
0058	100	20	9,505	9,505	95,046	95,046
		100	9,784	12,622	97,842	126,216

		200	12,680	20,794	126,795	207,944
		300	16,394	32,625	163,943	326,247
		400	19,780	46,087	197,799	460,871
		500	21,336	57,181	213,361	571,806
		600	24,620	74,353	246,202	743,530
		700	24,484	82,512	244,843	825,122
		800	20,738	77,147	207,384	771,470
0058	96	20	9,604	9,604	100,047	100,047
		100	9,904	12,677	103,167	132,053
		200	12,493	20,238	130,134	210,816
		300	14,996	29,542	156,206	307,725
		400	19,732	45,581	205,540	474,797
		500	21,617	57,501	225,175	598,965
		600	24,780	74,340	258,124	774,373
		700	24,401	81,498	254,172	848,936
		800	20,467	75,523	213,197	786,697

5.2.4 Influence of temperature on the specific airflow resistance of double samples in high temperature test rig

Having established that the specific airflow resistance is the preferred parameter to assess the material properties over a wide range of temperatures, statistical tests were conducted to assess the effect of temperature on the corrected specific airflow resistance values.

For material ID No.0048 (64 kg/m^3), a one-way analysis of variance was conducted on the influence of temperature on the specific airflow resistance of double samples in high temperature test rig – see Table 51. Temperature variable included nine different temperatures {20℃, 100℃, 200℃, 300℃, 400℃, 500℃, 600℃, 700℃, 800℃}. All effects were statistically significant at the 0.05 significance level. The main effect for the temperature yielded an F ratio of F (8,9)=64.32 p=0.000 (p<0.05), indicating a significant difference between room temperature (M=829.0, SD=42.4), 100 ℃ (M=1166.5, SD=36.0), 200 ℃ (M=1788.0 SD=17.0), 300 ℃ (M=2492.0 SD=220.6), 400 ℃ (M=3,223.5 SD=161.9),

500 ℃(*M*=4,096.0, *SD*=594.0), 600 ℃ (*M*=5,070.5, *SD*=376.9), 700 ℃ (*M*=3,575.0, *SD*=381.8) and 800 ℃ (*M*=328.0, *SD*=52.3).

According to the results of ANOVA with Tukey's post-hoc test was conducted, the specific airflow resistance at room temperature (20 ℃) has a significant difference (p=0.05) to all other temperature values except 100 and 200 ℃.

The specific airflow resistance at 100℃ has a significant difference (p=0.05) to all other temperatures except 20 ℃ (room temperature) and 200 ℃.

The specific airflow resistances at 100, 200 and 300 ℃ are not significantly different (p=0.05), however they are significantly different to other temperatures.

The specific airflow resistance at 300 ℃ is not significantly different (p=0.05) from 200 and 700 ℃.

The specific airflow resistance at 400 ℃ is significantly different (p=0.05) from other temperatures except 300, 500 and 700 ℃.

The specific airflow resistance at 500 ℃ is significantly different (p=0.05) from other temperatures except 400, 700 and 800 ℃.

The specific airflow resistance at 600 ℃ is significantly different (p=0.05) from other temperatures except 500℃.

The specific airflow resistance at 700 ℃ is significantly different (p=0.05) from other temperatures except 300, 400 and 500 ℃.

The specific airflow resistance at 800 ℃ is significantly different (p=0.05) from all other temperatures except 20 ℃ (room temperature) and 100 ℃.

Table 51. Statistical test output for specific airflow resistance of double samples at high temperatures for material ID No.0048 (64 kg/m^3)

Specific airflow resistance (Pa.s/m)								
Temperature (°C)	N	Mean (Pa.s/m)	Std. Deviation (Pa.s/m)	Std. Error (Pa.s/m)	95% Confidence Interval for Mean (Pa.s/m)		Minimum (Pa.s/m)	Maximum (Pa.s/m)
					Lower Bound	Upper Bound		
20	2	829.0	42.4	30.0	447.8	1210.2	799	859
100	2	1166.5	36.1	25.5	842.5	1490.5	1141	1192
200	2	1788.0	17.0	12.0	1635.5	1940.5	1776	1800
300	2	2492.0	220.6	156.0	509.8	4474.2	2336	2648
400	2	3223.5	161.9	114.5	1768.6	4678.4	3109	3338
500	2	4096.0	594.00	420.0	-1240.6	9432.6	3676	4516
600	2	5070.5	376.9	266.5	1684.3	8456.7	4804	5337
700	2	3575.0	381.8	270.0	144.3	7005.7	3305	3845
800	2	328.0	52.3	37.0	-142.1	798.1	291	365
Total	18	2507.6	1571.4	370.3	1726.2	3289.	291	5337

ANOVA					
Specific airflow resistance (Pa.s/m)					
	Sum of Squares	df	Mean Square	F	Sig.
Between Groups	41256594.778	8	5157074.347	64.315	.000
Within Groups	721663.500	9	80184.833		
Total	41978258.278	17			

Multiple Comparisons						
Dependent Variable: Specific airflow resistance (Pa.s/m)						
Tukey HSD						
(I) Temperature (°C)	(J) Temperature (°C)	Mean Difference (I-J) (Pa.s/m)	Std. Error (Pa.s/m)	Sig.	95% Confidence Interval	
					Lower Bound	Upper Bound
20	100	-337.500	283.169	.940	-1457.73	782.73
	200	-959.000	283.169	.108	-2079.23	161.23
	300	-1663.000*	283.169	.004	-2783.23	-542.77
	400	-2394.500*	283.169	.000	-3514.73	-1274.27
	500	-3267.000*	283.169	.000	-4387.23	-2146.77
	600	-4241.500*	283.169	.000	-5361.73	-3121.27
	700	-2746.000*	283.169	.000	-3866.23	-1625.77
	800	501.000	283.169	.699	-619.23	1621.23
100	20	337.500	283.169	.940	-782.73	1457.73

	200	-621.500	283.169	.476	-1741.73	498.73
	300	-1325.500*	283.169	.019	-2445.73	-205.27
	400	-2057.000*	283.169	.001	-3177.23	-936.77
	500	-2929.500*	283.169	.000	-4049.73	-1809.27
	600	-3904.000*	283.169	.000	-5024.23	-2783.77
	700	-2408.500*	283.169	.000	-3528.73	-1288.27
	800	838.500	283.169	.191	-281.73	1958.73
200	20	959.000	283.169	.108	-161.23	2079.23
	100	621.500	283.169	.476	-498.73	1741.73
	300	-704.000	283.169	.344	-1824.23	416.23
	400	-1435.500*	283.169	.011	-2555.73	-315.27
	500	-2308.000*	283.169	.000	-3428.23	-1187.77
	600	-3282.500*	283.169	.000	-4402.73	-2162.27
	700	-1787.000*	283.169	.003	-2907.23	-666.77
	800	1460.000*	283.169	.010	339.77	2580.23
300	20	1663.000*	283.169	.004	542.77	2783.23
	100	1325.500*	283.169	.019	205.27	2445.73
	200	704.000	283.169	.344	-416.23	1824.23
	400	-731.500	283.169	.307	-1851.73	388.73
	500	-1604.000*	283.169	.005	-2724.23	-483.77
	600	-2578.500*	283.169	.000	-3698.73	-1458.27
	700	-1083.000	283.169	.060	-2203.23	37.23
	800	2164.000*	283.169	.001	1043.77	3284.23
400	20	2394.500*	283.169	.000	1274.27	3514.73
	100	2057.000*	283.169	.001	936.77	3177.23
	200	1435.500*	283.169	.011	315.27	2555.73
	300	731.500	283.169	.307	-388.73	1851.73
	500	-872.500	283.169	.163	-1992.73	247.73
	600	-1847.000*	283.169	.002	-2967.23	-726.77
	700	-351.500	283.169	.926	-1471.73	768.73
	800	2895.500*	283.169	.000	1775.27	4015.73
500	20	3267.000*	283.169	.000	2146.77	4387.23
	100	2929.500*	283.169	.000	1809.27	4049.73
	200	2308.000*	283.169	.000	1187.77	3428.23
	300	1604.000*	283.169	.005	483.77	2724.23
	400	872.500	283.169	.163	-247.73	1992.73
	600	-974.500	283.169	.101	-2094.73	145.73
	700	521.000	283.169	.662	-599.23	1641.23
	800	3768.000*	283.169	.000	2647.77	4888.23
600	20	4241.500*	283.169	.000	3121.27	5361.73
	100	3904.000*	283.169	.000	2783.77	5024.23
	200	3282.500*	283.169	.000	2162.27	4402.73
	300	2578.500*	283.169	.000	1458.27	3698.73

	400	1847.000*	283.169	.002	726.77	2967.23
	500	974.500	283.169	.101	-145.73	2094.73
	700	1495.500*	283.169	.009	375.27	2615.73
	800	4742.500*	283.169	.000	3622.27	5862.73
700	20	2746.000*	283.169	.000	1625.77	3866.23
	100	2408.500*	283.169	.000	1288.27	3528.73
	200	1787.000*	283.169	.003	666.77	2907.23
	300	1083.000	283.169	.060	-37.23	2203.23
	400	351.500	283.169	.926	-768.73	1471.73
	500	-521.000	283.169	.662	-1641.23	599.23
	600	-1495.500*	283.169	.009	-2615.73	-375.27
	800	3247.000*	283.169	.000	2126.77	4367.23
800	20	-501.000	283.169	.699	-1621.23	619.23
	100	-838.500	283.169	.191	-1958.73	281.73
	200	-1460.000*	283.169	.010	-2580.23	-339.77
	300	-2164.000*	283.169	.001	-3284.23	-1043.77
	400	-2895.500*	283.169	.000	-4015.73	-1775.27
	500	-3768.000*	283.169	.000	-4888.23	-2647.77
	600	-4742.500*	283.169	.000	-5862.73	-3622.27
	700	-3247.000*	283.169	.000	-4367.23	-2126.77
*. The mean difference is significant at the 0.05 level.						

For material ID No.0064 (96 kg/m^3), a one-way analysis of variance was conducted on the influence of temperature on the specific airflow resistance of double samples in high temperature test rig – see Table 52. A one-way analysis of variance was conducted on the influence of temperature on the specific airflow resistance of double samples in high temperature test rig. Temperature variable included nine different temperatures {20℃, 100℃, 200℃, 300℃, 400℃, 500℃, 600℃, 700℃, 800℃}. All effects were statistically significant at the 0.05 significance level. The main effect for the temperature yielded an *F* ratio of *F* (8,18) =66.07 *p*=0.000 (*p*<0.05), indicating a significant difference between room temperature (*M*= 3,035.0, *SD*=52.9), 100 ℃ (*M*=3,976.3, *SD*=101.9), 200℃ (*M*=5,218.3 *SD*=48.3), 300℃ (*M*= 6,489.7 *SD*=57.7), 400℃ (*M*=8,432.3 *SD*=640.5), 500℃(*M*=11,070.3, *SD*=893.2), 600℃ (*M*=12,589.0, *SD*=1429.8), 700℃(*M*=11,555.3, *SD*=1194.3) and 800℃ (*M*=7,764.0, *SD*=310.6).

According to the results of ANOVA with Tukey's post-hoc test, the specific airflow resistance at room temperature (20 ℃) has a significant difference (*p*=0.05) to all other temperature values except 100 and 200 ℃.

The specific airflow resistance at 100℃ has a significant difference (p=0.05) to all other temperatures except 20 ℃ (room temperature) and 200 ℃.

The specific airflow resistances at 100, 200 and 300 ℃ are not significantly different (p=0.05), however they are significantly different to other temperatures.

The specific airflow resistance at 300 ℃ is not significantly different (p=0.05) from 200,400 and 800 ℃.

The specific airflow resistance at 400 ℃ is significantly different (p=0.05) from other temperatures except 300 and 800 ℃.

The specific airflow resistance at 500 ℃ is significantly different (p=0.05) from other temperatures except 600 and 700 ℃.

The specific airflow resistance at 600 ℃ and 700℃ is only significantly different (p=0.05) from 500℃.

The specific airflow resistance at 600 ℃ is only non-significantly different (p=0.05) from 500 and 700 ℃.

The specific airflow resistance at 700 ℃ is significantly different (p=0.05) from other temperatures except 500 and 600 ℃.

The specific airflow resistance at 800 ℃ is significantly different (p=0.05) from all other temperatures except 300℃ and 400 ℃.

Table 52. Statistical test output for specific airflow resistance at high temperatures for material ID No.0064 (96 kg/m^3)

Specific airflow resistance (Pa.s/m)								
Temperature (°C)	N	Mean (Pa.s/m)	Std. Deviation (Pa.s/m)	Std. Error (Pa.s/m)	95% Confidence Interval for Mean (Pa.s/m)		Minimum (Pa.s/m)	Maximum (Pa.s/m)
					Lower Bound	Upper Bound		
20	3	3035.0	52.9	30.6	2903.5	3166.5	2995	3095
100	3	3976.3	101.7	58.8	3723.3	4229.4	3905	4093
200	3	5218.3	48.3	27.9	5098.3	5338.4	5176	5271
300	3	6489.7	57.7	33.3	6346.1	6633.1	6425	6536
400	3	8432.3	640.5	369.8	6841.3	10023.3	7738	9000
500	3	11070.3	893.2	515.7	8851.6	13289.0	10049	11705
600	3	12589.0	1429.8	825.5	9037.2	16140.8	10944	13533
700	3	11555.3	1194.3	689.5	8588.6	14522.1	10183	12359
800	3	7764.0	310.6	179.4	6992.3	8535.7	7414	8007
Total	27	7792.3	3346.1	644.0	6468.6	9115.9	2995	13533

ANOVA					
Specific airflow resistance (Pa.s/m)					
	Sum of Squares	df	Mean Square	F	Sig.
Between Groups	281521079.185	8	35190134.898	66.067	.000
Within Groups	9587636.000	18	532646.444		
Total	291108715.185	26			

Multiple Comparisons						
Dependent Variable: Specific airflow resistance (Pa.s/m)						
Tukey HSD						
(I) Temperature (°C)	(J) Temperature (°C)	Mean Difference (Pa.s/m) (I-J)	Std. Error (Pa.s/m)	Sig.	95% Confidence Interval	
					Lower Bound	Upper Bound
20	100	-941.333	595.901	.804	-3029.29	1146.62
	200	-2183.333*	595.901	.036	-4271.29	-95.38
	300	-3454.667*	595.901	.000	-5542.62	-1366.71
	400	-5397.333*	595.901	.000	-7485.29	-3309.38
	500	-8035.333*	595.901	.000	-10123.29	-5947.38
	600	-9554.000*	595.901	.000	-11641.95	-7466.05
	700	-8520.333*	595.901	.000	-10608.29	-6432.38
	800	-4729.000*	595.901	.000	-6816.95	-2641.05
100	20	941.333	595.901	.804	-1146.62	3029.29

	200	-1242.000	595.901	.512	-3329.95	845.95
	300	-2513.333*	595.901	.012	-4601.29	-425.38
	400	-4456.000*	595.901	.000	-6543.95	-2368.05
	500	-7094.000*	595.901	.000	-9181.95	-5006.05
	600	-8612.667*	595.901	.000	-10700.62	-6524.71
	700	-7579.000*	595.901	.000	-9666.95	-5491.05
	800	-3787.667*	595.901	.000	-5875.62	-1699.71
200	20	2183.333*	595.901	.036	95.38	4271.29
	100	1242.000	595.901	.512	-845.95	3329.95
	300	-1271.333	595.901	.483	-3359.29	816.62
	400	-3214.000*	595.901	.001	-5301.95	-1126.05
	500	-5852.000*	595.901	.000	-7939.95	-3764.05
	600	-7370.667*	595.901	.000	-9458.62	-5282.71
	700	-6337.000*	595.901	.000	-8424.95	-4249.05
	800	-2545.667*	595.901	.011	-4633.62	-457.71
300	20	3454.667*	595.901	.000	1366.71	5542.62
	100	2513.333*	595.901	.012	425.38	4601.29
	200	1271.333	595.901	.483	-816.62	3359.29
	400	-1942.667	595.901	.080	-4030.62	145.29
	500	-4580.667*	595.901	.000	-6668.62	-2492.71
	600	-6099.333*	595.901	.000	-8187.29	-4011.38
	700	-5065.667*	595.901	.000	-7153.62	-2977.71
	800	-1274.333	595.901	.480	-3362.29	813.62
400	20	5397.333*	595.901	.000	3309.38	7485.29
	100	4456.000*	595.901	.000	2368.05	6543.95
	200	3214.000*	595.901	.001	1126.05	5301.95
	300	1942.667	595.901	.080	-145.29	4030.62
	500	-2638.000*	595.901	.008	-4725.95	-550.05
	600	-4156.667*	595.901	.000	-6244.62	-2068.71
	700	-3123.000*	595.901	.001	-5210.95	-1035.05
	800	668.333	595.901	.963	-1419.62	2756.29
500	20	8035.333*	595.901	.000	5947.38	10123.29
	100	7094.000*	595.901	.000	5006.05	9181.95
	200	5852.000*	595.901	.000	3764.05	7939.95
	300	4580.667*	595.901	.000	2492.71	6668.62
	400	2638.000*	595.901	.008	550.05	4725.95
	600	-1518.667	595.901	.273	-3606.62	569.29
	700	-485.000	595.901	.995	-2572.95	1602.95
	800	3306.333*	595.901	.001	1218.38	5394.29
600	20	9554.000*	595.901	.000	7466.05	11641.95
	100	8612.667*	595.901	.000	6524.71	10700.62
	200	7370.667*	595.901	.000	5282.71	9458.62
	300	6099.333*	595.901	.000	4011.38	8187.29

	400	4156.667*	595.901	.000	2068.71	6244.62
	500	1518.667	595.901	.273	-569.29	3606.62
	700	1033.667	595.901	.720	-1054.29	3121.62
	800	4825.000*	595.901	.000	2737.05	6912.95
700	20	8520.333*	595.901	.000	6432.38	10608.29
	100	7579.000*	595.901	.000	5491.05	9666.95
	200	6337.000*	595.901	.000	4249.05	8424.95
	300	5065.667*	595.901	.000	2977.71	7153.62
	400	3123.000*	595.901	.001	1035.05	5210.95
	500	485.000	595.901	.995	-1602.95	2572.95
	600	-1033.667	595.901	.720	-3121.62	1054.29
	800	3791.333*	595.901	.000	1703.38	5879.29
800	20	4729.000*	595.901	.000	2641.05	6816.95
	100	3787.667*	595.901	.000	1699.71	5875.62
	200	2545.667*	595.901	.011	457.71	4633.62
	300	1274.333	595.901	.480	-813.62	3362.29
	400	-668.333	595.901	.963	-2756.29	1419.62
	500	-3306.333*	595.901	.001	-5394.29	-1218.38
	600	-4825.000*	595.901	.000	-6912.95	-2737.05
	700	-3791.333*	595.901	.000	-5879.29	-1703.38
*. The mean difference is significant at the 0.05 level.						

For material ID No.0058 (128 kg/m^3), a one-way analysis of variance was conducted on the influence of temperature on the specific airflow resistance of double samples in high temperature test rig – see Table 53. A one-way analysis of variance was conducted on the influence of temperature on the specific airflow resistance of double samples in high temperature test rig. Temperature variable included nine different temperatures {20 ℃, 100 ℃, 200 ℃, 300 ℃, 400 ℃, 500 ℃, 600 ℃, 700 ℃, 800 ℃}. All effects were statistically significant at the 0.05 significance level. The main effect for the temperature yielded an *F* ratio of *F* (8,9) =2,098.48 *p*=0.000 (*p*<0.05), indicating a significant difference between room temperature (*M*= 9,554.5, *SD*=70.0), 100 ℃ (*M*=12,649.5, *SD*=38.9), 200 ℃ (*M*=20,516.0 *SD*=393.2), 300 ℃ (*M*= 31,083.5 *SD*=2,180.0), 400 ℃(*M*=45,834.0 *SD*=357.8), 500 ℃(*M*= 57,341.0, *SD*=226.3), 600 ℃ (*M*=74,346.5 , *SD*=9.2), 700 ℃(*M*=82,005.0, *SD*=717.0) and 800℃ (*M*=76,335.0, *SD*=1148.3),

According to the results of ANOVA with Tukey's post –hoc test, the specific airflow resistance at room temperature (20 ℃) has a significant difference (*p*=0.05) to all other temperature values except 100 ℃.

The specific airflow resistance at 600 ℃ is statistically non-significant to the value at 800 ℃.

Considering the results from the three densities, it might be possible to assume no significant effect of temperature on specific airflow resistance for 20 and 100 ℃. Whilst there was not always a significant difference between results in 100 ℃ steps, this choice was reasonable although the change in material properties above 600 ℃ means that future work could use smaller temperature steps to assess changes in airflow resistance as the material crystallises.

Table 53. Statistical test output for specific airflow resistance at high temperatures for material ID No.0058 (128 kg/m^3)

Specific airflow resistance (Pa.s/m)								
Temperature (℃)	N	Mean (Pa.s/m)	Std. Deviation (Pa.s/m)	Std. Error (Pa.s/m)	95% Confidence Interval for Mean (Pa.s/m)		Minimum (Pa.s/m)	Maximum (Pa.s/m)
					Lower Bound	Upper Bound		
20	2	9554.5	70.0	49.5	8925.5	10183.5	9505	9604
100	2	12649.5	38.9	27.5	12300.1	12998.9	12622	12677
200	2	20516.0	393.2	278.0	16983.7	24048.3	20238	20794
300	2	31083.5	2180.0	1541.5	11496.9	50670.1	29542	32625
400	2	45834.0	357.8	253.0	42619.3	49048.6	45581	46087
500	2	57341.0	226.3	160.0	55308.0	59374.0	57181	57501
600	2	74346.5	9.2	6.5	74263.9	74429.1	74340	74353
700	2	82005.0	717.0	507.0	75563.0	88447.1	81498	82512
800	2	76335.0	1148.3	812.0	66017.6	86652.4	75523	77147
Total	18	45518.3	27573.6	6499.2	31806.3	59230.4	9505	82512

ANOVA					
Specific airflow resistance (Pa.s/m)					
	Sum of Squares	df	Mean Square	F	Sig.
Between Groups	12918241346.000	8	1614780168.250	2098.476	.000
Within Groups	6925514.000	9	769501.556		
Total	12925166860.000	17			

Multiple Comparisons						
Dependent Variable: Specific airflow resistance (Pa.s/m)						
Tukey HSD						
(I) Temperature (℃)	(J) Temperature (℃)	Mean Difference (I-J) (Pa.s/m)	Std. Error (Pa.s/m)	Sig.	95% Confidence Interval (Pa.s/m)	
					Lower Bound	Upper Bound
20	100	-3095.000	877.212	.089	-6565.30	375.30
	200	-10961.500*	877.212	.000	-14431.80	-7491.20
	300	-21529.000*	877.212	.000	-24999.30	-18058.70
	400	-36279.500*	877.212	.000	-39749.80	-32809.20
	500	-47786.500*	877.212	.000	-51256.80	-44316.20
	600	-64792.000*	877.212	.000	-68262.30	-61321.70
	700	-72450.500*	877.212	.000	-75920.80	-68980.20
	800	-66780.500*	877.212	.000	-70250.80	-63310.20
100	20	3095.000	877.212	.089	-375.30	6565.30
	200	-7866.500*	877.212	.000	-11336.80	-4396.20
	300	-18434.000*	877.212	.000	-21904.30	-14963.70
	400	-33184.500*	877.212	.000	-36654.80	-29714.20
	500	-44691.500*	877.212	.000	-48161.80	-41221.20
	600	-61697.000*	877.212	.000	-65167.30	-58226.70
	700	-69355.500*	877.212	.000	-72825.80	-65885.20
	800	-63685.500*	877.212	.000	-67155.80	-60215.20
200	20	10961.500*	877.212	.000	7491.20	14431.80
	100	7866.500*	877.212	.000	4396.20	11336.80
	300	-10567.500*	877.212	.000	-14037.80	-7097.20
	400	-25318.000*	877.212	.000	-28788.30	-21847.70
	500	-36825.000*	877.212	.000	-40295.30	-33354.70
	600	-53830.500*	877.212	.000	-57300.80	-50360.20
	700	-61489.000*	877.212	.000	-64959.30	-58018.70
	800	-55819.000*	877.212	.000	-59289.30	-52348.70
300	20	21529.000*	877.212	.000	18058.70	24999.30
	100	18434.000*	877.212	.000	14963.70	21904.30
	200	10567.500*	877.212	.000	7097.20	14037.80
	400	-14750.500*	877.212	.000	-18220.80	-11280.20
	500	-26257.500*	877.212	.000	-29727.80	-22787.20
	600	-43263.000*	877.212	.000	-46733.30	-39792.70
	700	-50921.500*	877.212	.000	-54391.80	-47451.20
	800	-45251.500*	877.212	.000	-48721.80	-41781.20
400	20	36279.500*	877.212	.000	32809.20	39749.80
	100	33184.500*	877.212	.000	29714.20	36654.80
	200	25318.000*	877.212	.000	21847.70	28788.30
	300	14750.500*	877.212	.000	11280.20	18220.80
	500	-11507.000*	877.212	.000	-14977.30	-8036.70

	600	-28512.500*	877.212	.000	-31982.80	-25042.20
	700	-36171.000*	877.212	.000	-39641.30	-32700.70
	800	-30501.000*	877.212	.000	-33971.30	-27030.70
500	20	47786.500*	877.212	.000	44316.20	51256.80
	100	44691.500*	877.212	.000	41221.20	48161.80
	200	36825.000*	877.212	.000	33354.70	40295.30
	300	26257.500*	877.212	.000	22787.20	29727.80
	400	11507.000*	877.212	.000	8036.70	14977.30
	600	-17005.500*	877.212	.000	-20475.80	-13535.20
	700	-24664.000*	877.212	.000	-28134.30	-21193.70
	800	-18994.000*	877.212	.000	-22464.30	-15523.70
600	20	64792.000*	877.212	.000	61321.70	68262.30
	100	61697.000*	877.212	.000	58226.70	65167.30
	200	53830.500*	877.212	.000	50360.20	57300.80
	300	43263.000*	877.212	.000	39792.70	46733.30
	400	28512.500*	877.212	.000	25042.20	31982.80
	500	17005.500*	877.212	.000	13535.20	20475.80
	700	-7658.500*	877.212	.000	-11128.80	-4188.20
	800	-1988.500	877.212	.441	-5458.80	1481.80
700	20	72450.500*	877.212	.000	68980.20	75920.80
	100	69355.500*	877.212	.000	65885.20	72825.80
	200	61489.000*	877.212	.000	58018.70	64959.30
	300	50921.500*	877.212	.000	47451.20	54391.80
	400	36171.000*	877.212	.000	32700.70	39641.30
	500	24664.000*	877.212	.000	21193.70	28134.30
	600	7658.500*	877.212	.000	4188.20	11128.80
	800	5670.000*	877.212	.002	2199.70	9140.30
800	20	66780.500*	877.212	.000	63310.20	70250.80
	100	63685.500*	877.212	.000	60215.20	67155.80
	200	55819.000*	877.212	.000	52348.70	59289.30
	300	45251.500*	877.212	.000	41781.20	48721.80
	400	30501.000*	877.212	.000	27030.70	33971.30
	500	18994.000*	877.212	.000	15523.70	22464.30
	600	1988.500	877.212	.441	-1481.80	5458.80
	700	-5670.000*	877.212	.002	-9140.30	-2199.70

*. The mean difference is significant at the 0.05 level.

In conclusion, by considering all the statistical test results, it is shown that the effect of temperature on the specific airflow resistance is statistically significant and that the effect of temperature was highest with material ID No.0058 which has the highest nominal density (i.e. manufacturers quoted density at room temperature).

5.2.5 Effect of airflow velocity on double samples

Specific airflow resistance measurements were carried out for four different airflow velocities corresponding to the sound pressure levels indicated in Table 1 and the results are shown in Table 54 and Figure 47.

Table 54. Specific airflow resistance values for different airflow velocities.

Mass (g)	Specific airflow resistance values for different airflow velocities (Pa.s/m)			
	0.5×10^{-3} m/s	1×10^{-3} m/s	2×10^{-3} m/s	4×10^{-3} m/s
22.12	365	4032	9010	17312
24.21	291	3972	8759	17052
29.57	7871	16438	23517	33187
30.86	7414	15478	23162	32759
30.87	8007	16268	23227	33178
47.61	77147	53777	48144	30047
48.32	75523	48545	48399	27942

In contrast to the room temperature measurements in section 5.1.5 where the effect of different airflow velocities was negligible, Figure 47 shows that the specific airflow resistance at 800℃ vary with the different airflow velocities. For the highest density samples there is little change in the specific airflow resistance for the range of airflow velocities. However, with increasing airflow velocity the change in specific airflow resistance with increasing sample mass becomes less significant such that the specific airflow resistance becomes almost independent from the sample mass at the highest airflow velocity of 4×10^{-3} m/s .

In this project the main comparisons between the two test rigs are all carried out with an airflow velocity of 0.5×10^{-3} m/s; however, the findings here suggest that the airflow velocity should be chosen to correspond to the SPL in the specific application.

Table 55. Statistical comparison of specific airflow resistance at 800℃ for four different airflow velocities

Dependent variable : Specific airflow resistance (Pa.s/m)				
Mass (kg)	Velocities (m/s)	Mean (Pa.s/m)	Std. Deviation (Pa.s/m)	N
22.12	0.5×10^{-3}	365.00	.	1
	1×10^{-3}	4032.00	.	1
	2×10^{-3}	9010.00	.	1

	4×10^{-3}	17312.00	.	1
	Total	7679.75	7333.972	4
24.21	0.5×10^{-3}	291.00	.	1
	1×10^{-3}	3972.00	.	1
	2×10^{-3}	8759.00	.	1
	4×10^{-3}	17052.00	.	1
	Total	7518.50	7239.726	4
29.57	0.5×10^{-3}	7871.00	.	1
	1×10^{-3}	16438.00	.	1
	2×10^{-3}	23517.00	.	1
	4×10^{-3}	33187.00	.	1
	Total	20253.25	10736.390	4
30.86	0.5×10^{-3}	7414.00	.	1
	1×10^{-3}	15478.00	.	1
	2×10^{-3}	23162.00	.	1
	4×10^{-3}	32759.00	.	1
	Total	19703.25	10821.182	4
30.87	0.5×10^{-3}	8007.00	.	1
	1×10^{-3}	16268.00	.	1
	2×10^{-3}	23227.00	.	1
	4×10^{-3}	33178.00	.	1
	Total	20170.00	10672.667	4
47.61	0.5×10^{-3}	77147.00	.	1
	1×10^{-3}	53777.00	.	1
	2×10^{-3}	48144.00	.	1
	4×10^{-3}	30047.00	.	1
	Total	52278.75	19425.254	4
48.32	0.5×10^{-3}	75523.00	.	1
	1×10^{-3}	48545.00	.	1
	2×10^{-3}	48399.00	.	1
	4×10^{-3}	27942.00	.	1
	Total	50102.25	19515.953	4
Total	0.5×10^{-3}	25231.14	35072.209	7
	1×10^{-3}	22644.29	20271.881	7
	2×10^{-3}	26316.86	16325.800	7
	4×10^{-3}	27353.86	7207.957	7
	Total	25386.54	20943.426	28

Tests of Between-Subjects Effects					
Dependent variable: Specific airflow resistance (Pa.s/m)					
Source	Type III Sum of Squares	df	Mean Square	F	Sig.
Corrected Model	8296828679.179[a]	9	921869853.242	4.679	.003
Intercept	18045333476.036	1	18045333476.036	91.598	.000
Mass	8210869144.214	6	1368478190.702	6.946	.001
Velocities	85959534.964	3	28653178.321	.145	.931
Error	3546103223.786	18	197005734.655		
Total	29888265379.000	28			
Corrected Total	11842931902.964	27			
a. R Squared = .701 (Adjusted R Squared = .551)					

Multiple Comparisons- Mass						
Dependent variable: Specific airflow resistance (Pa.s/m)						
Tukey HSD						
(I) Mass (kg)	(J) Mass (kg)	Mean Difference (I-J) (Pa.s/m)	Std. Error (Pa.s/m)	Sig.	95% Confidence Interval	
					Lower Bound	Upper Bound
22.12	24.21	161.25	9924.861	1.000	-32634.49	32956.99
	29.57	-12573.50	9924.861	.858	-45369.24	20222.24
	30.86	-12023.50	9924.861	.881	-44819.24	20772.24
	30.87	-12490.25	9924.861	.862	-45285.99	20305.49
	47.61	-44599.00*	9924.861	.004	-77394.74	-11803.26
	48.32	-42422.50*	9924.861	.007	-75218.24	-9626.76
24.21	22.12	-161.25	9924.861	1.000	-32956.99	32634.49
	29.57	-12734.75	9924.861	.851	-45530.49	20060.99
	30.86	-12184.75	9924.861	.874	-44980.49	20610.99
	30.87	-12651.50	9924.861	.855	-45447.24	20144.24
	47.61	-44760.25*	9924.861	.004	-77555.99	-11964.51
	48.32	-42583.75*	9924.861	.007	-75379.49	-9788.01
29.57	22.12	12573.50	9924.861	.858	-20222.24	45369.24
	24.21	12734.75	9924.861	.851	-20060.99	45530.49
	30.86	550.00	9924.861	1.000	-32245.74	33345.74
	30.87	83.25	9924.861	1.000	-32712.49	32878.99
	47.61	-32025.50	9924.861	.058	-64821.24	770.24
	48.32	-29849.00	9924.861	.089	-62644.74	2946.74
30.86	22.12	12023.50	9924.861	.881	-20772.24	44819.24
	24.21	12184.75	9924.861	.874	-20610.99	44980.49
	29.57	-550.00	9924.861	1.000	-33345.74	32245.74
	30.87	-466.75	9924.861	1.000	-33262.49	32328.99
	47.61	-32575.50	9924.861	.052	-65371.24	220.24

	48.32	-30399.00	9924.861	.080	-63194.74	2396.74
30.87	22.12	12490.25	9924.861	.862	-20305.49	45285.99
	24.21	12651.50	9924.861	.855	-20144.24	45447.24
	29.57	-83.25	9924.861	1.000	-32878.99	32712.49
	30.86	466.75	9924.861	1.000	-32328.99	33262.49
	47.61	-32108.75	9924.861	.057	-64904.49	686.99
	48.32	-29932.25	9924.861	.087	-62727.99	2863.49
47.61	22.12	44599.00*	9924.861	.004	11803.26	77394.74
	24.21	44760.25*	9924.861	.004	11964.51	77555.99
	29.57	32025.50	9924.861	.058	-770.24	64821.24
	30.86	32575.50	9924.861	.052	-220.24	65371.24
	30.87	32108.75	9924.861	.057	-686.99	64904.49
	48.32	2176.50	9924.861	1.000	-30619.24	34972.24
48.32	22.12	42422.50*	9924.861	.007	9626.76	75218.24
	24.21	42583.75*	9924.861	.007	9788.01	75379.49
	29.57	29849.00	9924.861	.089	-2946.74	62644.74
	30.86	30399.00	9924.861	.080	-2396.74	63194.74
	30.87	29932.25	9924.861	.087	-2863.49	62727.99
	47.61	-2176.50	9924.861	1.000	-34972.24	30619.24

Based on observed means.

The error term is Mean Square (Error) = 197005734.655.

*. The mean difference is significant at the .05 level.

Multiple Comparisons -Velocities

Dependent variable: Specific airflow resistance (Pa.s/m)

Tukey HSD

(I) Velocities (m/s)	(J) Velocities (m/s)	Mean Difference (I-J) (Pa.s/m)	Std. Error (Pa.s/m)	Sig.	95% Confidence Interval	
					Lower Bound	Upper Bound
0.5×10^{-3}	1×10^{-3}	2586.86	7502.490	.985	-18617.36	23791.07
	2×10^{-3}	-1085.71	7502.490	.999	-22289.93	20118.50
	4×10^{-3}	-2122.71	7502.490	.992	-23326.93	19081.50
1×10^{-3}	0.5×10^{-3}	-2586.86	7502.490	.985	-23791.07	18617.36
	2×10^{-3}	-3672.57	7502.490	.960	-24876.78	17531.64
	4×10^{-3}	-4709.57	7502.490	.922	-25913.78	16494.64
2×10^{-3}	0.5×10^{-3}	1085.71	7502.490	.999	-20118.50	22289.93
	1×10^{-3}	3672.57	7502.490	.960	-17531.64	24876.78
	4×10^{-3}	-1037.00	7502.490	.999	-22241.21	20167.21
4×10^{-3}	0.5×10^{-3}	2122.71	7502.490	.992	-19081.50	23326.93
	1×10^{-3}	4709.57	7502.490	.922	-16494.64	25913.78
	2×10^{-3}	1037.00	7502.490	.999	-20167.21	22241.21

Based on observed means.

The error term is Mean Square (Error) = 197005734.655.

Interaction effect : Mass * Velocities

Dependent variable: Specific airflow resistance (Pa.s/m)

Mass (kg)	Velocities (m/s)	Mean (Pa.s/m)	Std. Error (Pa.s/m)	95% Confidence Interval	
				Lower Bound (Pa.s/m)	Upper Bound (Pa.s/m)
22.12	0.5×10^{-3}	7524.357	8388.039	-10098.258	25146.972
	1×10^{-3}	4937.500	8388.039	-12685.115	22560.115
	2×10^{-3}	8610.071	8388.039	-9012.544	26232.687
	4×10^{-3}	9647.071	8388.039	-7975.544	27269.687
24.21	0.5×10^{-3}	7363.107	8388.039	-10259.508	24985.722
	1×10^{-3}	4776.250	8388.039	-12846.365	22398.865
	2×10^{-3}	8448.821	8388.039	-9173.794	26071.437
	4×10^{-3}	9485.821	8388.039	-8136.794	27108.437
29.57	0.5×10^{-3}	20097.857	8388.039	2475.242	37720.472
	1×10^{-3}	17511.000	8388.039	-111.615	35133.615
	2×10^{-3}	21183.571	8388.039	3560.956	38806.187
	4×10^{-3}	22220.571	8388.039	4597.956	39843.187
30.86	0.5×10^{-3}	19547.857	8388.039	1925.242	37170.472
	1×10^{-3}	16961.000	8388.039	-661.615	34583.615
	2×10^{-3}	20633.571	8388.039	3010.956	38256.187
	4×10^{-3}	21670.571	8388.039	4047.956	39293.187
30.87	0.5×10^{-3}	20014.607	8388.039	2391.992	37637.222
	1×10^{-3}	17427.750	8388.039	-194.865	35050.365
	2×10^{-3}	21100.321	8388.039	3477.706	38722.937
	4×10^{-3}	22137.321	8388.039	4514.706	39759.937
47.61	0.5×10^{-3}	52123.357	8388.039	34500.742	69745.972
	1×10^{-3}	49536.500	8388.039	31913.885	67159.115
	2×10^{-3}	53209.071	8388.039	35586.456	70831.687
	4×10^{-3}	54246.071	8388.039	36623.456	71868.687
48.32	0.5×10^{-3}	49946.857	8388.039	32324.242	67569.472
	1×10^{-3}	47360.000	8388.039	29737.385	64982.615
	2×10^{-3}	51032.571	8388.039	33409.956	68655.187
	4×10^{-3}	52069.571	8388.039	34446.956	69692.187

Two-way analysis of variance (Two way ANOVA) was conducted on the effect of sample mass and the airflow velocities on specific airflow resistance – see Table 55. There was a statistical significant difference between the specific airflow resistance and the sample mass. *F* (6, 28)

=6.946 p=0.001 (p<0.05). However, there was a non-significance difference on the specific airflow resistance and airflow velocities. F (3, 28) =0.145 p=0.931 (p>0.05).

According to the results of Two way ANOVA with Tukey's post-hoc test was conducted, The specific airflow resistance of both 47.61 and 48.32 kg samples have a significant difference (p=0.05) to all other samples. However there is no significance difference in the specific airflow resistance between the sets of lower mass values and the medium mass values.

Furthermore, there is no significance difference in the specific airflow resistance between individual airflow velocities for different sample mass values.

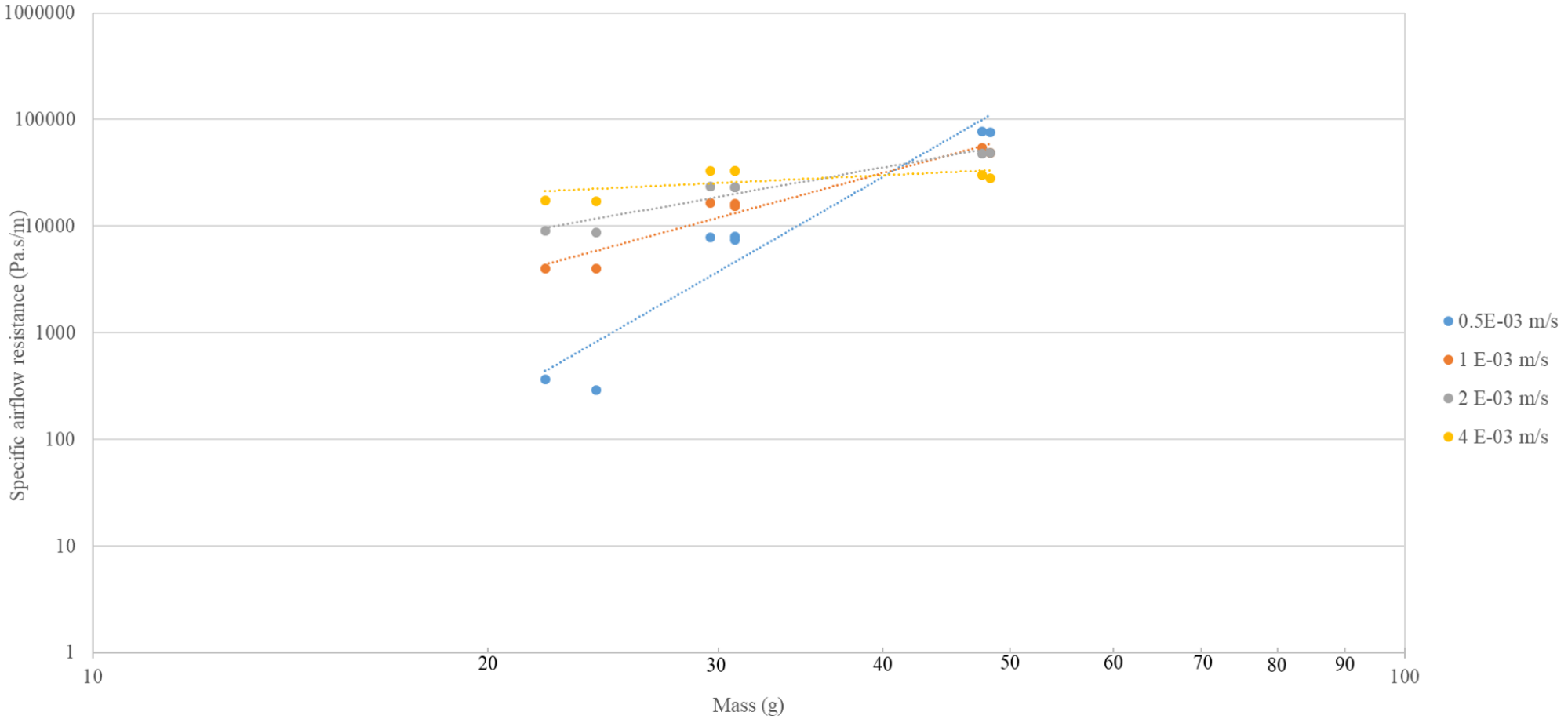

Figure 47. Specific airflow resistance at 800 ℃ for four different airflow velocities.

5.2.6 Regression analysis to relate specific airflow resistance to sample mass for different density materials

Section 5.2.4 confirmed that the specific airflow resistance varies with temperature. The final stage is to use regression analysis to identify a relationship between specific airflow resistance and temperature for each material ID. Referring back to room temperature measurements in section 5.1.4 it was feasible to use an independent variable of bulk density. However, over the temperature range from 20 to 800 °C, the thickness of the double sample significantly reduces above 600 °C. This means that the density of the sample is no longer known across the full range of temperatures. For this reason, another approach has been taken to identify an empirical relationship; this is to use the mass, *m*, of each double sample at temperature, *T*. For the double samples the straight-line regression coefficients are shown in Table 56. These regression lines are plotted along with the individual data points in Figure 48.

Table 56. Regression lines for each individual temperature

Temperature (°C)	No of Samples	Gradient	Intercept	Coefficient of determination, R^2	Standard error
20	7	3.2198	-1.3846	0.953	0.102
100	7	3.1412	-1.1387	0.956	0.097
200	7	3.2684	-1.1666	0.982	0.063
300	7	3.4142	-1.2532	0.982	0.067
400	7	3.6049	-1.4114	0.981	0.071
500	7	3.5683	-1.2488	0.973	0.085
600	7	3.6643	-1.3108	0.976	0.082
700	7	4.2415	-2.2268	0.978	0.091
800	7	7.0712	-6.8665	0.914	0.312

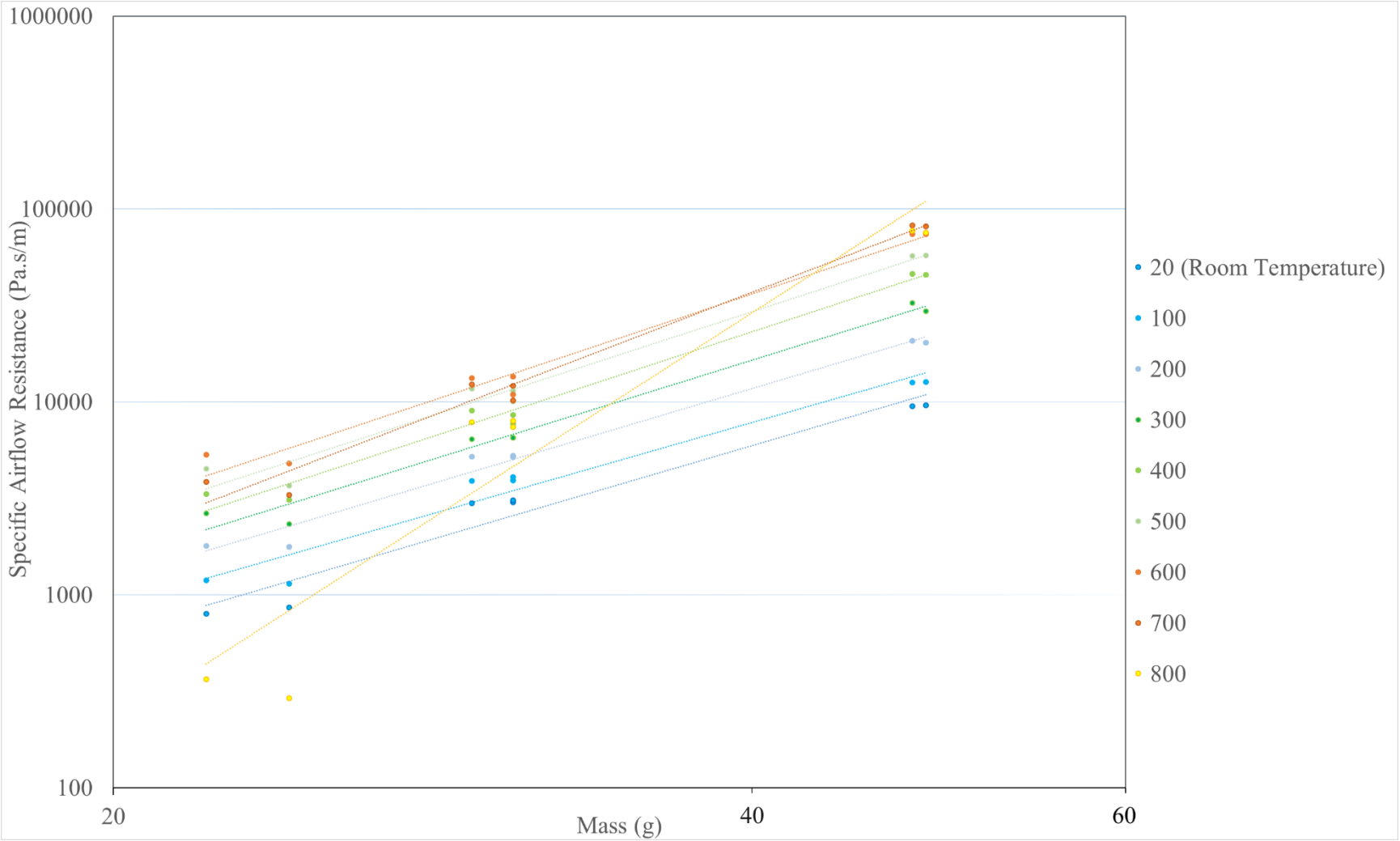

Figure 48. Relationship between specific airflow resistance and mass of the double samples at temperatures between 20 and 800 °C.

To identify a single regression equation that is valid for all temperatures between 20 and 800 °C, multiple regression analysis was conducted using the nine regression lines together a single equation that applies to all nine temperatures and the results are as follows:

Dependent variable: $\log_{10}(R_s)$
Independent variable: $\log_{10}(m)$
Conditional variable: T

Table 57. Relationship between airflow resistivity and mass of the double samples at temperatures between 20 and 800 °C: Multiple regression analysis.

Parameter	Estimated values	Standard error	T statistic	*p* value
Constant	-1.385	0.605	-2.288	0.027
$\log_{10}(m)$	3.220	0.401	8.038	0.000
T =1	0.229	0.812	0.283	0.779
T =2	0.218	0.856	0.255	0.800
T =3	0.131	0.856	0.154	0.879
T =4	-0.027	0.856	-0.031	0.975
T =5	0.136	0.856	0.159	0.875
T =6	0.074	0.856	0.086	0.932
T =7	-0.842	0.856	-0.984	0.330
T =8	-5.482	0.856	-6.406	0.000
$\log_{10}(m)$* T =1	-0.068	0.541	-0.126	0.900
$\log_{10}(m)$* T =2	0.449	0.566	0.086	0.932
$\log_{10}(m)$* T =3	0.194	0.566	0.343	0.733
$\log_{10}(m)$*T=4	0.385	0.566	0.680	0.500
$\log_{10}(m)$* T=5	0.349	0.566	0.615	0.541
$\log_{10}(m)$* T=6	0.445	0.566	0.785	0.437
$\log_{10}(m)$* T=7	1.022	0.566	1.804	0.078
$\log_{10}(m)$* T=8	3.851	0.566	6.799	0.000

Table 58. Relationship between airflow resistivity and mass of the double samples at temperatures between 20 and 800 °C: ANOVA for variables in the order fitted.

Source	Sum of squares	Degrees of freedom	Mean square	F-ratio	*p* value
$\log_{10}(m)$	14.918	1	14.918	894.63	0.0000
Intercepts	3.837	8	0.480	28.76	0.0000
Slopes	1.268	8	0.159	9.51	0.0000
Model	20.024	17			

Multiple linear regression was calculated to predict $\log_{10}$ (R_S) based on mass and temperature. A significant regression equation was found with an R^2 of 0.963. The equation of the fitted model is as follows.

$$\log_{10}(R_s) = -1.385 + 3.220*\log_{10}(m) + 0.229*(T=1) +0.218*(T=2) +0.131*(T=3)-0.027*(T=4)+ 0.136*(T=5)+0.074*(T=6) - 0.842*(T=7) – 5.482*(T=8) -0.0683*\log_{10}(m)*(T=1)+ 0.049*\log_{10}(m)*(T=2) +0.194*\log_{10}(m)*(T=3) +0.385*\log_{10}(m)*(T=4) +0.349*\log_{10}(m)*(T=6)+ 1.022*\log_{10}(m)*(T=7) +3.851*\log_{10}(m)*(T=8) \quad (74)$$

where "*T*" is coded as 0= "Room temperature (20℃)", 1=100℃, 2=200℃, 3=300℃, 4=400℃, 5=500℃, 6=600℃, 7= 700℃ and 8= 800℃. The term $T=n$ (where, n=1, 2, 3, 4…..7, 8) is an indicator variable which takes the value 1 if it is 100℃ etc. This corresponds to 9 separate lines, one for each value of temperature. Nine linear regression models for $\log_{10}$ (R_s) were subjected to one way analysis of variance by considering intercepts (F (8, 17) =27.92, p<0.05) and gradients (F (8, 17) =27.92, p<0.05). There is a statistically significant difference (p=0.05) among intercepts and gradients for each temperature.

Up to 700 ℃, the specific airflow resistance is proportional to the temperature as well as the mass of the sample. However, there is a significant change of specific airflow resistance at 800 ℃ for the 64 and 96 kg/m^3 materials, although the specific airflow resistance remains proportional to the sample mass.

5.2.7 Regression analysis to identify the power law relationship between specific airflow resistance and temperature for different density materials

The final stage is to identify the power law relationship between specific airflow resistance and temperature using regression analysis as discussed in section 3.3. Previous results discussed in this chapter indicate that the material changed significantly above 600 °C; hence the regression analysis was only carried out from room temperature up to 600 °C. The results are shown in Table 59 and plotted in Figure 49 to Figure 55. Power law regression gives a close fit to the measured data as indicated by the coefficient of determination R^2>0.99. However, the values of the exponents are larger than those published in the literature that were reviewed in section 3.3. The average exponent for the three material densities is 1.6 and individual exponents vary between 1.17 and 1.96. These exponent values are larger than the value of 0.7 that would have been expected from Sutherland's equation [64] and the value of 0.6 found by Christie [34] for rock wool at temperatures up to 400 °C. However, Miglietta et al [65] did determine an exponent value of 1.2 from a variety of different materials at temperatures between 0 and 30 °C, which indicates that exponents >0.7 can occur even at relatively low temperatures. As there is no reason to doubt the exponent values for the AES materials tested in this project it would be worthwhile testing different materials in future projects to see whether the average value of 1.60 is unusual.

Table 59. Exponents for the absolute temperature from power law regression for individual samples.

Material ID No.	Exponent for the power law	Coefficient of determination, R^2
0048A	1.5807	0.9965
0048B	1.7653	0.9988
0064A	1.1685	0.9953
0064B	1.4016	0.9867
0064C	1.3857	0.9866
0058A	1.9568	0.9934
0058B	1.9454	0.9907
Average	1.6006	-

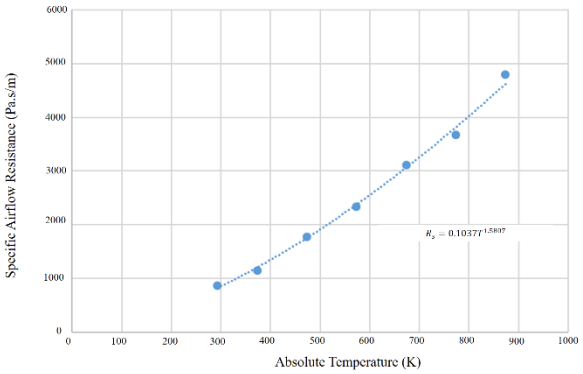

Figure 49. Power law relationship for Material ID No.0048A

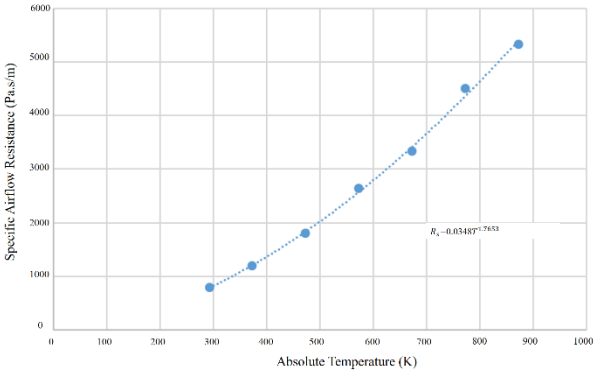

Figure 50. Power law relationship for Material ID No.0048B

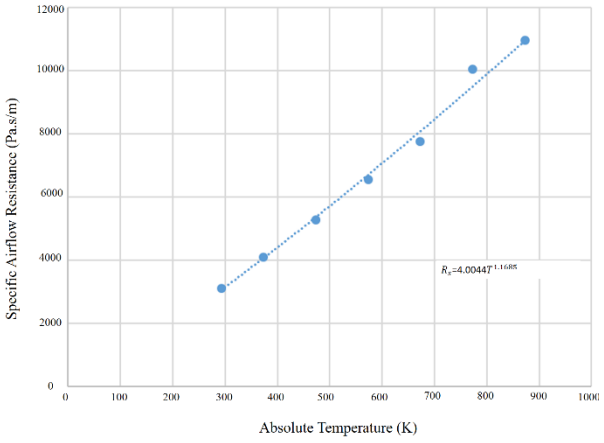

Figure 51. Power law relationship for Material ID No.0064A

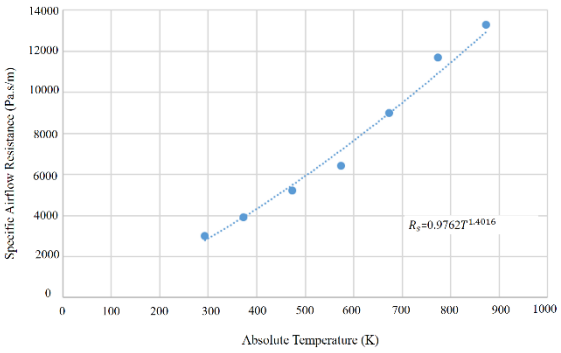

Figure 52. Power law relationship for Material ID No.0064B

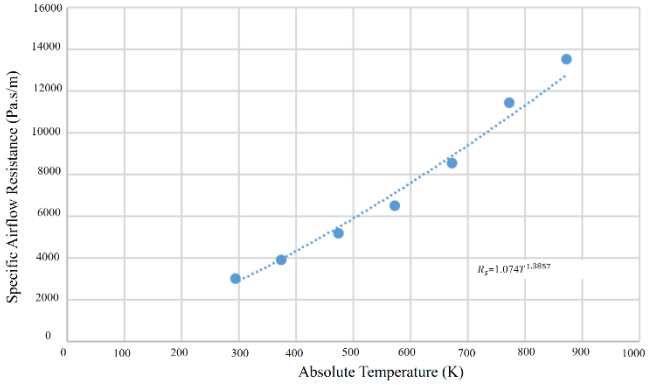

Figure 53. Power law relationship for Material ID No.0064C

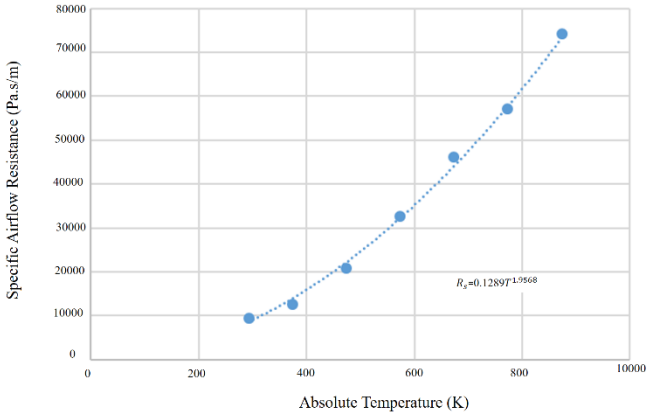

Figure 54. Power law relationship for Material ID No.0058A

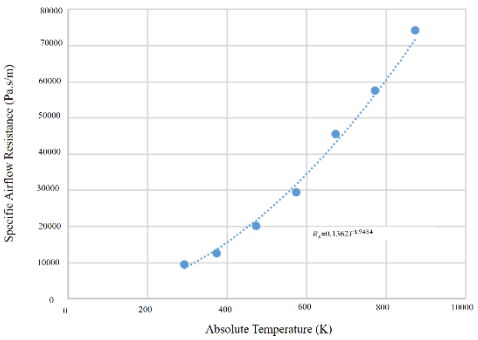

Figure 55. Power law relationship for Material ID No.0058B

In order to assess whether there was a relationship between the exponents for the different materials, all exponents are plotted for the individual samples as shown in Figure 56.

A one-way analysis of variance with Tukey's post –hoc test was conducted on all exponents of power curves for individual material IDs – See Table 60 . Considering the results from three densities, the only significant difference ($p < 0.05$) between exponent values for the different densities are for Materials ID Nos. 0058 and 0064.

Table 60. Statistical test output for exponents of power curves for each material ID.

Exponents								
					95% Confidence Interval for Mean		Minimum	Maximum
Material ID	N	Mean	Std. Deviation	Std. Error	Lower Bound	Upper Bound		
0048	2	1.673000	0.1305319	0.0923000	0.500217	2.845783	1.5807	1.7653
0064	3	1.318600	0.1302333	0.0751902	0.995083	1.642117	1.1685	1.4016
0058	2	1.951100	0.0080610	0.0057000	1.878675	2.023525	1.9454	1.9568
Total	7	1.600571	0.3016016	0.1139947	1.321637	1.879506	1.1685	1.9568

ANOVA					
Exponents					
	Sum of Squares	df	Mean Square	F	Sig.
Between Groups	.495	2	.247	19.393	.009
Within Groups	.051	4	.013		
Total	.546	6			

Multiple Comparisons						
Dependent Variable: Exponents						
Tukey HSD						
(I) material ID	(J) material ID	Mean Difference (I-J)	Std. Error	Sig.	95% Confidence Interval	
					Lower Bound	Upper Bound
0048	0064	.3544000	.1031029	.056	-.013058	.721858
	0058	-.2781000	.1129435	.141	-.680630	.124430
0064	0048	-.3544000	.1031029	.056	-.721858	.013058
	0058	-.6325000*	.1031029	.008	-.999958	-.265042
0058	0048	.2781000	.1129435	.141	-.124430	.680630
	0064	.6325000*	.1031029	.008	.265042	.999958
*. The mean difference is significant at the 0.05 level.						

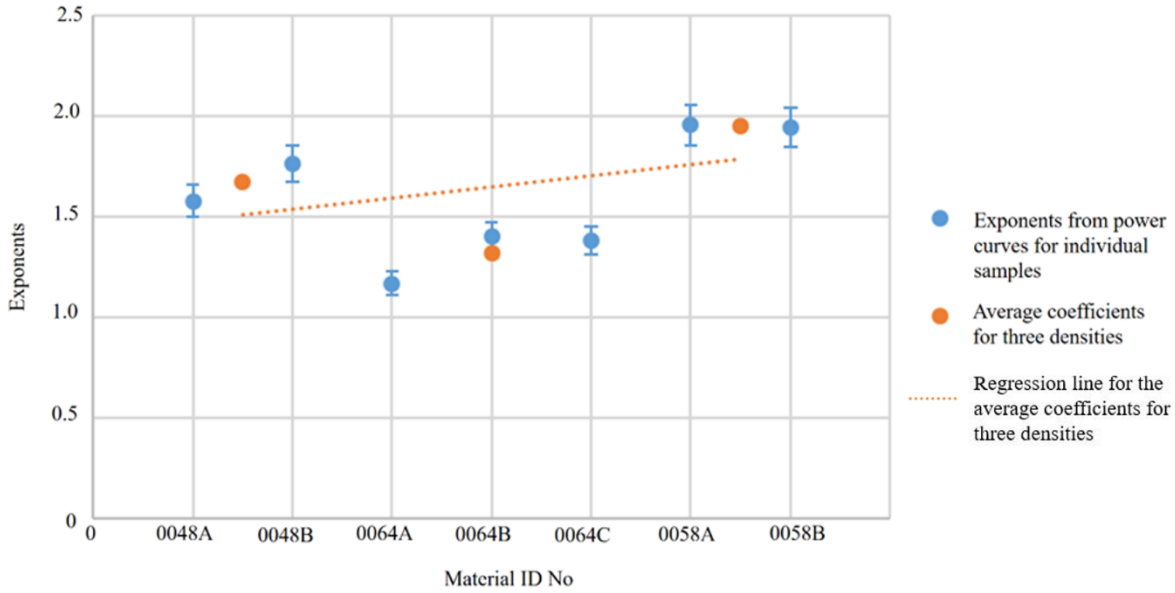

Figure 56. Exponents for individual material ID Nos.

5.3 Summary

This chapter analysed the room temperature and high temperature airflow resistivity measurements. Comparisons were carried out between the measurements related to ISO 9053-1 standards and the measurements conducted according to ASTM C522. The results indicates that for the majority of materials there is less than 10% difference between two sets of measurements.

The effects of air leaks in pipes were assessed experimentally by considering when there is a leak in the air supply and when there are leaks in both air supply and the differential pressure pipe which is connected to the test rig. Results indicated that there is a negligible effect when there is a leak in the supply, and a leak in the differential pressure pipe causes a drop in the differential pressure which is less than 5%.

To check that the ISO and high temperature test rigs gave nominally identical results when measurements were carried out at room temperature, experiments were carried out with 64, 96 and 128 kg/m^3 AES materials. Measurements were carried out using single samples and double samples (i.e. two samples on top of each other) because it was expected that double samples would eventually be needed to achieve measurable differential pressure drops at high temperature. CoV values for all double samples were lower than the corresponding single samples, particularly for the low density material and this was attributed to the mixing of two different samples of this more variable material. The lower CoV was beneficial as it allowed a more rigorous assessment of any differences between the ISO and high temperature test rigs. The statistical tests used to assess the difference between test rigs at room temperature were more reliable for the combination of single and double samples and this confirmed that there was no significant difference between the two test rigs.

High temperature experiments were conducted up to 800 °C for three different densities (64, 96 and 128 kg/m^3) using double samples to ensure a measurable differential pressure. It was observed that the measured thickness of the material was different before and after exposure to high temperatures. The double sample thickness was reduced after heating to 800 °C when inside and outside the test rig; hence it was concluded this shrinkage was not caused by the containment of the material inside the test rig. When there is an unknown reduction in thickness at high temperature it is not appropriate to quote the airflow resistivity of the porous material for which the calculation requires knowledge of the thickness. When the thickness is unknown it is appropriate to calculate the specific airflow resistance instead. However, results were included for both the specific airflow resistance and airflow resistivity as it seems feasible to continue quoting the airflow resistivity up to 600 °C. Regression analysis was used to identify relationships concerning the specific airflow resistance for the three different density materials at different temperatures.

As specific airflow resistance is proportional to T^n, regression analysis was used to identify the exponent, n, as having an average value of 1.6 for these AES materials.

Chapter 6. CONCLUSIONS

This research has led to the design and construction of two test rigs for the measurement of airflow resistance of porous materials used for acoustical applications. The "ISO test rig" is for room temperature measurements according to ISO 9053-1:2018. This is a well-established standard which provided a useful benchmark against which to design and build a "high temperature test rig". The high temperature environment was provided by installing the high temperature test rig within a kiln.

The high temperature test rig has been designed for measurements at temperatures up to 800 ℃ by modifying a design used by Christie [34] that was used for measurements up to 500 °C. To aid the design of this high temperature test rig, Matlab Simulink was used to carry out simulations from which it was possible to establish suitable dimensions for the test rig, carry out thermal stress analysis, assess thermal expansion of joints and pipes, and assess the cooling effect of a heat exchanger on the pipework. The differential pressure drop across the test sample is required but it is only possible to connect the pipes to the measurement equipment once the air has been cooled down closer to room temperature. For this reason, Matlab Simulink and analytical calculations were used to assess the effect of measuring the differential pressure after significant cooling of the air adjacent to the test sample. This showed that the differential pressure measured with the high temperature test rig after cooling of the air is significantly lower than at room temperature. The implication of this finding was that thicker test samples could be needed to ensure that there is a measurable differential pressure.

Initial experiments on a range of AES materials compared room temperature measurements with the ISO test rig according to ISO 9053-1 with measurements according to ASTM C522 from another laboratory that were provided by the funder. Ten samples were measured for each of sixteen material ID numbers. There was close agreement in the measured airflow resistivity (<10% difference) between the two sets of measurements. It is concluded that results from the ISO test rig and those from the other laboratory according to ASTM C522 can be considered to be nominally identical.

For the high temperature measurements inside the kiln there is very limited scope to identify problems such as air leaks in the pipes. For this reason, an assessment was made of the problem

at room temperature by introducing artificial leaks. The results indicated that there was negligible effect when there was a leak in the supply because the flow rate is always manually adjusted to give the required flow velocity. For typical AES materials it was concluded that any minor leaks due to thermal expansion in the test rig and/or pipes would result in a negligible error in the airflow resistivity.

To check that the ISO and high temperature test rigs gave nominally identical results when measurements were carried out at room temperature, experiments were carried out with 64, 96 and 128 kg/m^3 AES materials. Measurements were carried out using single samples and double samples (i.e. two samples on top of each other) because it was expected that double samples would eventually be needed to achieve measurable differential pressure drops at high temperature. The statistical tests were more reliable for the combination of single and double samples which confirmed that there is no significant difference between the two test rigs.

An assessment was then made as to whether the fitting of double samples inside the sample holders leads to a more compressed material inside the test rigs than with single samples. Compression was found to occur with both test rigs; hence it is important to measure the thickness of the sample when fitted inside the test rig if it is required to calculate airflow resistivity rather than specific airflow resistance.

Comparison of measured airflow resistivity of single and double samples indicated that they are sometimes significantly different. The commercial implication is that when measurements are made using double samples, the measured airflow resistivity will not always correspond to the thickness of the product which is sold and installed.

High temperature experiments were conducted up to 800 °C for three different densities (64, 96 and 128 kg/m^3) using double samples to ensure a measurable differential pressure. It was observed that the measured thickness of the material was different before and after exposure to high temperatures. The double sample thickness was reduced after heating to 800 °C when inside and outside the test rig; hence it was concluded this shrinkage was not caused by the containment of the material inside the test rig. When there is an unknown reduction in thickness at high temperature it is not appropriate to quote the airflow resistivity of the porous material for which the calculation requires knowledge of the thickness. When the thickness is unknown it is appropriate to calculate the specific airflow resistance instead. However, results were

included for both the specific airflow resistance and airflow resistivity as it seems feasible to continue quoting the airflow resistivity up to 600 ℃. In addition to the thickness change, the results showed a general increase in the differential pressure (and corrected differential pressure) from 20 to ≈600 ℃ above which there was a reduction between ≈600 and 800 ℃.

The high temperature tests from the three densities indicate that it might be possible to assume no significant effect of temperature on specific airflow resistance for 20 and 100 ℃. Whilst there was not always a significant difference between results in 100 ℃ steps, this choice was reasonable although the change in material properties above 600 ℃ means that future work could use smaller temperature steps to assess changes in specific airflow resistance as the material crystallises.

Regression analysis was used to identify relationships concerning the specific airflow resistance for the three different density materials at different temperatures. To achieve this it was necessary to use the sample mass (instead of bulk density as used at room temperature) because the unknown reduction in material thickness above 600 ℃ meant that the density was also unknown across the entire frequency range.

Theory indicates that specific airflow resistance is proportional to absolute temperature, T, in terms of T^n; hence regression analysis was used to identify the exponent, n, as having an average value of 1.6 for these AES materials.

In this project the main comparisons between the two test rigs were all carried out with an airflow velocity of 0.5×10^{-3} m/s. Whilst it was shown that at room temperature there is little difference between the specific airflow resistance measured with an airflow velocity between 0.5×10^{-3} m/s and 4×10^{-3} m/s, this was not the case at 800℃. Hence for high temperature applications the airflow velocity should be chosen to correspond to the sound pressure level in the specific industrial application.

6.1 Limitations of the research and recommendations for future work

Since AES materials are relatively soft materials, it is necessary to consider the fitting of the material inside the test rig. Therefore, it is recommended to use transparent material to build the high temperature test rig and, although the fabrication cost is relatively higher, quartz could

be considered as a better option as it can withstand at the maximum temperature of 1200 ℃. In addition, because the differential pressure is relatively low at 800 ℃, it is recommended to increase the sample thickness in order to have the measurable value for the differential pressure.

For high temperature measurements where the differential pressure can be low, the measuring instrument will often need to measure lower values than would occur at room temperature.

Future work could investigate other materials as this research indicated that the power exponent relationship with absolute temperature and specific airflow resistance cannot be estimated using Sutherland's law.

REFERENCES

[1] V. Ganapathy, Industrial Boilers and Heat Recovery Steam Generators -Design , Applications and Calculations, New York: Marcel Dekker Inc, 2003.

[2] "ISO 9053-1," European Committee for Standardization (CEN), Brussels, 2018.

[3] V. Gambino and P. Ashtiani, "Acoustic Performance Considerations for A 'Once Through Steam Generators'(OTSG)," in *17 th Symposium on Industrial Applications of Gas Turbines (IAGT)* , Banff, Alberta, Canada, 2007.

[4] H. Kuttruff, Room Acoustics, Apple Academic Press Inc., 2016.

[5] T. Cox and P. D'Antonio, Acoustic Absorbers and Diffusers : Theory Design and Application, CRC Press, 2009.

[6] C. Hopkins, Sound Insulation, Oxford: Elsevier, 2007.

[7] "ASTM C522 Standard Test Method for Airflow Resistance of Acoustical Materials," ASTM International, West Conshohocken, 2016.

[8] J. F. Allard and G. Daigle, "Propagation of Sound in Porous Media: Modeling Sound Absorbing Materials," *The Journal of the Acoustical Society of America* , vol. 95, pp. 2785-2793, 1994.

[9] M. E. Delany and . E. N. Bazley, "Acoustical Properties of Fibrous Absorbent Materials," *Applied Acoustics,* vol. 3, pp. 105-116, 1970.

[10] N. Dauchezl, S. Sahraoui and N. Atalla, "Validation of 3 D poroelastic Finite Element from the Impedence Measurement of a Vibrating Foam Sample," *Can Acoust,* vol. 4, pp. 94-95, 2000.

[11] X. Mendibil, *Medida de la Absorción Acústica De Los Materiales Poroelásticos. Thesis Presented in the University of Mondragón,* Spain, 2004.

[12] M. R. Stinson and G. A. Daigle, "Electronic System for the Measurement of Flow Resistance," *Journal of the Acoustical Society of America,* vol. 83, no. 6, pp. 2422-2428, 1998.

[13] J. Pan and P. Jackson, "Review of Test Methods for Material Properties of Elastic Porous Materials," *SAE International Journal of Materials and Manufacturing,* vol. 2, no. 1, pp. 570-579, 2009.

[14] D. A. Bies and C. H. Hansen, "Flow Resistance Information for Acoustical Design," *Applied Acoustics,* vol. 13, pp. 357-391, 1980.

[15] "Standard Method of Test for Airflow Resistance of Acoustical Materials," ASTM International, West Conshohocken, 1972.

[16] R. L. Brown and R. H. Bolt, "The Measurements of Flow Resistance of Porous Acosustics Materials," *The Journal of the Acoustical Society of America,* vol. 13, no. 4, pp. 337-345, 1942.

[17] R. Dragonetti, C. Ianniello and R. A. Romano, “Measurement of the Resistivity of Porous Materials with an Alternating Airflow Method,” *The Journal of the Acoustical Society of America,* vol. 753, 2011.

[18] M. Garai and F. Pompoli, “A European Inter Laboratory Test of Airflow Resistivity Measurements,” *Acta Acustica United With Acustica,* vol. 89, no. 2, pp. 471-478, 2003.

[19] N. Kino and T. Ueno, “Improvements to the Johnson–Allard Model for Rigid-Framed Fibrous Materials,” *Applied Acoustics,* vol. 68, p. 1468–1484, 2007.

[20] J. F. Allard and N. Atalla, “Propagation of Sound in Porous Media;Modelling Sound Absorbing Materials .,” in *Wiley,* Chichester, 2009.

[21] J. F. Allard and Y. Champoux, “New Empirical Equations for Sound Propagation in Rigid Frame Fibrous Material,” *The Journal of the Acoustical Society of America,* vol. 95, pp. 3346-3353, 1992.

[22] M. E. Delany and E. N. Bazley, “Acoustical Properties of Fibrous Absorbent Materials,” *Applied Acoustics,* vol. 3, no. 1, pp. 105-116, 1970.

[23] H. Nichols, “Flow-Resistance Characteristics of Fibrous Acoustical Materials*,” *The Journal of The Acoustical Society of America,* vol. 19, 1947.

[24] V. G. Venzke, R. Behr and H. Deicke, “Extended Facilities for Measuring the Flow Resistance of Porous Layers,” *Acta Acustica United With Acustica,* vol. 26, pp. 141-146, 1972.

[25] R. F. Lambert and J. S. Tesar, “Acoustic Structure and Propagation in Highly Porous, Layered, Fibrous Materials,” *The Journal of the Acoustical Society of America,* vol. 76, no. 1231, pp. 1231-1237, 1984.

[26] P. M. Morse and K. U. Ingard, Theoretical Acoustics, New Jersey: Mc-GrewHill, 1986.

[27] C. W. Kosten and C. Zwikker, “Theory of the Absorption of Sound by Compressible Walls with a Non- Porous Surface Layer,” *Physica,* vol. 8, no. 2, pp. 251-271, 1941.

[28] M. A. Biot, “The Elastic Coefficients of the Theory of Consolidation,” *Jouranal of Acoustical Society,* vol. 28, pp. 179-191, 1956.

[29] M. A. Picard and P. Solana, “A Method of Measuring the Dynamic Flow Resistance and the Acoustic Measurement of the Effective Static Flow Resistance in Stratified Rockwool Samples,” *Journal of Sound and Vibration,* vol. 216, no. 3, pp. 495-505, 1998.

[30] M. Ren and F. Jacobsen, “A Method of Measuring the Dynamic Flow Resistance and Reactance of Porous Materials,” *Applied Acoustics,* vol. 39, pp. 265-276, 1993.

[31] W. Qunli, “Empirical Relations between Acoustical Properties and Flow Resistivity of Porous Plastic Open-Cell Foam,” *Applied Acoustics,* vol. 25, p. 141 – 148, 1988.

[32] A. Cummings and I.-J. Chang, “Acoustic Propagation in Porous Media with Internal Mean Flow,” *Journal of Sound and Vibration,* vol. 3, no. 114, pp. 565-581, 1987.

[33] A. Cummings and S. P. Beadle, “Acoustic Properties of Reticulated Plastic Foams,” *Journal of Sound and Vibration,* vol. 175, no. 1, pp. 115-133, 1994.

[34] D. R. A. Christie, “Measurement of the Acoustic Properties of a Sound Absorbing Material at High Temperatures,” *Journal of Sound and Vibration,* vol. 46, no. 3, pp. 347-355, 1976.

[35] O. K. Mawardi, “Measurement of Acoustic Impedance,” *The Journal of the Acoustical Society of America,* vol. 21, no. 2, pp. 84-91, 1949.

[36] P. Miglietta, E. Negro, F. Sini, G. Nierop, G. Toniato, C. Guglielmone and A. Schiavi, “Measurement of Airflow Resistivity Variation due to Temperature and its Impact on Simulated Sound Absorption Inside a Vehicle's Passenger Compartment,” *SAE International Journal of Passenger Cars Mecahnical Systems,* no. 3, pp. 901-915, 2010.

[37] X. Wang, F. Peng and B. Chang, “Sound Absorption of Porous Metals at High Sound Pressure Levels,” *Journal of Acoustical Society of America,* vol. 2, pp. 126-133, 2009.

[38] X. Wang, Y. Li, T. Chen and Z. Ying, “Research on the Sound Absorption Characteristics of Porous Metal Materials at High Sound Pressure Levels,” *Advances in Mechanical Engineering,* vol. 7, no. 5, pp. 1-7, 2015.

[39] F. Giese, H.-C. Ries and C. Eigenbrod, “On the Performance of Porous Sound Absorbent Material in High Temperature Applications,” Germany, 2010.

[40] D. Bies and P. A. Franken, “Flow Resistance of Fibrous Materials,” *The Jouranl of The Acoustical Society of America,* vol. 33, 1961.

[41] H. Nichols, “Flow-Resistance Characteristics of Fibrous Acoustical Materials,” *The Journal of The Acoustical Society of America,* vol. 19, 1947.

[42] P. P. Narang, “Material Parameter Selection in Polyester Fibre Insulation for Sound Transmission and Absorption,” *Applied Acoustics,* vol. 45, pp. 335-358, 1995.

[43] P. C. Carman, “Permeability of Saturated Sands, Soils and Clays,” *Journal of Agricultural Science,* vol. 29, pp. 263-273, 1939.

[44] P. C. Carman, “Flow of Gases through Porous Media,” Butterworth, London, 1956.

[45] K. Attenborough, “Acoustical Characteristics of Porous Materials,” *Physics Reports,* vol. 82, no. 3, pp. 179-227, 1982.

[46] K. Attenborough, “Acoustical Characteristics of Rigid Fibrous Absorbents and Granular Materials,” *The Journal of the Acoustical Society of America,* vol. 73, pp. 785-799, 1983.

[47] K. Attenborough, “Acoustical Impedance Models for Outdoor Ground Surfaces,” *Journal of Sound and Vibration,* vol. 99, no. 4, pp. 521-544, 1985.

[48] N. Voronina , “Acoustic Properties of Fibrous Materials,” *Applied Acoustics,* vol. 42, pp. 165-174, 1994.

[49] R. Delrey, J. Alba, J. P. Arenas and V. J. Sanchis, “An Empirical Modelling of Porous Sound Absorbing Materials Made of Recycled Foam,” *Applied Acoustics,* vol. 73, no. 6-7, pp. 604-609, 2012.

[50] E. Nousiainen, V. Hongisto and M. Lindgreen, “Accoustical Characterization of Fiberous Materials by Using Measured Flow Resistivity Data,” in *Extended Facilities for Measuring the Flow Resistance of Porous Layers,* France, 2000.

[51] D. Cuiyun, C. Guang, X. Xinbang and L. Peisheng, “Sound Absorption Characteristics of a High-Temperature Sintering Porous Ceramic Material,” *Applied Acoustics,* vol. 73, pp. 865-871, 2012.

[52] K. U. Ingard and T. A. Dear, “Measurement of Acoustic Flow Resistance,” *Journal of Sound and Vibration,* vol. 103, no. 4, pp. 567-572, 1985.

[53] M. A. Kuczmarski and J. C. Johnston, “Acoustic Absorption in Porous Materials,” National Aeronautics and Space Administration, Ohio, 2011.

[54] J. R. Pearse and M. J. Kingan, “Measurement of Sound in Airflow,” in *The Thirteenth International Congress on Sound and Vibrations*, Vienna, 2006.

[55] D. L. Johnson, D. L. Hemmick and H. Kojima, “Probing Porous Media with First and Second Sound. I. Dynamic Permeability,” *Journal of Applied Physics,* vol. 76, pp. 104-114, 1994.

[56] M. Yasushi , “Acoustical Properties of Porous Materials -Modifications of Delany- Bazley Models,” *Journal of Acoustical Society of Japan,* vol. 11, no. 1, pp. 19-28, 1990.

[57] B. Zhang and X. Wang, “Numerical Simulation of Acoustic Properties of Porous Metals under High Sound Pressure Level Conditions,” in *The 21st International Congress on Sound and Vibration*, Beijing, 2014.

[58] F. P. Mechel and I. Ver, “Sound Absorbing Materials and Sound Absorbers,” *Noise and Vibration Control Engineering: Principles and Applications,* pp. 203-243, 1992.

[59] J. C. Maxwell, “The Bakerian Lecture - On the Viscosity or Internal Friction of Air and Other Gases,” 1866.

[60] W. D. Niven, The Scientific Papers of James Clerk Maxwell, vol. 19, New York: Cambridge University Press, 1890, p. 387.

[61] W. H. Furry, “On the Elementary Explanation of Diffusion Phenomena in Gases,” *American Journal of Physics,* vol. 16, pp. 63-78, 1948.

[62] R. D. Present, Kinetic Theory of Gases, London: McGraw-Hill Book Company,Inc, 1958.

[63] G. C. Maitland, “Intermolecular Forces: Their Origin and Determination,” in *Oxford University Press,* 1981.

[64] W. Sutherland, “The Viscosity of Gases and Molecular Force,” *Philosophical Magazine Series 5,* vol. 223, no. 36, pp. 507-531, 1893.

[65] P. Miglietta , E. Negro, F. Sini, G. Nierop, G. Toniato, C. Guglielmone and A. Schiavi, “Measurement of Airflow Resistivity Variation Due toTemperature and Its Impact on Simulated Sound Absorption Inside a Vehicle's Passenger Compartment,” *SAE International,* vol. 1, no. 1417, pp. 901-915, 2010.

[66] A. M. Biot , “Theory of propagation of elastic waves in a fluid-saturated porous solid: I. Low frequency range,” *Journal of Acoustics Society of America,* vol. 28, 1956.

[67] A. J. Smits and J. P. Dussauge, Turbulent Shear Layers in Supersonic Flow, New York: Springer Science+Business Media, Inc, 1996.

[68] E. UG, “fx Solver,” Equanalysis UG, 2017. [Online]. Available: https://www.fxsolver.com/about/. [Accessed 29 11 2018].

[69] “IPFS,” 05 2017. [Online]. Available: https://ipfs.io/ipfs/QmXoypizjW3WknFiJnKLwHCnL72vedxjQkDDP1mXWo6uco/wiki/Hagen%E2%80%93Poiseuille_equation.html. [Accessed 29 11 2018].

[70] F. Controls, “Certificate of Calibration,” Furness Controls LTD, East Sussex, 2017.

[71] “LFR Filter Regulator Hand Book,” AMJ Pneumatics, 2017.

[72] Y. A. Cengel, Heat Transfer,A Practical Approach, London: McGraw-Hill, 2000.

[73] “Modeling Gas Systems,” The MathWorks, 1994-2018. [Online]. Available: https://uk.mathworks.com/help/physmod/simscape/ug/modeling-gas-systems.html. [Accessed 29 11 2018].

[74] E. A. Basuki, . D. . H. Prajitno and . F. Muhammad, “Alloys Developed for High Temperature Applications,” in *The 1st International Process Metallurgy Conference,* Indonesia, 2016.

[75] “Fused Quartz Properties & Usage Guide,” Momentive Performance Materials Quartz,inc, 18 May 2007. [Online]. Available: http://www.quartz.com/gedata.html. [Accessed 29 11 2018].

[76] M. Takahashi, H. Nagahama, T. Masuda and A. Fujimura, “Fractal Analysis of Experimentally, Dynamically Recrystallized Quartz Grains and its Possible Application as a Strain Rate Meter,” *Journal of Structural Geology,* vol. 20, no. 2-3, pp. 269-275, 1998.

[77] “Quartz Glass: High Temperature Glass Resistant,” John Moncrieff Ltd, 2018. [Online]. Available: https://www.johnmoncrieff.co.uk/quartz-glass/.. [Accessed 29 11 2018].

[78] W. G. Fahrenholtz, E. J. Wuchina, W. E. Lee and Y. Zhou, Ultra-High Temperature Ceramics: Materials for Extreme Environment Applications, Willey.

[79] E. Wuchina, E. Opila, M. Opeka, W. Fahrenholtz and I. Talmy, “UHTCs: Ultra-High Temperature Ceramic Materials for Extreme Environment Applications,” The Electrochemical Society, New Jersey, 2007.

[80] F. Monteverde, A. Bellosi and L. Scatteia, “Processing and properties of ultra-high temperature ceramics for space applications,” *Materials Science and Engineering,* vol. 485, no. 1-2, pp. 415-421, 2008.

[81] E. Opila, S. Levine and J. Lorincz, “Oxidation of ZrB2- and HfB2-Based Ultra-High Temperature Ceramics: Effect of Ta Additions,” *Journal of Materials Science,* vol. 39, no. 19, p. 5969–5977, 2004.

[82] A. Sanusi, I. Adeoye, O. Opeyemi, J. V. Ademola and S. Oshenye, “Nickel based Super Alloys for Gas Turbines Applications,” Ottawa, 2015.

[83] Alloy, “High Temperature Nickel Alloys Applications,” Heanjia Super Metal Co. Ltd, 2015. [Online]. Available: https://super-metals.com/applications/high-temperature-nickel-alloys-applications/. [Accessed 29 11 2018].

[84] L. Shi and D. O. Northwood, “The Mechanical Behavior of An AISI Type 310 Stainless Steel,” *Acta Metallurgica et Materialia,* vol. 43, no. 2, pp. 453-460, 1995.

[85] A. Kosmac, “Stainless Steel at High Temperature,” European Stainless Steel Development Association, Brussels, 2012.

[86] L. Digital, “Martensitic Stainless Steels,” British Stainless sleet Association, 2018. [Online]. Available: https://www.bssa.org.uk/topics.php?article=253. [Accessed 30 11 2018].

[87] B. Weiss and R. Stickler, “Phase Instabilities During High Temperature Exposure of 316 Austenitic Stainless Steel,” *Metallurgical and Materials Transactions B,* vol. 3, no. 4, pp. 851-866, 1972.

[88] H.-W. Hsu and T. T. Wen , “High Temperature Corrosion Behavior of Siliconized 310 Stainless Steel,” *Materials Chemistry and Physics,* vol. 64, no. 2, pp. 147-155, 2000.

[89] A. S. Metals, “Stainless Steel - High Temperature Resistance,” AZO Materials, 2002. [Online]. Available: https://www.azom.com/article.aspx?ArticleID=1175. [Accessed 29 11 2018].

[90] “The Stainless Steel Information Center,” US Super Alloys, [Online]. Available: http://www.ssina.com/composition/temperature.html. [Accessed 29 11 2018].

[91] M. F. Montemor, M. Ferreira, N. Hakiki and M. D. Cunha Belo, “Chemical Composition and Electronic Structure of the Oxide Films Formed on 316L Stainless Steel and Nickel Based Alloys in High Temperature Aqueous Environments,” *Corrosion Science,* vol. 42, no. 9, pp. 1635-1650, 2000.

[92] V. S. Sirinivasan, M. Valsan, R. Sandhy , K. B. S. Rao, S. L. Mannan and D. H. Sastry, “High Temperature Time-Dependent Low Cycle Fatigue Behaviour of a Type 316L(N) Stainless Steel,” *International Journal of Fatigue,* vol. 21, no. 1, pp. 11-21, 1999.

[93] “316 Stainless Steel,” Metals4U LTD, [Online]. Available: https://www.metals4u.co.uk/316-Stainless-Steel.asp. [Accessed 30 11 2018].

[94] “High Temeperature Properties,” The Stainless Steel Information Center, [Online]. Available: http://www.ssina.com/composition/temperature.html. [Accessed 10 December 2018].

[95] W. Nayak, “Engistudies,” 01 October 2017. [Online]. Available: https://www.engistudies.com/2017/10/von-mises-stress-analysis.html. [Accessed 14 March 2019].

[96] A. N. Eraslan and H. Argeso , “On the Application of von Mises’ Yield Criterion to a Class of Plane Strain Thermal Stress Problems,” *Turkish Journel of Engineering and Environmental Science,* vol. 29, pp. 113-128, 2004.

[97] “Autodesk Knowledge Network,” Autodesk, 2018. [Online]. Available: https://knowledge.autodesk.com/support/simulation-mechanical/learn-explore/caas/CloudHelp/cloudhelp/2018/ENU/SimMech-UsersGuide/files/GUID-

BD892BF5-3243-4DE3-9A59-9BFAAAD533FC-htm.html?st=how to do temperature distribution. [Accessed 09 12 2018].

[98] "Air - Thermophysical Properties," Engineering ToolBox, 2003. [Online]. Available: https://www.engineeringtoolbox.com/air-properties-d_156.html . [Accessed 30 November 2018].

[99] "Water - Thermophysical Properties," Engineering ToolBox, 2003. [Online]. Available: https://www.engineeringtoolbox.com/water-thermal-properties-d_162.html. [Accessed 30 November 2018].

[100] D. Roncati , "Iterative Calculation of the Heat Transfer Coefficient," Progettazione Ottica Roncati, Ferrara - Italy.

[101] "EN 12939:2000," European Committe for Standardisation (CEN) , Brussels, 2000.

[102] B. Standards, "Refractory Products -Methods of Test for Ceramic Fibre Products-ISO 10635 1999," International Standard Organisation (ISO), 2000.

[103] " Ideal Gas Law," Engineering ToolBox, 2003. [Online]. Available: https://www.engineeringtoolbox.com/ideal-gas-law-d_157.html . [Accessed 30 11 2018].

[104] "Easycalculation.com," [Online]. Available: https://www.easycalculation.com/statistics/learn-tukeys-post-hoc.php. [Accessed 03 April 2019].

[105] L. G. Bäck, S. Ali, S. Karlsson, D. Möncke, E. . I. Kamitsos and B. Jonson, "Mixed alkali/alkaline earth-silicate glasses: Physical properties and structure by vibrational spectroscopy," *International Journal of Applied Glass Science,* pp. 1-14, 2019.

[106] T. P. Brown and P. T. C. Harrison, "Crystalline Silica in Heated Man-Made Vitreous Fibres: A Review," *Regulatory Toxicology and Pharmacology,* vol. 68, pp. 152-159, 2014.

[107] G. J. Tatlock, T. J. Hurd and J. S. Punni, "High Temperature Degradation of Nickel Based Alloys," University of Liverpool, Liverpool.

[108] J. Kozeny, "Ueber kapillare Leitung des Wassers im Boden," *Stizungsber Akad Wiss Wien,* vol. 136, pp. 271-306, 1927.

[109] P. C. Carman, "Fluid flow through granular beds," *Transactions of Instituition of Chemical Engineers,* vol. 15, pp. 150-167, 1937.

[110] T. D. Eastop and A. McConkey, Applied thermodynamics for engineering technologists, Pearson Education LTD, 2009.

[111] B. W. Evans, "Application of a reaction rate method to the breakdown equilibrium of muscovite and mucovite plus quartz," *American Journal of Science,* vol. 263, pp. 647-667, 1965.

[112] A. Nowotnik, "Nickel-Based Superalloys," Elsevier B.V, 2018. [Online]. Available: https://www.sciencedirect.com/topics/materials-science/nickel-based-superalloys. [Accessed 29 11 2018].

[113] D. Capecchi and G. Ruta, “Strength of Materials and Theory of Elasticity in 19th Century Italy,” 2015.

[114] J. . E. Shigley, , C. R. Mischke and R. G. Budynas, Mechanical Engineering Design.

[115] “Finite element analysis,” SimWiki, [Online]. Available: https://www.simscale.com/docs/content/simwiki/fea/what-is-von-mises-stress.html. [Accessed 30 11 2018].

[116] D. Zhao, P. Yang, N. Melosh, J. Feng, F. Bradley , Chmelka and G. . D. Stucky, “Continuous Mesoporous Silica Films with Highly Ordered Large Pore Structures,” *Journal of Advanced Materials,* vol. 10, no. 16, pp. 1380-1385, 1998.

[117] M. Bilova and E. Lumnitzer, “Acoustical prameters of porous materials and their measurements,” *ACTA Technica Corviniensis- Bulletin of Engineering,* vol. 4, pp. 1-4, 2011.

[118] R. J. Ackermann and C. A. Sorrell, “Thermal Expansion and the High-Low Transformation in Quartz;High-Temperature X-ray Studies,” *Applied Crystals,* vol. 7, pp. 461-467, 1974.

[119] “Dry Air Properties,” Engineering ToolBox, 2005. [Online]. Available: https://www.engineeringtoolbox.com/dry-air-properties-d_973.html . [Accessed 02 07 2019].

[120] M. E. Davis, “Ordered Porous Materials for Emerging Applications,” *Nature,* vol. 417, pp. 813-821, 2002.

[121] D. L. Johnson, J. Koplik and R. Dashen, “Theory of dynamic permeability and tortuosity in fluid-saturated porous media,” *Journal of fluid mechanics,* vol. 176, pp. 379-402, 1987.

[122] K. V. Horoshenkov and M. J. Swift, “The effect of consolidation on the acoustic properties of loose rubber granulates,” *Applied Acoustics,* vol. 62, p. 665 – 690, 2001.

[123] M. Henry , P. Lemarinier, J. F. Allard, J. L. Bonardet and A. Gedeon, “Evaluation of the Characteristic Dimensions of Porous Sound-Absorbing Materials,” *Journal of Applied Physics,* vol. 77, pp. 17-20, 1995.

APPENDICES

Appendix A. ISO Test rig AutoCAD drawings

Appendix B. High temperature test rig AutoCAD drawings

Appendix C. Schematic diagram for airflow at room temperature

Appendix D. Schematic diagram for airflow at high temperature

Appendix E. Specific airflow resistance and air resistivity values for all material ID s

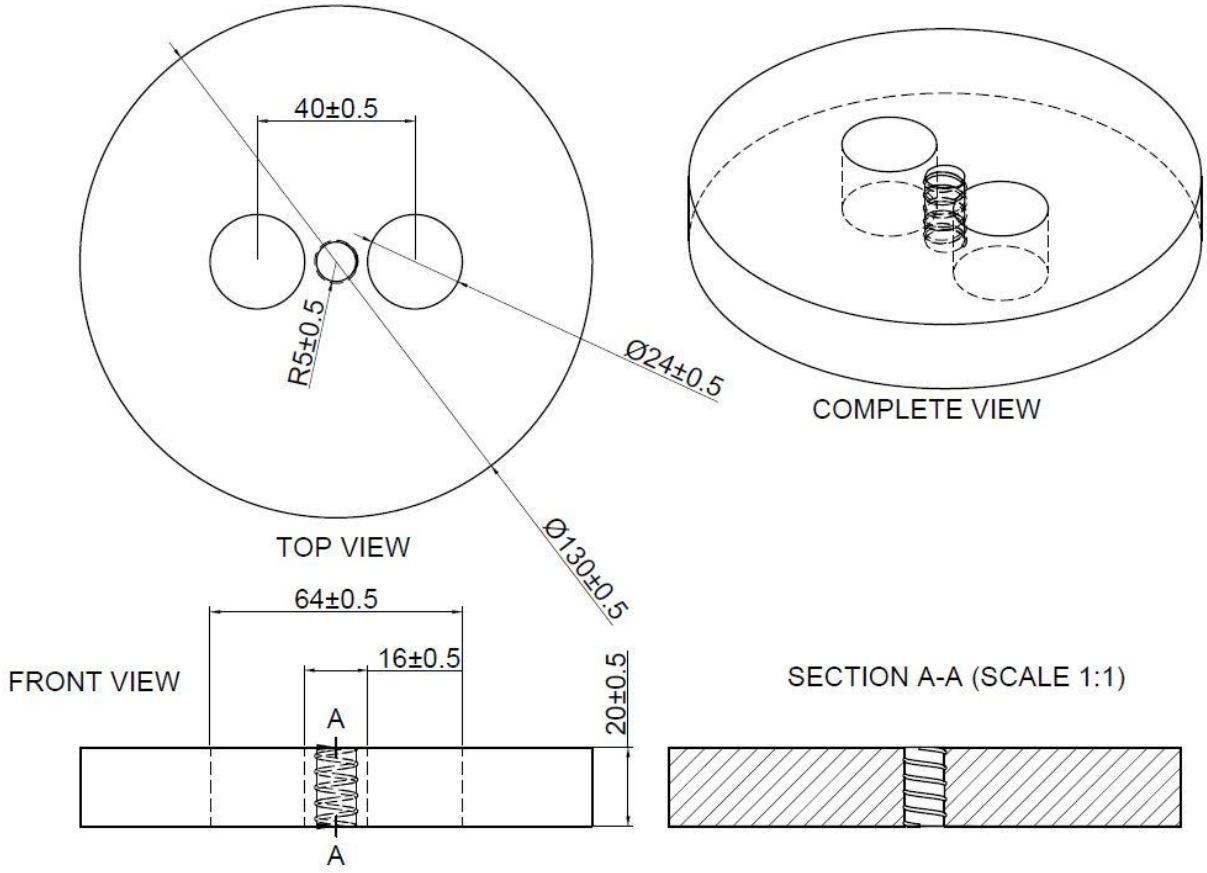

Figure A 1. ISO Test rig: Plunger assembly part 01

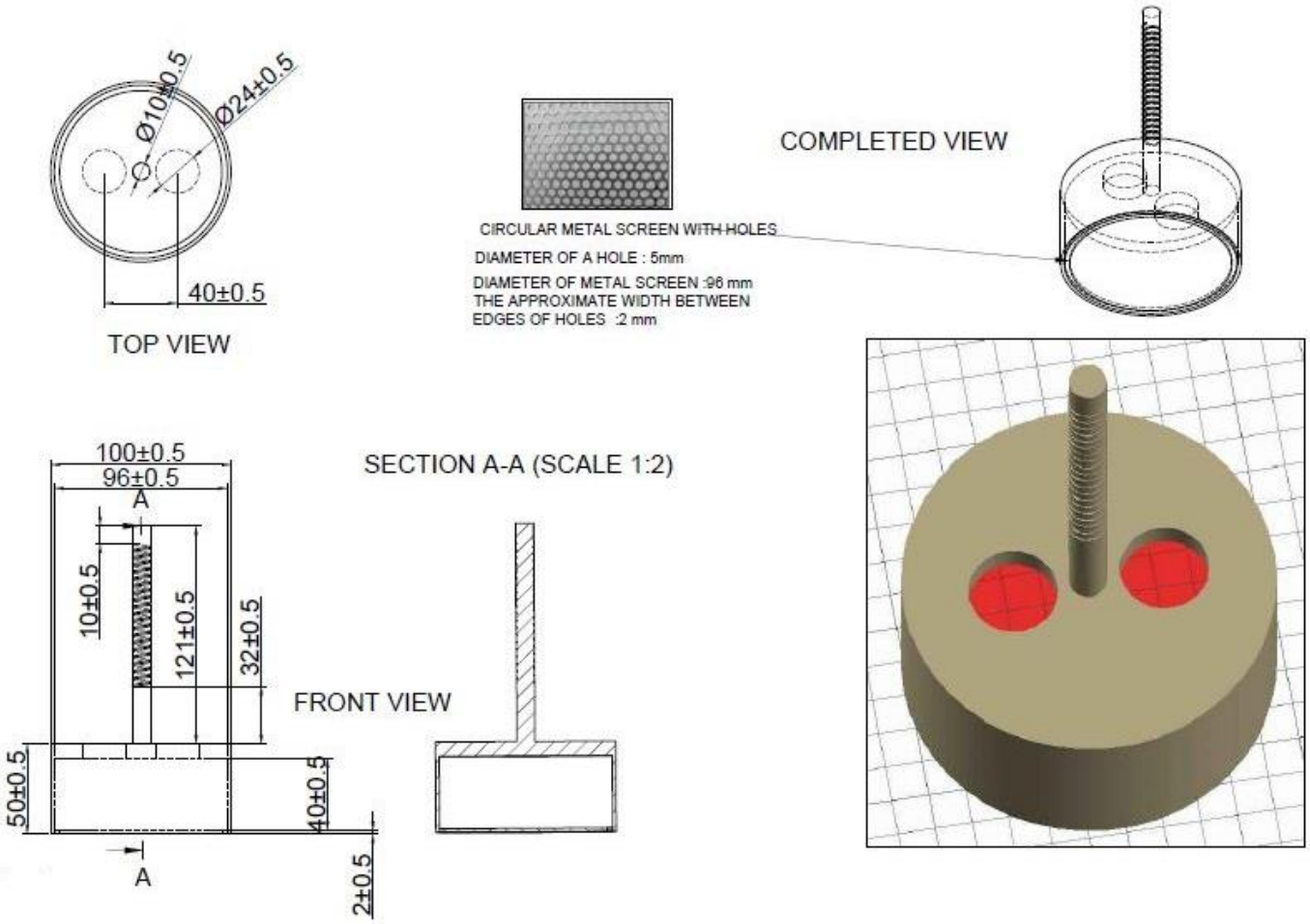

Figure A 2. ISO Test rig: Plunger assembly part 02

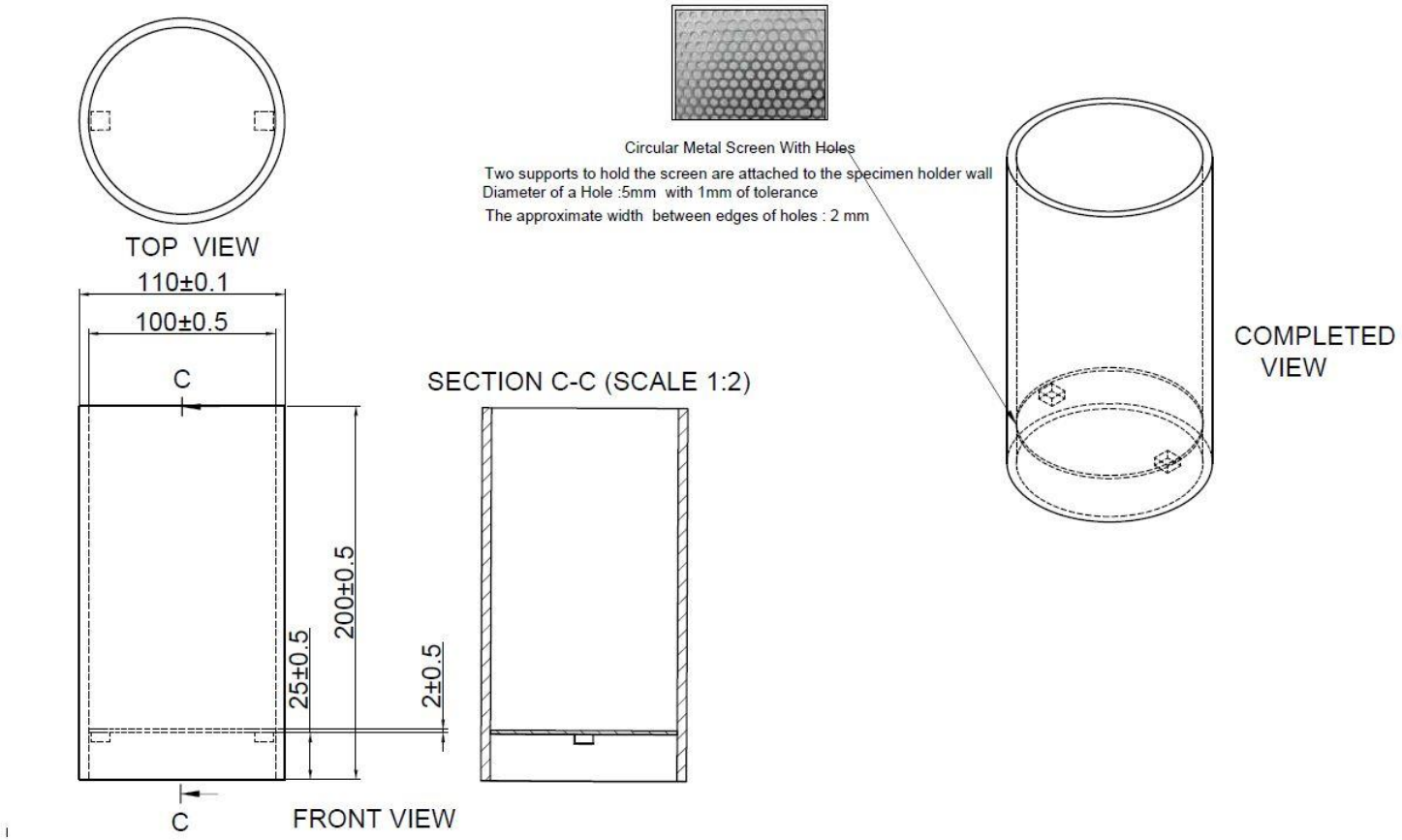

Figure A 3. ISO Test rig: Specimen holder

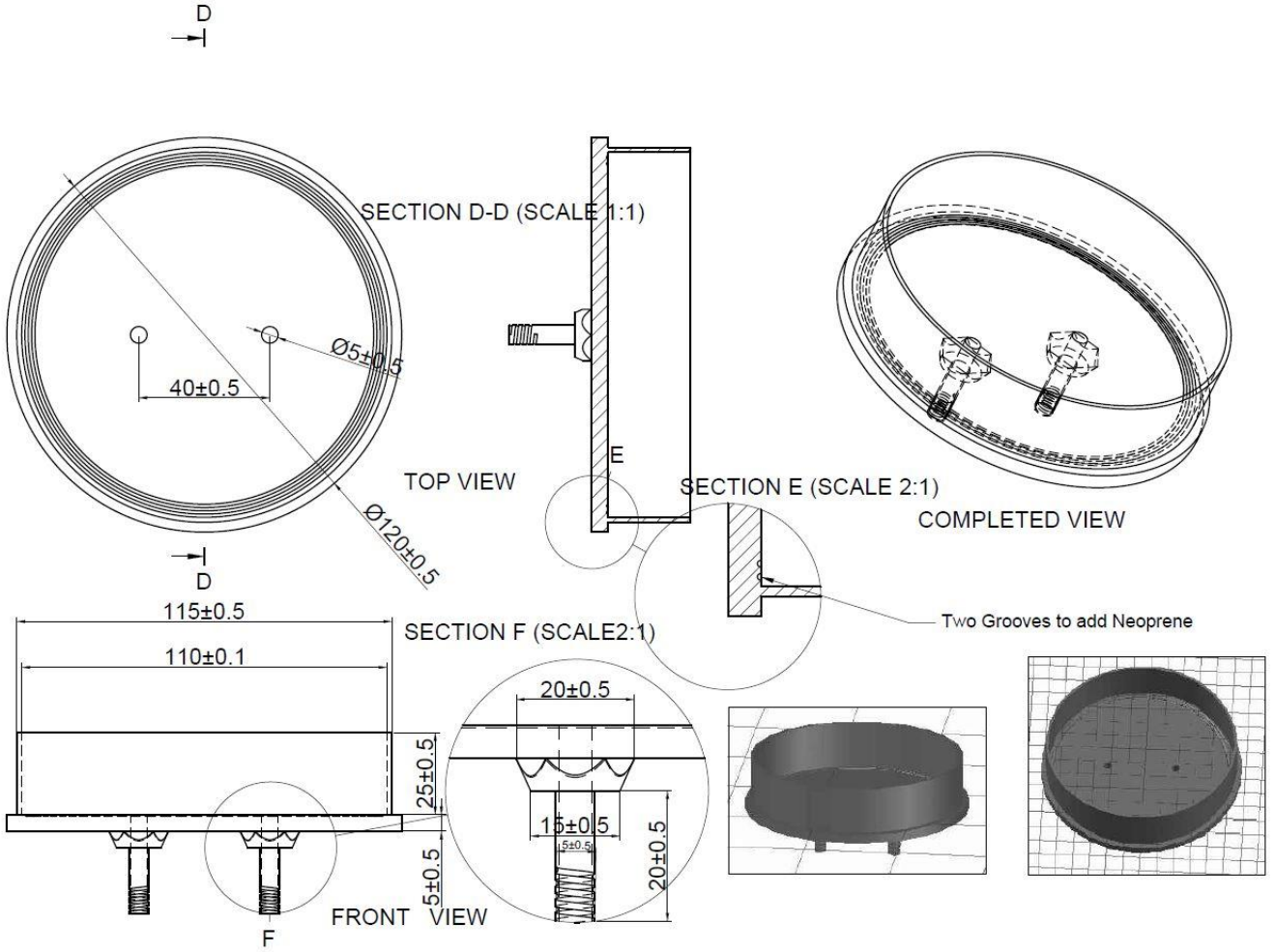

Figure A 4. ISO Test rig: Metal sleeve

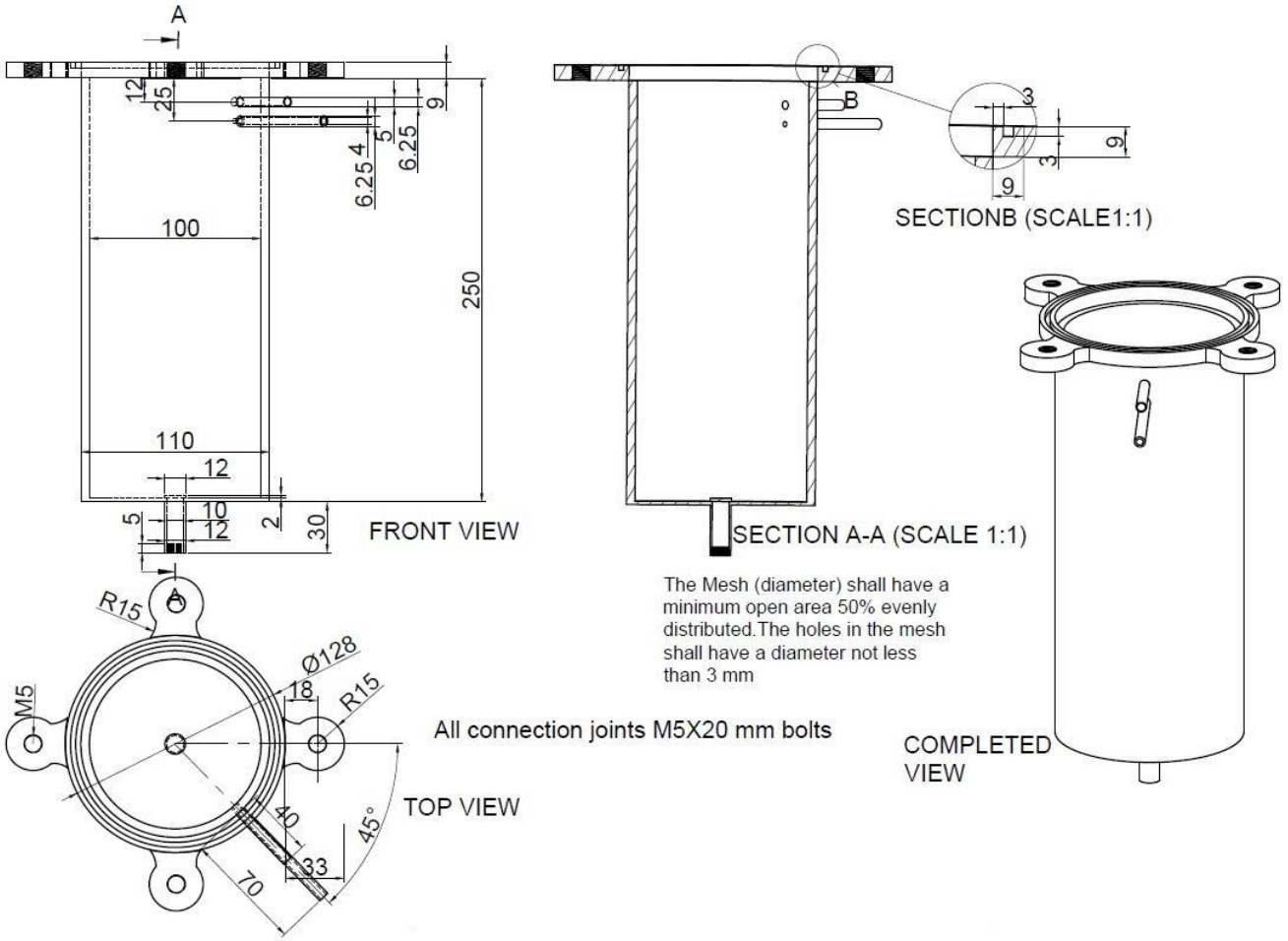

Figure B 1. High temperature test rig: Preheater

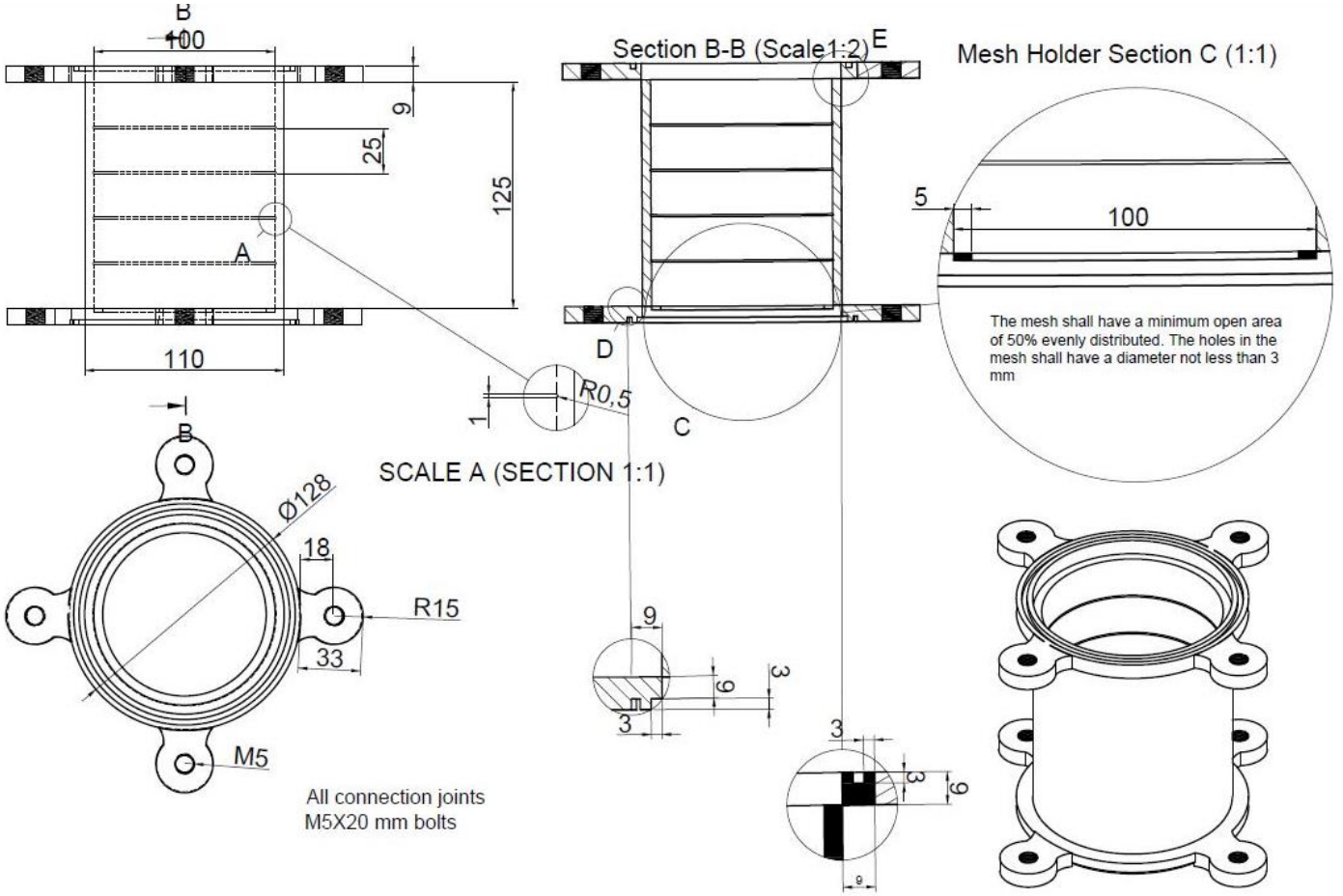

Figure B 2. High temperature test rig: Specimen holder

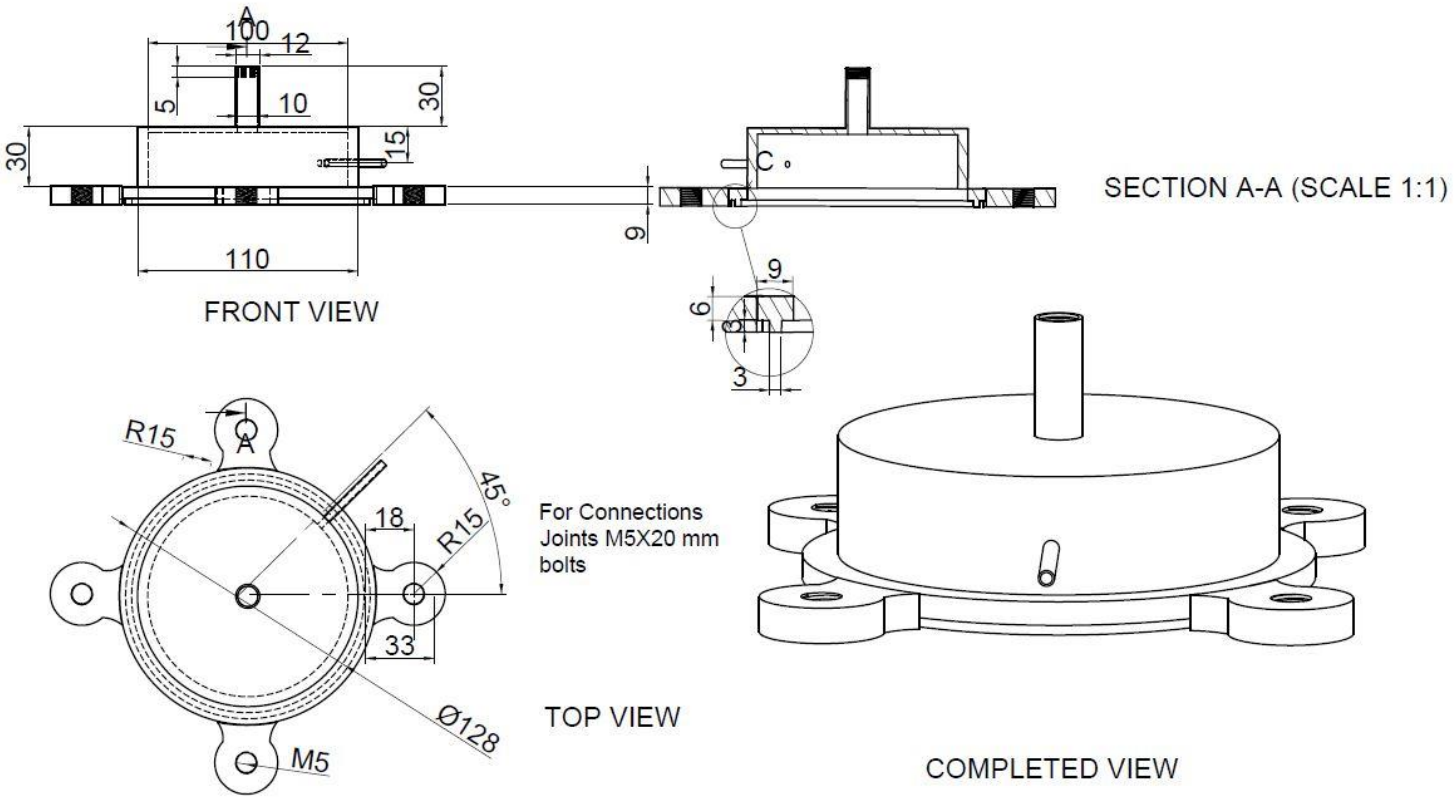

Figure B 3. High temperature: Specimen holder cap

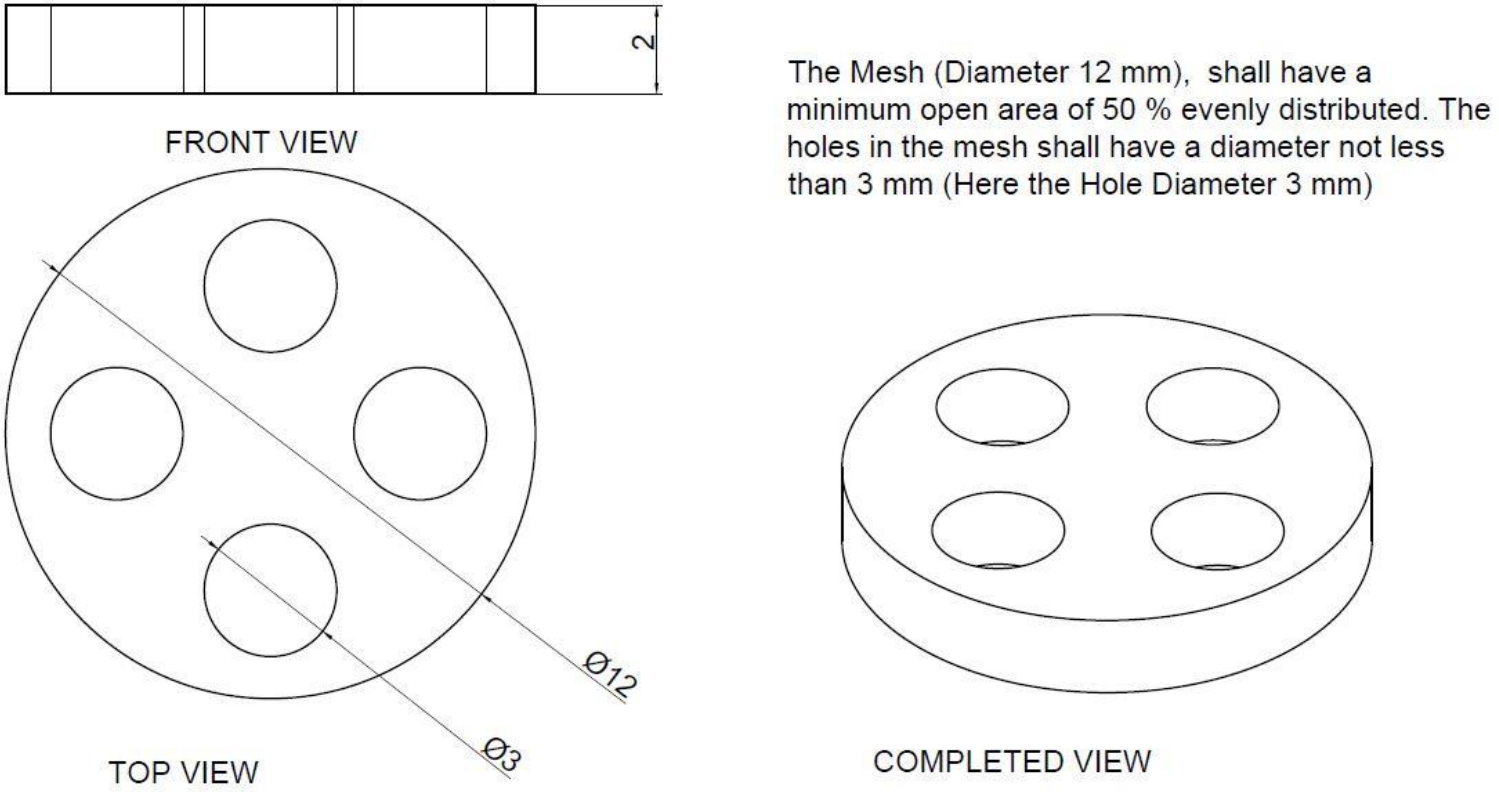

Figure B 4. High temperature test rig: 12 mm Mesh

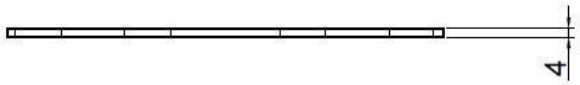

FRONT VIEW

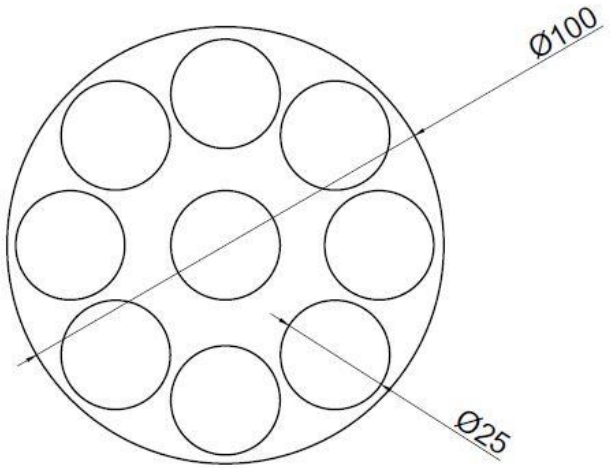

TOP VIEW

The mesh, shall have a minimum open area of 50 % evenly distributed. The holes in the mesh shall have a diameter not less than 3 mm.

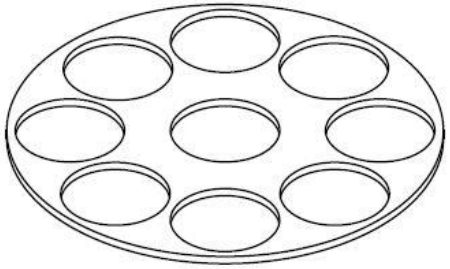

Figure B 5. High temperature test rig: 100 mm Mesh

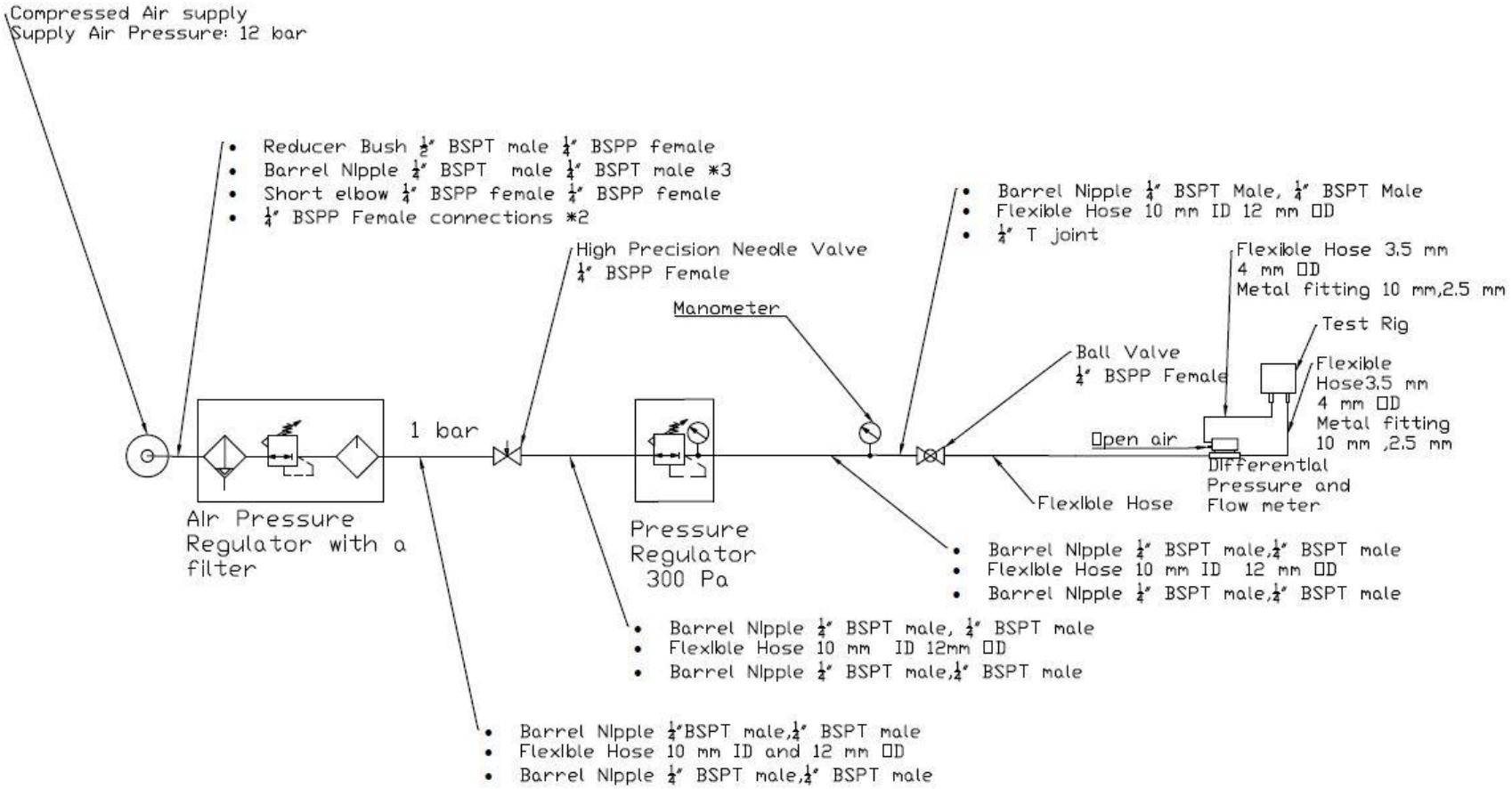

Figure C 1. Schematic diagram for airflow at room temperature

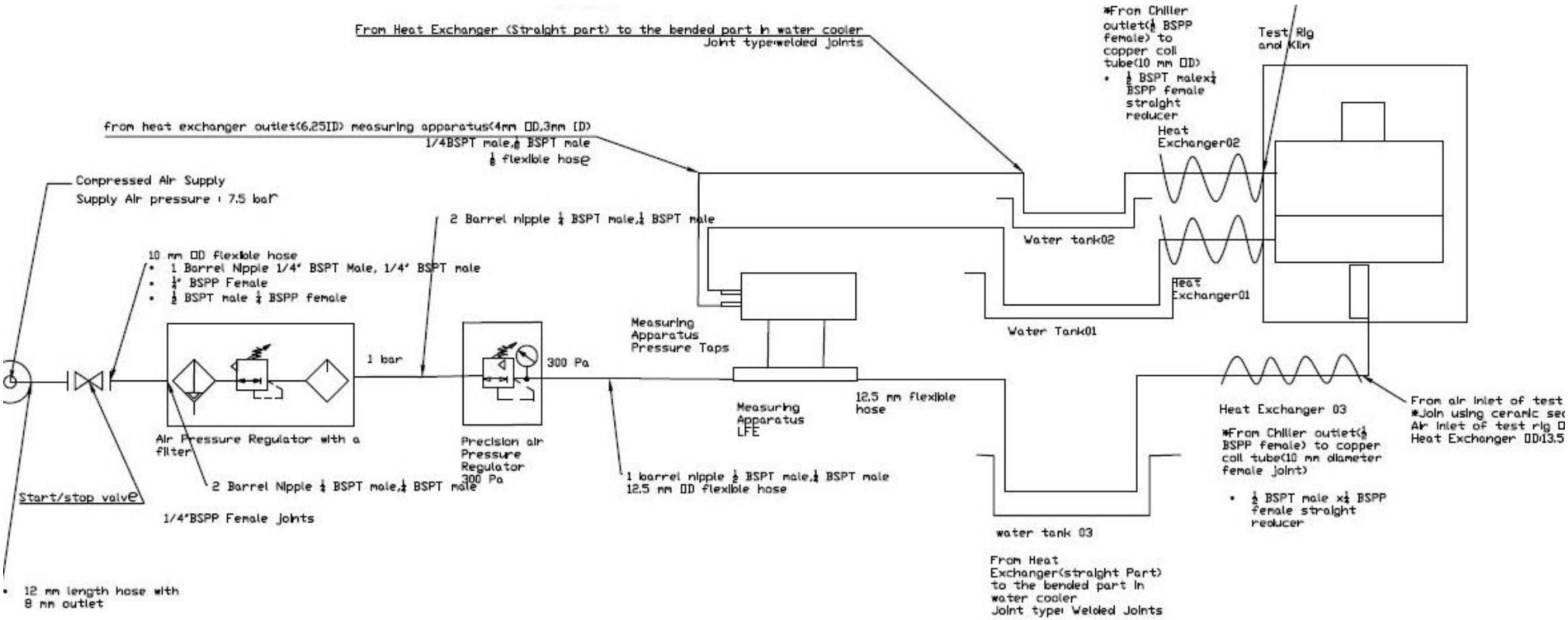

Figure D 1. Proposed schematic diagram for airflow at high temperature

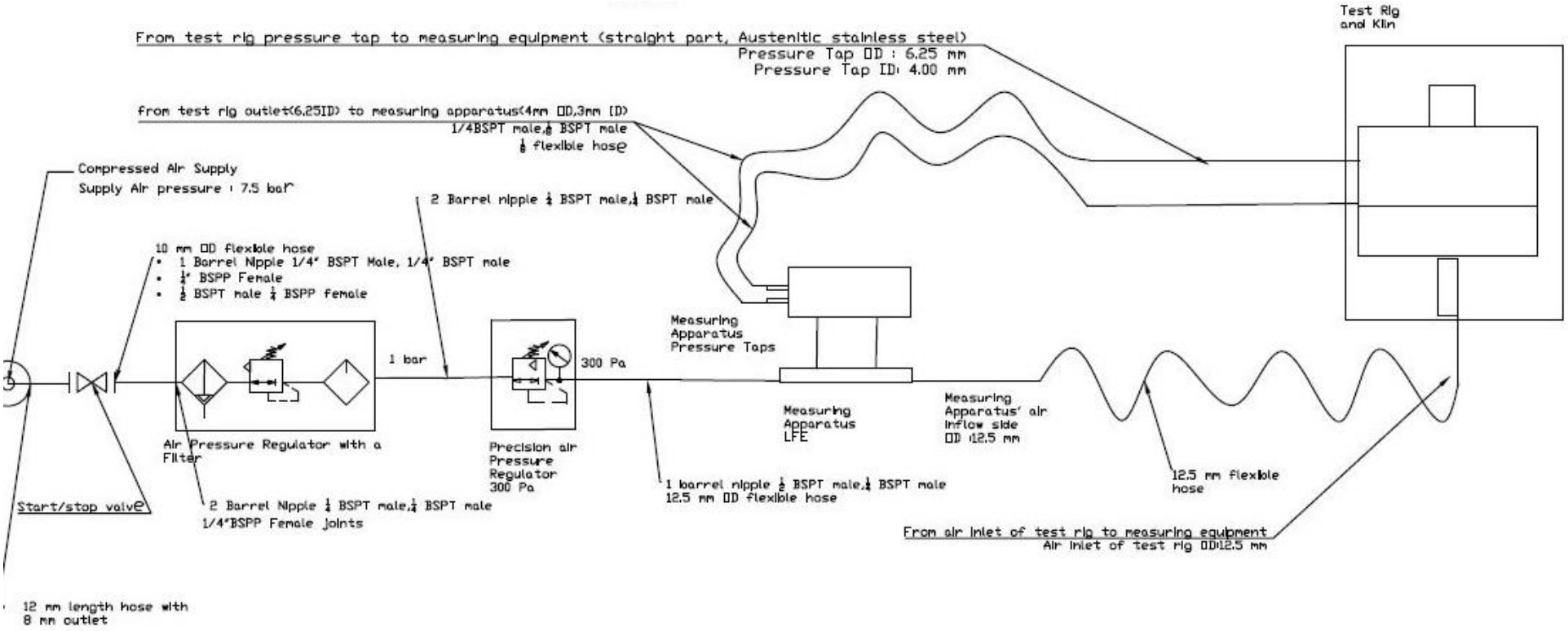

Figure D 2. Schematic diagram for airflow at high temperature

Table E 1. Corrected specific airflow resistance and airflow resistivity values (Without Packing)

Material Index	Initial Thickness (mm)	Temperature°C	Specific Airflow Resistance (Pa.s/m)	Corrected Airflow Resistance (Pa.s/m)	Airflow Resistivity (Pa.s/m^2)	Corrected Airflow Resistivity (Pa.s/m^2)
0064	74	20.1	2,835	2,835	38,316	38,316
		100	3,499	4,444	47,290	60,059
		200	4,632	7,458	62,601	100,788
		300	5,990	11,681	80,950	157,853
		400	7,368	16,947	99,569	229,008
		500	8,699	22,967	117,565	310,370
		600	9,544	28,441	128,974	384,342
		700	9,084	30,158	122,755	407,546
		800	5,053	18,495	68,288	249,932
0064	80	21.3	2,995	2,995	37,439	37,439
		100	3,148	4,156	39,353	51,946
		200	4,311	7,200	53,892	89,999
		300	6,176	12,538	77,203	156,722
		400	7,941	18,899	99,261	236,241
		500	9,485	25,893	118,561	323,673
		600	10,528	32,530	131,596	406,631
		700	9,145	31,460	37,439	37,439
		800	1,750	6,649	39,353	51,946
0064	74	21.3	2,815	2,815	38,047	38,047
		100	3,035	3,855	41,015	52,089
		200	4,033	6,494	54,506	87,755
		300	5,271	10,279	71,236	138,911
		400	6,517	14,924	88,069	201,678
		500	7,953	20,917	107,478	282,668
		600	8,683	25,788	117,335	348,486
		700	7,339	24,293	99,179	328,284
		800	5,112	18,658	69,077	252,133
0058	100	14.9	9,904	9,904	99,040	99,040
		100	10,124	13,262	101,236	132,620
		200	14,816	24,595	148,160	245,946
		300	17,860	35,540	178,595	355,404
		400	21,823	51,065	218,226	510,648
		500	24,905	66,996	249,054	669,956
		600	24,620	74,599	246,202	745,992
		700	21,075	71,235	210,0753	712,347
		800	14,872	55,476	148,728	554,756

Table E 2. Corrected specific airflow resistance and airflow resistivity values for all other values (With Packing)

Material Index	Initial Thickness (mm)	Temperature°C	Specific Airflow Resistance (Pa.s/m)	Corrected Airflow Resistance (Pa.s/m)	Airflow Resistivity (Pa.s/m^2)	Corrected Airflow Resistivity (Pa.s/m^2)
0063	96	23	4,233	4,233	44,095	44,095
		100	4,233	5,334	44,095	55,560
		200	4,173	6677	43,471	69,554
		300	4,153	8,057	43,263	83,931
		400	4,153	9,428	43,263	98,208
		500	4,113	10,736	42,847	111,832
		600	4,131	12,186	43,030	126,938
		700	3,774	12,416	39,311	129,335
		800	2,776	10,075	28,912	104,949
0034	97	10.8	2,696	2,696	27,790	27,790
		100	3,182	4,168	32,803	42,972
		200	3,544	5,919	36,540	61,021
		300	4,472	9,035	46,111	93,144
		400	5,153	12,214	53,129	125,916
		500	5,631	16,102	58,050	157,897
		600	5,294	16,305	54,576	168,095
		700	5,115	17,545	52,733	180,876
		800	5,033	19,026	51,889	196,140
0062	75	8.8	2,556	2,556	34,078	34,078
		100	3,297	2,536	33,812	43,956
		200	4,177	2,546	33,956	55,688
		300	5,007	2,516	33,546	66,756
		400	5,887	2,516	33,546	78,497
		500	6,491	2,516	33,546	86,548
		600	7,837	2,496	33,280	104,498
		700	8,031	2,377	31,682	107,085
		800	3,501	938	12,513	46,674
0061	90	14	4,153	4,153	46,148	46,148
		100	5,373	4,133	45,926	45,926
		200	6,701	4,111	45,676	45,676
		300	8,107	4,053	45,038	45,038
		400	9,438	4,033	44,816	44,816
		500	10,635	3,954	43,929	43,929
		600	11,776	3,874	43,042	43,042
		700	12,015	3,544	39,382	39,382
		800	5,550	1,484	16,488	16,488
0060	96	23	4,952	4,952	51,583	51,583
		100	4,952	6,388	51,583	66,542
		200	4,952	8,121	51,583	84,597
		300	5,631	11,149	58,655	116,137
		400	6,829	15,911	71,135	165,744
		500	7,715	20,676	80,362	215,371
		600	7,148	21,588	74,463	224,878
		700	6,303	21,242	65,659	221,272
		800	926	3,437	9,650	35,800
0059	100	23	8,067	8,067	80,670	80,670
		100	8,366	10,542	83,665	105,418
		200	9,664	15,463	96,644	154,630

		300	10,803	21,065	108,025	210,649
		400	11,442	26,087	114,415	260,866
		500	11,530	33,553	115,303	335,531
		600	11,069	32,986	110,691	329,859
		700	8,686	28,664	86,860	286,636
		800	5,511	20,060	55,111	200,604

Table E 3. Corrected specific airflow resistance and airflow resistivity values for all other values (Without Packing)

Material Index	Initial Thickness (mm)	Temperature°C	Specific Airflow Resistance (Pa.s/m)	Corrected Airflow Resistance (Pa.s/m)	Airflow Resistivity (Pa.s/m^2)	Corrected Airflow Resistivity (Pa.s/m^2)
0057	103.25	14.3	8,307	8,307	80,451	80,451
		100	8,706	11,317	84,319	109,615
		200	11,042	18220	106,946	176,460
		300	14,580	29452	141,212	285,249
		400	17,816	42045	172,548	407,213
		500	20,164	54443	195,294	527,294
		600	20,799	63438	201,448	614,415
		700	20,187	68637	195,519	664,765
		800	16,294	60938	157,808	590,201
0063	98	16	4,126	4,126	42,101	42,101
		100	4,253	5,487	43,399	55,985
		200	4,833	8,022	49,313	81,860
		300	6,317	12,634	64,459	128,919
		400	7,874	18,347	80,348	187,211
		500	9,226	24,725	94,142	252,301
		600	10,274	31,234	104,839	318,710
		700	10,416	35,101	106,283	358,175
		800	7,928	29,413	80,899	300,136
0034	96	8.8	3,055	3,055	31,824	31,824
		100	4,672	6,167	48,670	64,244
		200	6,678	11,218	69,558	116,857
		300	8,943	18,155	93,161	189,118
		400	11,250	26,886	117,183	280,067
		500	13,355	36,593	139,115	381,176
		600	14,458	44,820	150,604	466,872
		700	14,638	50,503	152,484	526,069
		800	17,432	66,415	181,581	691,825
0062	86	20	3,315	3,314	38,542	38,542
		100	3,395	4,481	39,471	52,102
		200	3,609	6,028	41,971	70,091
		300	4,994	10,089	58,073	117,308
		400	6,809	16,137	79,174	187,643
		500	8,646	23,604	100,535	274,461
		600	10,124	31,181	117,717	362,567
		700	10,427	35,766	121,249	415,883
		800	7,079	26,828	82,309	311,952
0061	90.51	23	4,353	4,353	48,094	48,094
		100	4,354	5,487	60,619	48,110
		200	6,130	9,808	108,365	67,728
		300	8,086	15,689	173,336	89,348

		400	10,303	23,389	258,409	113,836
		500	11,322	27,965	308,967	125,088
		600	14,137	40,856	451,401	156,194
		700	140,578	41,470	458,181	155,315
		800	5,242	17,248	190,568	57,923
		800	20,738	77,147	207,384	771,470